MICROWAVE INTERFEROMETRIC MEASUREMENTS OF ELECTRON DENSITY IN LASER-GENERATED PLASMA CHANNELS

BY

KATHRYN ELLEN KEISTER

DISSERTATION

Submitted in partial fulfillment of the requirements
for the degree of Doctor of Philosophy in Physics
in the Graduate College of the
University of Illinois at Urbana-Champaign, 2011

Urbana, Illinois

Doctoral Committee:

Professor S. Lance Cooper, Chair

Professor J. Gary Eden, Director of Research

Professor David Hertzog

Associate Professor P. Scott Carney

Abstract

Measurements of the temporal decay of the absolute electron density in a laser-produced plasma channel have been made with a 9.2 Ghz microwave interferometer. The plasma channels were generated by sub-picosecond laser pulses (λ =248 nm, 40 mJ per pulse) produced by a hybrid Ti:sapphire/KrF excimer amplifier system. The ultrashort pulse duration resulted in a δ-function excitation source, allowing the subsequent plasma decay to be explored without further excitation of the gas and without deconvolving the excitation source profile from the electron density decay data. The temporal resolution of the interferometer has been demonstrated to be a few nanoseconds (bandwidth of $\approx$1 GHz), and electron density decay profiles have been measured in argon and nitrogen at pressures in the range of 1-650 Torr. Gas kinetic models in argon and nitrogen have been developed, and have shown good agreement with the measured electron density profiles.

Model predictions of the dissociative recombination rate constants, α_D, in argon and nitrogen are reported, $\alpha_D\,(\mathrm{Ar}) = 1 - 6 \times 10^{-6}$ cm^3 s^{-1} and $\alpha_D\,(\mathrm{N_2}) = 1 - 3.25 \times 10^{-6}$ cm^3 s^{-1}. At pressures >200 Torr, the reported values show good agreement with previous measurements, and in the pressure range 20-200 Torr, the values presented here are the first to be reported. The multiphoton ionization (MPI) cross section for argon, $\sigma_{(4)}$, is estimated to be in the range $10^{-117} - 10^{-118}$ cm^8 s^3, which is within an order of magnitude of the one previous measurement, and the experimental technique is shown to have the potential to improve the precision of this estimate.

Dedicated to the memory of James E. Keister (1914-2010)

Electrical Engineer Extraordinaire, but loving grandfather first.

Acknowledgments

This thesis, both the experiments and the writing, would not have been possible without the support of family and friends.

First, I would like to thank my parents and my sisters for their unwavering support and patience as I have stumbled through grad school, whether by luck or lack of imagination has yet to be determined. From the beginning of my academic career, which began, as far as I can tell, in elementary school, they have put up with my "shop talk", encouraged my investigations, and held my hand when I wanted to throw in the towel.

I would also like to thank my adviser, Gary Eden, who has shown an admirable degree of patience in my long years here. Always ready with a new idea and an encouraging word, he has almost made me believe that I will make him famous!

The experimental design and data collection presented here represents the combined efforts of myself, Clark Wagner, and Jeff Putney, from whom, along with Dave Virgillito, I have learned everything I know about lasers. Looking back on the experiment, it is only by the skill and determination of the three of us that it ever worked! Many thanks also to Joe Verdeyen, without whose expertise in microwave technology we would never have been able to operate the experiment.

The gang at Club LOPE has been some of the best friends I could ever hope to have, and has made every day at work a new adventure. To my predecessors in the PhD, Tom Spinka, JD Readle, Paul Tchertchian, and Seung Hoon Sung, I have learned a great deal by watching you, and your success has encouraged me that I can make finish too. A special thanks to the Coffee Squad, who have made legally addictive stimulants a daily ritual of

friendship and conversation. Thanks to Tom Houlahan for his unique analysis of electron cooling by momentum transfer. Thanks to Darby Hewitt, my "tea buddy", for always being willing to take time to talk.

Outside the lab, the few times I managed to escape, I was blessed by the friendships of so many, including Tim and Roxann Bossenbroek, Ned and Linda O'Gorman, Dave and Sherry Thomas, Irene Koshik, Kevin Hamilton and Susan Becker, Patricia Lazicki, Vernita Gordon, Rachel Tyson, Julie Fultz, Steve and Karolyn Williamson and others who I hope will forgive me for having forgotten them! I also owe a special debt to my roommate of many years, Crystal Goshorn, who tolerated dishes in the sink and laundry in the dryer, and provided an ear to listen, a hand to high-five, and a shoulder to cry on.

Graduate school is truly a test of psychological stamina as much as intellectual capacity, and while I may have been born with the capacity, I was not born with the stamina, and cannot express enough my gratitude for the friends who have helped me through.

Table of Contents

Chapter 1 Introduction **1**

Chapter 2 Previous Work **8**
2.1 Traditional Plasma Diagnostics 8
2.2 Laser Filaments 12

Chapter 3 Experimental Techniques **16**
3.1 Femtosecond Laser System 16
3.2 Microwave Interferometer 21

Chapter 4 Microwave Interferometer Analysis **33**
4.1 Theory 33
4.2 Interferometer Calculations 35
4.3 Representative Data and Analysis 38
4.4 Electron Diffusion 40

Chapter 5 Representative Data and Discussion **46**
5.1 Electron Decay Processes in Argon and Determination of Critical Constants 46
5.2 Electron Decay Processes in Nitrogen and Determination of Critical Constants 68

Chapter 6 Conclusions **79**

Appendix A Absolute Electron Density Measurements of Plasma Filaments **81**
A.1 Experimental Techniques 81
A.2 Results 84

References **98**

Chapter 1

Introduction

Accounting for 99% of the visible matter in the universe, plasma is commonly referred to as the fourth state of matter. Plasma is the result of partially ionizing a gas or vapor, thus rendering the medium partially electrically conductive, and the degree of ionization can be in the range from $< 10^{-6}$ to unity. First identified in 1879 in an electrical discharge tube by British scientist Sir William Crookes, plasma was recognized as a distinct state of matter and dubbed "radiant matter" in a lecture to the British Association for the Advancement of Science [1]. The term "plasma" was coined in 1928 by Irving Langmuir with the statement, "We shall use the name *plasma* to describe this region containing balanced charges of ions and electrons." [2]. Since then, plasmas have been observed in many natural settings, and has been produced artificially for a wide range of applications.

Plasmas are typically catagorized by their production method and/or internal parameters such as temperature and density. Figure 1.1 shows the temperature and electron density scales of some common natural and artificial plasmas. Terrestrial plasma sources include lightning, flames, the polar aurorae, and St. Elmo's fire, a coronal discharge historically seen on the masts of ships. While somewhat rare on Earth, plasmas occur commonly above the upper atmosphere. Early research in radio transmission led to the discovery of the ionosphere, a shell of plasma 50-1000 km above the Earth which acts as a reflector for radio waves. Beyond the atmosphere, the sun and other stars are composed of plasma, as is the space between them, although interstellar space is a very low density plasma [3–6].

The most common method of artificially producing plasma is the application of voltage to conductive electrodes. By varying the frequency and amplitude of the applied voltage,

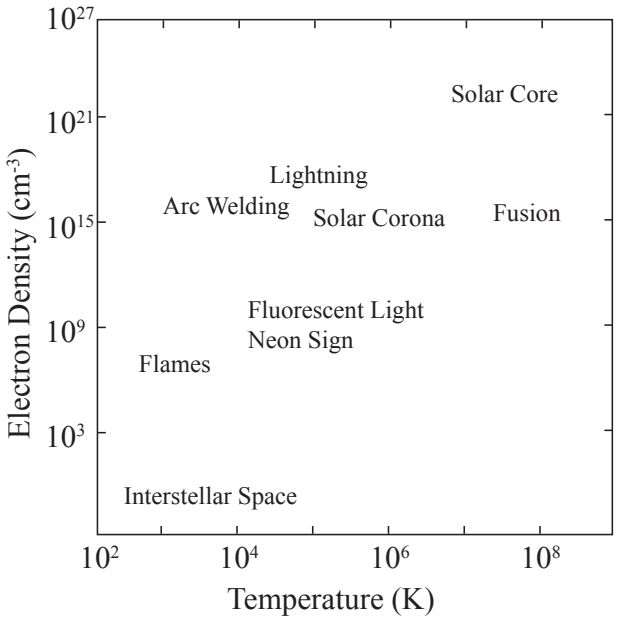

Figure 1.1: Graph showing plasma properties for commonly occuring natural and artificial plasmas. Adapted from figures in [3] and [4].

as well as the pressure of the plasma medium, a wide range of plasma applications and devices are possible. Fluorescent light bulbs, neon signs, and plasma television displays all operate at low pressures (0.1-10 Torr) and low frequencies (up to 100 kHz). Higher frequency discharges (tens of MHz) are present in industrial applications such as surface processing of semiconductors. Other plasma applications include welding, plasma cutting, and arc lamps in projectors and stage lighting.

Non-electrode methods of producing plasma include those generated by electron beams, lasers, microwaves, and shock tubes. Shock tubes are used to study plasmas at very high pressures (10-20 atm) and high temperature (typically 9,000-13,000 K). A shock tube consists of a hollow tube containing a region of high pressure and a region of low pressure, separated by a diaphragm. The diaphragm bursts in a controlled manner, sending a shock wave into the low pressure region of the tube [7]. This shock wave increases the pressure and temperature of the gas, producing a plasma. Microwave sources, in addition to being used to probe plasma parameters, as will be discussed in detail later, are also capable of generating

plasmas. Microwave and radio frequency (RF, ranging from 30 kHz to 300 GHz) radiation has the advantage over electrode discharge plasmas that there is no contact between the plasma-generating electrodes and the plasma itself. A more direct way to ionize gas atoms and molecules, especially at high pressures, is an electron beam, whereby a high energy (10 keV to 1 MeV) electron beam is directed into a neutral gas, and the beam electrons transfer energy by collisions with gas atoms or molecules, producing ions and free electrons. Electrons can also be stripped from their parent ions by a high power laser beam. A laser beam with sufficient intensity, usually hundreds of MW/cm^2 depending upon the material, induces breakdown between ions and electrons.

Given this large range of both natural and artificial sources and applications, research in plasma science covers a variety of fields, including meteorology, astronomy, physics, fusion energy research, spectroscopy, and optics. The recent report by the Plasma 2010 subcommittee of the National Research Council underscores the breadth of research in plasmas [8]. This results in a diverse range of experimental techniques and goals. These fields are united, however, by their common interest in plasma fundamentals. As shown on the axes of Fig. 1.1, two of the most significant characteristics of a plasma are the electron density, the number of free electrons per unit volume, and the temperature which is closely related to the average kinetic energy of the electrons. These two parameters dictate the conductivity of the plasma, its response to electric and magnetic fields, and the reaction rates of many plasma reactions.

In addition to free electrons, plasmas contain atomic and molecular ions, neutrals, and various excited state species in a plasma. The interactions between these species are critical to the behavior of the plasma and, thus, their study is a vital research endeavor. For example, energetic electrons can interact with gas phase atoms and molecules to produce ions by electron impact ionization,

$$\mathrm{M} + e^- \rightarrow \mathrm{M}^+ + 2e^- \tag{1.1}$$

where M is the molecule or atom being ionized. This reaction will be linear in the electron density, but will depend strongly on the electron temperature, or, more specifically, on the electron energy distribution function (EEDF). Less energetic electrons may be captured by positive ions, in a process known as recombination, or by strongly electronegative atoms or molecules in a process known as attachment. In air plasmas, oxygen attachment

$$O_2 + O + e^- \rightarrow O^- + O_2 \tag{1.2}$$

is the dominant electron loss process [9], resulting in lifetimes of free electrons in atmospheric pressure air plasmas on the nanosecond timescale. Recombination rates [10] can be either linear in electron density, as is the case for the two-body recombination process

$$M^+ + e^- \rightarrow M, \tag{1.3}$$

or the rate may be quadratic in electron density as is the case for the three-body recombination process

$$M^+ + e^- + e^- \rightarrow M + e^-. \tag{1.4}$$

Additionally, there are reactions between neutral atoms and molecules that are mediated by plasma electrons, such as the reaction

$$M_{triplet} + e^- \rightarrow M_{singlet} + e^-, \tag{1.5}$$

in which the electron is necessary to conserve spin [11]. These are just a few examples of the plasma reactions that depend on electron density and temperature, which, combined with the role of electron density in electromagnetic interactions, demonstrate the importance of accurate measurements of electron density to understanding plasmas.

In plasmas without a steady-state excitation source, the electron density will decay, yield-

ing information about many of the reactions described above. The main hurdle in probing the electron density and its temporal decay following a transient excitation source is decoupling the probe measurement from the plasma production mechanism. Because they are often in physical contact with the plasma volume, metal electrodes in discharge plasmas can be a source of additional electrons and reaction species, corrupting the measurement of the electron density. In addition, many discharge plasmas require voltages up to several kV and frequencies up to several GHz, which can add noise to electrical measurements and disrupt measurement electronic systems. Furthermore, the unambiguous determination of electron reaction rate constants from electron density decay times requires that the electron production process be short when compared to the shortest electron decay process. Thus, the electron generation mechanism can be viewed as $\delta(t)$ – the delta function and the deconvolution of the electron decay transient from the electron production function is not necessary. In electron beam and laser-induced plasmas, the high power plasma production necessarily occupies the same volume as the plasma. Thus, any probe inserted into the plasma volume will also encounter the beam, leading to probe damage, disruption of plasma production, or introduction of new interaction processes and species.

Measuring the electron density and characterizing its decay is, thus, a challenging problem in all types of plasmas. To explore the decay and interaction processes, it is additionally necessary to have a method which provides time resolution. Due to oxygen attachment, as mentioned above, the recombination rates at atmospheric pressure in air are on the nanosecond timescale [9], requiring that the measurement system have a bandwidth of at least 1 GHz, or that the plasma generation volume has gas and pressure controls to increase characteristic reaction times. Measurement efforts, both time-resolved and static, have included spark gap conductivity measurements, electrostatic and magnetic probes, optical and microwave interferometry, and absorption and emission spectroscopy. Further discussion of these is found in Sect. 2.1.

Microwave interferometry, the diagnostic technique adopted for this dissertation, has

been used as a plasma diagnostic since the 1950s [12]. A partially ionized plasma can be described as a dielectric, and microwaves, like all electromagnetic waves encountering a dielectric, will experience transmission losses and phase shifts. Various interferometric structures are developed to measure these shifts, which can be from which the electron density of the plasma can be calculated. Requiring no physical probe to be inserted into the plasma, and having the potential for sub-nanosecond time-resolution, microwave diagnostics are a versatile plasma measurement technique. The plasma volume to be measured can be located within a segment of rigid metallic waveguide, or between microwave antennas [12], enabling a wide range of geometries and plasma sources to be tested.

With the increase in available peak laser power in the last decade, lasers are now widely available that can produce a plasma in an atmosphere of air. This has a number of advantages for studying plasma properties. The electrode-less production mechanism does not require high-voltage electronics in contact with the plasma, which eliminates metal electrode materials as a source of electrons and additional reaction products. Furthermore, this design eliminates the electrical noise associated with high discharge voltages. Ultrafast laser technologies, in addition to increasing the available peak powers, allow femtosecond plasma production pulses, with no further excitation of the plasma, resulting in what can be considered a δ-function excitation source. While these properties make laser-induced plasmas an attractive research tool, there are difficulties introduced by the high intensity laser beam that occupies the same volume as the plasma itself. A probe inserted into the plasma would also encounter the laser beam, interrupting plasma production, and introducing new interactions that could corrupt the measurement, thus making non-invasive microwave techniques an ideal diagnostic tool.

Combining the capabilities of modern high-powered lasers with the time-tested advantages of microwave plasma diagnostics has created a unique laboratory environment for the characterization of laser-induced plasmas. While both techniques have been studied separately, this dissertation represents the first time that they have been used in combination. In

this dissertation, an electron density probe system based on a 9.2 GHz microwave interferometeris applied to the measurement of the temporal decay of electron density in a rare gas or N_2 background. Measurent made over a range in pressure allows for the determination of several fundamental collisional rate constants and optical cross sections. Extensive testing of the interferometer resulted in a detailed characterization of its performance limits, and, to evaluate the measurement technique and detemine several critical constants, a gas kinetic model was developed in argon and nitrogen. In addition to evaluating the experimental technique, the results of the model are used to calculate rate constants in a pressure range for which there are no reported values, and to estimate multiphoton ionization cross-sections for which there are no other values in the literature.

Chapter 2

Previous Work

2.1 Traditional Plasma Diagnostics

The identification of the first artificially produced plasma by William Crookes in 1879 was part of an active research field involving vacuum electrical discharge tubes, eventually leading to the discovery of the electron by J. J. Thompson in 1897. [13]. In the early part of the twentieth century, most plasma research was conducted in the context of these discharge tubes and their close relative, light bulbs. Irving Langmuir, an American chemist, was researching ways of extending the lifetime of lamp filaments when he developed the theory of plasma sheaths, the boundary layer between a plasma and a solid surface. Langmuir also developed a probe, called a Langmuir probe, to measure the electron density of what he had dubbed *plasma* [2].

After World War II, hopes for controlled nuclear fusion fueled new interest in plasma physics. Concurrent with the development of plasma generation processes and fusion studies, research on diagnostic methodology proceeded with equal intensity. In the introduction to a 1965 compendium of plasma diagnostic techniques, editor Richard Huddlestone writes:

> "Indeed progress in plasma research can be measured, to a large extent, by the stage of development of its measurement techniques and the adequacy of accompanying theoretical interpretation.
>
> It should be noted that diagnostic methods can be, and in many cases are, based on phenomena which are only remotely related to intrinsic plasma characteristics, provided that in each instance there is a well-understood connec-

tion between such properties and the condition of the plasma. For this reason, plasma diagnostics has a somewhat interdisciplinary character, borrowing its methods from many branches of physics including optics, spectroscopy, high-energy physics, microwave technology, and fluid mechanics. [14]"

Creative probe and measurement techniques have proven vital to the continued research of laboratory plasmas, fusion science, astrophysical phenomena, and artificial atmospheric reentry conditions. Plasma diagnostic techniques must meet stringent requirements, both in materials, which must be selected with care to maintain plasma purity, and in time resolution, for which microsecond or even nanosecond resolution may be required to monitor rapidly changing or short-lived plasma phenomena. A summary of the main subgroups of methods is described here, but the discussion is adapted primarily from Ref. [14]. While there are macroscopic techniques to measure large-scale properties of plasmas, including current, voltage, conductivity and emitted radiation, examining internal parameters or spatially resolved phenomena, requires the introduction of other methods.

One of the earliest probe techniques developed was the electric probe, also commonly known as a Langmuir probe. The electrostatic probe is a simple structure - a small metallic electrode, usually a wire, that is inserted into the plasma volume, as shown in the schematic structure in Fig. 2.1. The simple structure is offset, however, by the complex theory that is required to extract reliable information from its measurements, given the perturbation the probe introduces to plasma behavior. The probe introduces an additional plasma boundary, near which the behavior of the plasma changes from the bulk. A layer, which Langmuir called the "sheath", forms near the boundary, in which there can be a large electric field due to different densities of electrons and ions. Accurate theoretical models of the sheath are necessary to subtract this effect from the experimental measurement to obtain the non-sheath plasma conditions.

The interaction of plasmas with magnetic fields, an active research subfield of its own, has produced many probe techniques that examine the magnetic interactions of the plasma.

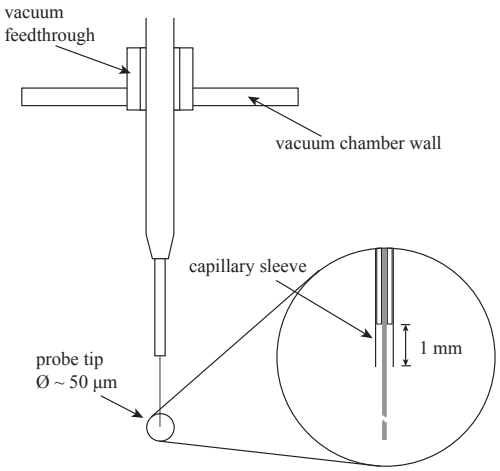

Figure 2.1: Schematic of an electrostatic (Langmuir) probe.

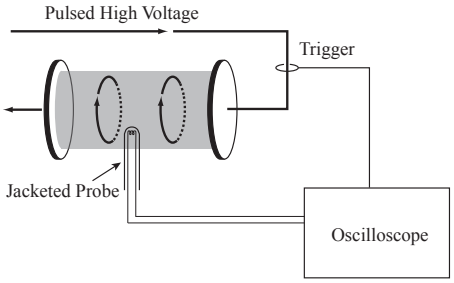

Figure 2.2: Schematic of magnetic probe setup.

These are limited, however, by the necessity that the probe be inserted into the plasma volume, making the technique unusable for high density or high temperature plasmas. A schematic of a typical magnetic probe apparatus is shown in Fig. 2.2, where the plasma is produced by a discharge between electrodes, with an azimuthal magnetic field due to the current between the anode and the cathode. A magnetic sensor, which can be as simple as a coil of wire, is inserted in the plasma, usually with some protective insulation or jacket. Probe sensitivity and frequency response can be easily adjusted by changing the area and number of turns in the coil, respectively, but one can only be improved to the detriment of the other, limiting the range of applications for this technique.

In addition to the free electrons and ions that define the existence of a plasma, the excitation source also produces excited states of both ions and neutral species. The deexcitation radiation produced by these species as they decay provides the basis for a large range of diagnostic techniques, based on both continua and discrete line shapes which are used to determine plasma parameters, including electron density and electron temperature. Measuring emitted radiation is attractive as an experimental technique because it is nonperturbative, and has the potential for high time resolution, but these advantages are balanced by the

need for well-developed theories to correctly interpret the results. For example, theoretical predictions of relative excited state population densities can be used to measure electron temperature by comparing the intensity of two or more lines originating in different excited states, but the results are limited in accuracy by the theoretical predictions. Line broadening mechanisms in plasmas offer another opportunity to probe electron density and temperature. Doppler broadening [15], because it is determined by the velocity of the radiating particle, can be used to measure electron temperature, while Stark broadening [16], arising from interactions between emitting particles, is sensitive to the electron density.

Most important for this dissertation is the class of techniques that measure the transmission, attenuation, and scattering of radiation from the plasma volume. These measurements require an optical or microwave frequency radiation and are typically used to detect the change in index of refraction of the plasma, often by interferometry, which provides the necessary resolution to measure small changes in the refractive index. The changing index of refraction is then analyzed to determine the plasma property of interest. As with other spectroscopic techniques, these methods do not require the insertion of a sensor or probe into the plasma volume, making microwave diagnostics ideal for the applications in this dissertation.

During World War II, the development of microwave generation, detection, and transmission technology was greatly accelerated, as a result of its utility for radar, communication, and power transmission. After the war, it was adapted to be used as a diagnostic technique in gaseous discharges, with early methods including measuring changes in the frequency of a resonant cavity [12] and the impedance of transmission line terminating in the plasma [17] to determine the electron density of the plasma. In 1952, Goldstein *et al.* [18] introduced a method in which the plasma filled a section of rigid waveguide and the microwave transmission of the plasma was used to determine plasma parameters, and later, this method was developed for applications where the plasma only partially filled the waveguide. Microwave diagnostics are still used to analyze discharge plasmas, but this work represents the

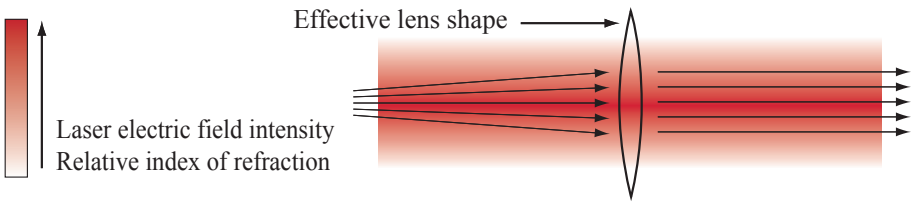

Figure 2.3: Illustration of self-focusing in high-intensity laser beams.

first attempt at conjoining a microwave interferometer with a laser induced plasmas. This technique is further elaborated in Sections 3.2 and 4.1.

2.2 Laser Filaments

Part of the motivation of this dissertation was the development of a technique to characterize a laser plasma phenomenon known as "filamentation". A laser beam naturally experiences dispersion and divergence when it interacts with air, reducing the peak intensity and therefore limiting the length over which plasma is formed. Above a critical intensity, however, third order nonlinearities result in a change in the index of refraction with the electric field intensity, producing an effective lens and leading to what is referred to as "self-focusing" (illustrated in Fig. 2.3). When this self-focusing balances dispersion, the laser pulse maintains high peak intensity over long distances, producing a plasma "filament". While this phenomenon was predicted as early as the 1960s [19–21], it wasn't until the development of femtosecond lasers that the phenomenon was observed in 1995 [22]. There are numerous industrial and defense applications of this phenomenon, primarily using the filament as a transient conductor for high voltage discharges, often called "guided lightning".

The potential use of filaments as a conductor stimulated considerable interest in measuring the electron density, a critical component in determining the plasma conductivity of the filaments. In 1999, two groups almost simultaneously reported estimates of the elec-

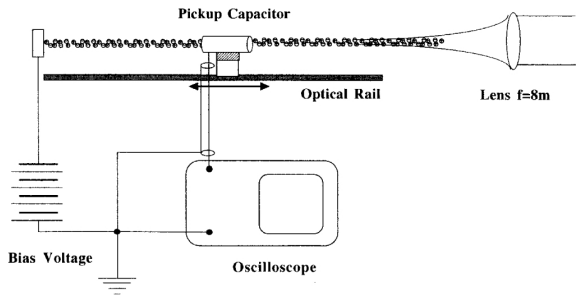

Figure 2.4: Schematic experimental setup from Ref. [23]. Reproduced with kind permission from Springer Science+Business Media: [23], Fig. 2.

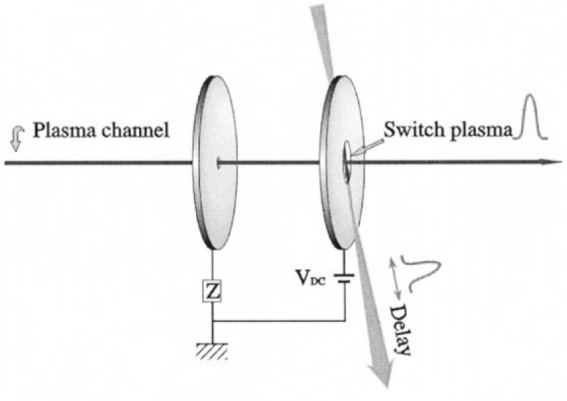

Figure 2.5: Experimental scheme for cross-conductivity measurements from Ref. [25]. Reprinted from [25] with permission from Elsevier.

tron density using two different conductivity measurements. Schillinger and Sauerbrey [23] used capacitive coupling to a pickup capacitor, shown in Fig. 2.4, to demonstrate the existence of free charges in the channel, and to set a lower bound on the electron density of $n_e \gtrsim 6 \times 10^{11}\,\mathrm{cm}^{-3}$. Tzortzakis *et al.* [24] used a copper electrode with a pinhole to allow the filament to pass through, and measured the current as a function of the distance between the drilled electrode and another, solid electrode for fixed applied voltages of 1-1.5 kV. The conductivity of the channel and, therefore, the electron density was extracted from these measurements. They reported an electron density range of $n_e = 3 \times 10^{16} - 2 \times 10^{17}\,\mathrm{cm}^{-3}$. In a proof note, Schillinger and Sauerbrey attribute the large spread between the two measurements to different estimates of the filament diameter. Both of these experiments include a solid metal electrode that terminates the laser beam, and it is likely that a laser pulse with intensities of $10^{13} - 10^{14}\,\mathrm{W/cm}^2$, as was present in both experiments, would produce significant photoelectron densities when incident on the electrodes, resulting in additional electron production and corrupting conductivity measurements. To address this problem, Tzortzakis *et al.* developed a cross-conductivity method, shown in Fig. 2.5, in which both electrodes had holes in them, and a second plasma channel, a switching plasma, was used to allow conduction between the main plasma channel and the edge of the second electrode [25].

By varying the delay between filament production and the creation of the switching plasma, time-resolved measurements were possible. The electron density was assumed to be proportional to the peak current between the electrodes, but no absolute electron density was reported using this method.

Several all-optical measurement techniques have also been developed. Tzortzakis *et al.* added an optical diffractometry technique to their studies of laser induced filaments [25]. A probe beam crossed the filament perpendicular to the filament direction of travel, with a variable delay, and the far field image of the probe beam was recorded with a CCD camera. Plasma characteristics were extracted from the beam image by modeling the filament as a thin diverging lens, and the lower limit of the electron density for this technique was reported to be 10^{15} cm^{-3}. A longitudinal spectral interferometry technique was developed by La Fontaine *et al.* [26], whereby a probe pulse propagated through the filament, accumulating a phase shift due to the free electrons in the filament and a reference pulse propagated through only air. The interferogram between the probe and reference pulses was recorded by a spectrometer, and the electron density extracted from the accumulated phase. This longitudinal technique had a large shot to shot variance, as the path of the probe beam was perturbed by the steep radial electron density gradients in the filament. The authors analyzed the radial refraction of the probe beam to determine that the distance the probe beam was actually traveling through the plasma was only a fraction of a meter. The inferred electron density was a few times 10^{16} cm^{-3}, but no time resolution or detection limit was given for this technique. Théberge *et al.* also used the longitudinal diffraction technique, and additionally monitored the fluoresence of a specific transition of the N_2^+ ion, which they assumed to be proportional to the total number of ions, and therefore electrons, in the plasma column [27]. Peak electron densities in the range of $10^{15} - 10^{18}$ cm^{-3} were reported.

More recently, Rodriguez *et al.* [28] used a transverse geometry to image the diffraction patterns of plasma filaments, and verified their results with a rate equation population kinetics model. In a manner similar to the other transverse interferometric techniques, a

portion of the laser beam was diverted to a beamsplitter and sent to an optical delay stage before crossing the filament at a right angle. The technique is holographic rather than interferometric because it compares the far-field image of the probe beam with and without the filament present, in which both images were recorded separately. The interference fringes are compared to a beam propagation model in order to determine the electron density. Time resolution is not specifically listed, but data shows points separated by tens of picoseconds. Peak electron densities of 18×10^{16} cm^{-3} were reported, and the lower detection limit on electron density is reported to be 10^{16} cm^{-3}, which is reached in < 1 ns for the filaments under study, thus limiting the timescale over which decay processes can be examined.

While these optical spectroscopic measurements have the advantages of sub-ns time resolution and a non-invasive probe mechanism, an improvement over the early conductivity measurements, they are limited in scope by the detection limit of the techniques. Microwave interferometry has a lower detection limit of at least 10^{10} cm^{-3} (see Eqn. 4.12 and following), six orders of magnitude below that of optical spectroscopy. Additionally, the only filaments measured by these techniques are produced in atmospheric pressure in air, while the technique developed in this dissertation examines a pressures almost three orders of magnitude in range, and can be applied to any non-corrosive gas.

Chapter 3

Experimental Techniques

Sub-picosecond ultraviolet laser pulses, having a center wavelength of 248 nm and energies up to 40 mJ, are produced by a hybrid Ti:sapphire/KrF excimer amplifier system. A Ti:sapphire oscillator and regenerative amplifier generate 400 μJ, 160 fs pulses at 744 nm, which are frequency tripled before passing through a prism pair pulse stretcher, by which the ultraviolet seed pulse width can be stretched or compressed to temporal widths between 500 fs and 2 ps. The seed makes three total passes through a KrF (248 nm) oscillator and amplifier, resulting in sub-picosecond, 40 mJ pulses at a repetition rate of 10 Hz. A single laser pulse produces a plasma channel in a vacuum sealed section of X-band waveguide which, in turn, is filled with one of several test gases or gas mixtures. The ultrashort excitation pulse length results in a plasma decay process that is unperturbed by residual laser energy and continued plasma generation, thereby allowing exploration of the recombination mechanisms with no further laser excitation of the gas. The X-band waveguide forms one arm of a full-bridge interferometer operating at 9.2 GHz. The laser and microwave interferometer experimental system allows exploration of the recombination dynamics of pure gases over a large pressure range.

3.1 Femtosecond Laser System

The entire laser system is shown in Fig. 3.2 in the form of a schematic diagram. A KMLabs Ti:sapphire oscillator kit operating at a repetition rate of 90 MHz produced 2.7 nJ, 85 fs pulses at 744 nm, which were subsequently amplified in a Spectra-Physics Spitfire regener-

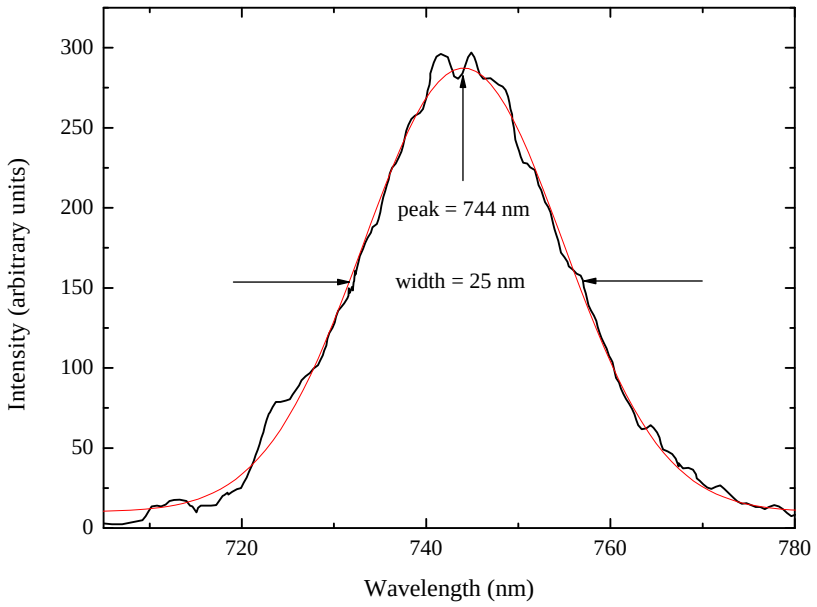

Figure 3.1: Wavelength spectrum of the IR seed pulse, illustrating the peak wavelength of 744 nm, and a bandwidth of 25 nm.

ative amplifier, resulting in a train of 400 μJ, 160 fs seed pulses produced at 744 nm at a pulse repetition frequency of 1 kHz. The wavelength spectrum of the seed pulse is shown in Fig. 3.1, confirming a peak wavelength of 744 nm and a bandwidth of 25 nm. These seed pulses were then frequency-tripled to 248 nm in a tripler consisting of three nonlinear crystals. First, the pulse passed through a bismuth borate, BiB_3O_6 (BiBO) crystal, producing second harmonic radiation at 372 nm. Second harmonic generation produces photons at twice the frequency of the fundamental, but at an orthogonal polarization and with a phase shift [29]. To maximize efficiency in the third crystal, a calcite flat realigned the phase of the doubled light with the residual fundamental. Finally, a β-barium borate, BaB_2O_4 (BBO) crystal combined the fundamental and the second harmonic by sum-frequency generation, producing the third harmonic of the Ti:sapphire 744 nm seed light at 248 nm.

Following the tripler, a fused silica prism pair pulse stretcher provided control of the pulse width in the range between 200 fs and 2 ps, and also provided a spatial filter for the residual fundamental and second harmonic radiation, which were refracted out of the beam path. The

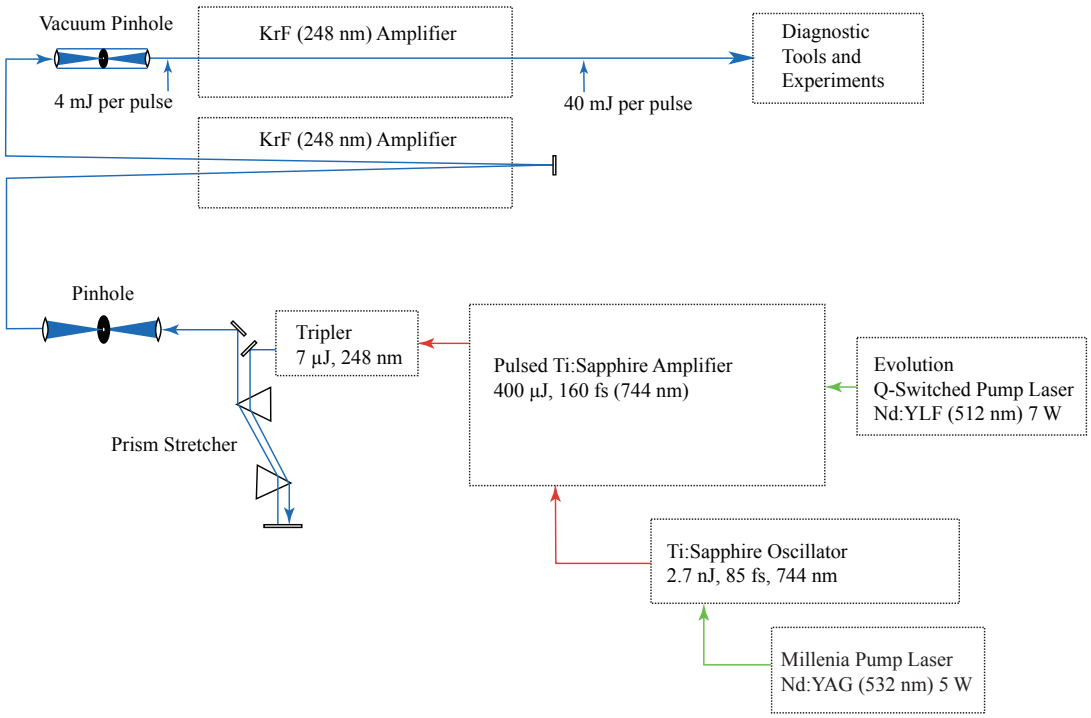

Figure 3.2: Schematic of the ultraviolet femtosecond laser system.

ultraviolet seed passed twice through a KrF excimer amplifier, and then passed through a vacuum pinhole for the purpose of spatial mode filtering and to reduce amplified spontaneous emission (ASE). The pinhole must be in vacuum because the intensity is sufficiently high that focusing in air would result in self-phase modulation (SPM), thus altering the pulse frequency spectrum and reducing beam quality. A final amplifier pass produces 40 mJ pulses at a repetition rate of 10 Hz. A dielectric mirror designed for maximum reflection at zero degrees turns the beam at 45° and was determined by calibration to transmit ≈2% of the beam, which was measured with a photodiode to monitor pulse energy.

The large number of individual laser units required to produce high power UV laser pulses necessitated a precise timing system. The system was synchronized by a fast pho-

todiode monitoring the output from the Ti:sapphire oscillator, and after amplification, this signal provided an trigger signal to a Stanford Research Systems DG535 Digital Delay/Pulse Generator which, in turn, triggered the Q-switched pump and the Pockels cells for the regenerative amplifier. This first DG535 Generator also provides a synchronization signal to a second DG535 which controlled the timing of the the two excimer laser amplifiers. Precise temporal alignment of the excimer gas discharge with the UV seed pulse is essential for high-power operation. In addition, the high-voltage switches in the excimers which produce the gas discharge gain region, called thyratrons, have a discharge jitter of a least 2 ns, and this synchronization system had the capability for minute adjustment to maintain high power over several hours as data was acquired. To illustrate the effect of the thyratron jitter, two laser shots are shown in Fig. 3.3, transmitted through the angled zero-degree mirror described above. The narrow peak is the sub-picosecond pulse, while the broad signal on both sides is the emission from the amplifiers that is not absorbed by the seed. The red line shows a laser pulse in which the seed was well-aligned with the excimer discharge, while the black line shows a pulse in which the discharge is slightly in advance of the arrival of the seed pulse, resulting in the seed pulse arriving after the peak of the amplifier discharge. It is likely that the photodiode was saturated during these measurements and does not show a peak energy difference between the two pulses, but typically the pulse energy was decreased by as much as 50% by such a misalignment.

The resulting laser pulses were focused with a 1.5 m focal length concave mirror. Clearly visible excitation channels are produced by the focused laser beam in air, extending approximately half a meter on either side of the focal point. To verify the production of a plasma along the laser beam, a handheld Tesla coil was modified to discharge when synchronized with the laser. The picture in Fig. 3.4 was captured by a digital camera set to a 1 s shutter speed, and illustrates two laser pulses and two coil discharges. In the absence of the laser pulse, the Tesla coil produced an arc across a gap of $\approx$1 cm. With the addition of the ionized channel of the laser pulse, the same voltage will discharge across $\approx$3 cm. This increase in

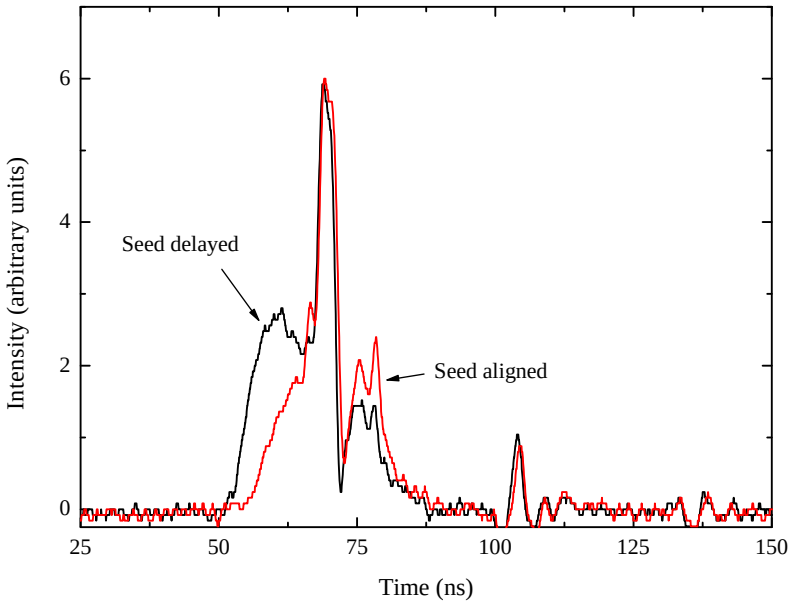

Figure 3.3: Two laser pulses transmitted through an angled zero-degree dielectric mirror (2% transmission) in which the seed pulse is well-aligned (red line) with the excimer amplifier discharge, and delayed from the discharge (black line).

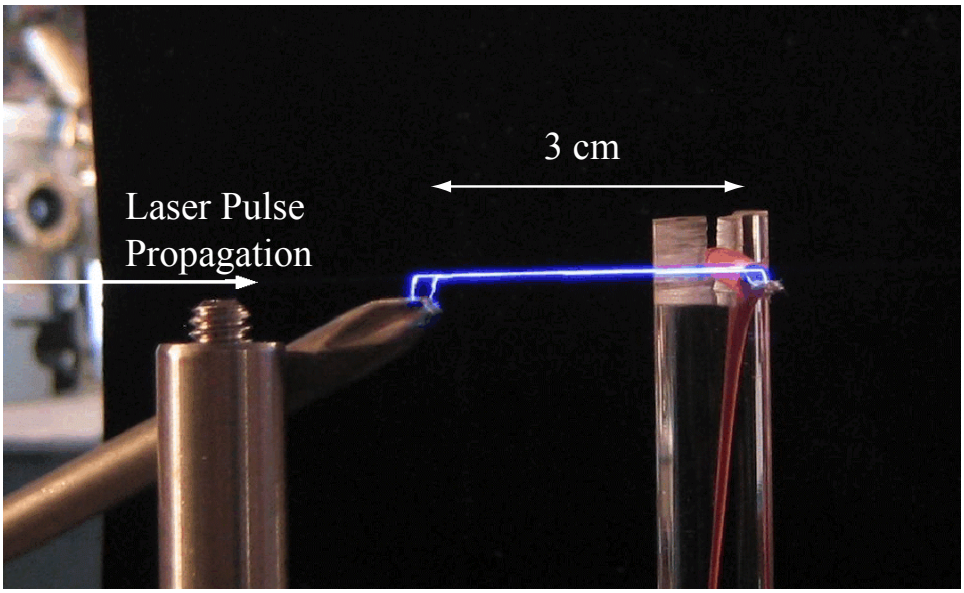

Figure 3.4: Digital photograph of two discharges from a triggered handheld Tesla coil along the path ionized by the laser pulse.

conductivity of the air channel is a dramatic demonstration of the ionization power of the laser pulse.

3.2 Microwave Interferometer

3.2.1 Waveguide and Components

Microwave interferometry operates on the same principles as many more commonly encountered optical wavelength interferometry methods. Microwaves from a single source are split into two parts and directed through two pathways before being recombined at a detector. One of the pathways is perturbed by the laser-induced plasma, and this perturbation can be analyzed by the interference between the microwaves that traveled on the reference pathway and the microwaves that interacted with the plasma.

The interferometer in this experiment operated in what is referred to as the X-band frequency region, which ranges from 8 to 12 GHz, and was constructed from WR-90 rectangular rigid waveguide. Standard rectangular waveguide is sized according to the specified frequency band such that the lowest frequency is supported, and the highest frequency in the range indicates the point in the frequency spectrum above which more than one frequency mode can be transmitted. The X-band waveguide has interior dimensions of 0.900×0.400 inches, or 2.286×1.016 cm, and is traditionally constructed of brass with a silver plated interior for maximum conductivity. A straight section of X-band waveguide is shown in Fig. 3.5. The circular ridges visible around the rectangular opening are engineered to reduce coupling losses at waveguide junctions.

For the diagrams that follow in this section, circuit diagrams are used that include symbols that may be unfamiliar, so a legend of the microwave symbols is shown in Fig. 3.7, and the components to which they refer are described below. The klystron is the microwave source, in which a high voltage cavity accelerates bunches of electrons past a pickup loop to produce microwaves. A uniline is a magnetic signal isolator that is used to eliminate

Figure 3.5: Sample straight section of X-band waveguide.

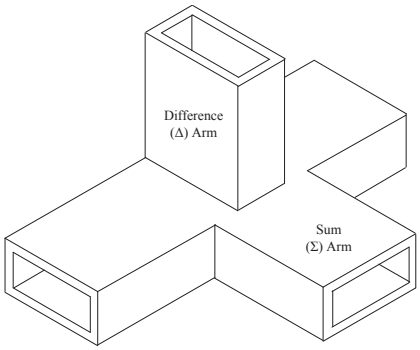

Figure 3.6: Outline drawing of a magic-tee junction.

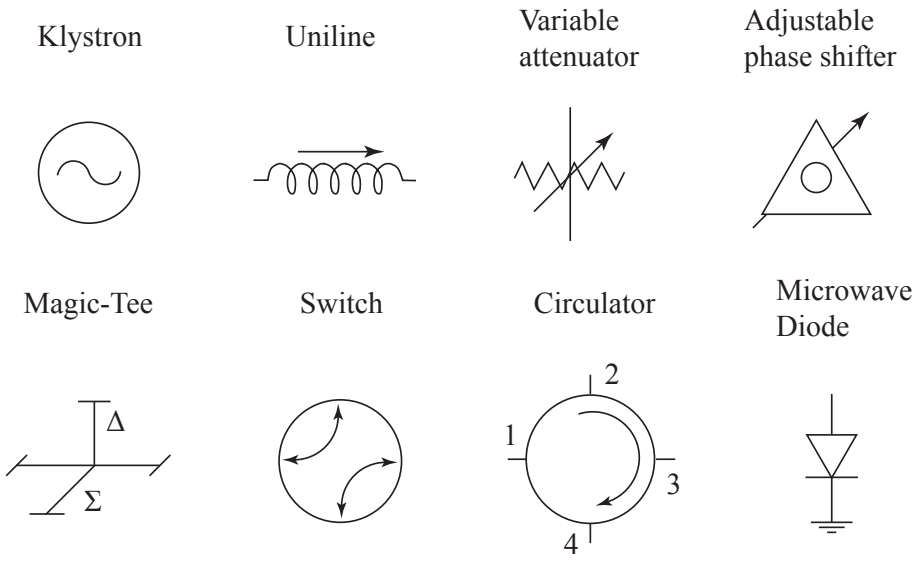

Figure 3.7: Microwave circuit diagram symbols.

reflections that would corrupt the signal, functioning as a microwave diode that allows transmission in only one direction. The microwave switch has two waveguide bends on a rotating knob, allowing fast, repeatable changes to waveguide structure which would otherwise require time-consuming reconstruction. A circulator is a complex component that transmits signal in a clockwise fashion: a signal entering port 2 exits at port 3, similarly around the device. This is extremely useful for monitoring reflection signals; for example if a signal exits port 2 and reflects back, the reflection will be transmitted to port 3. The most important

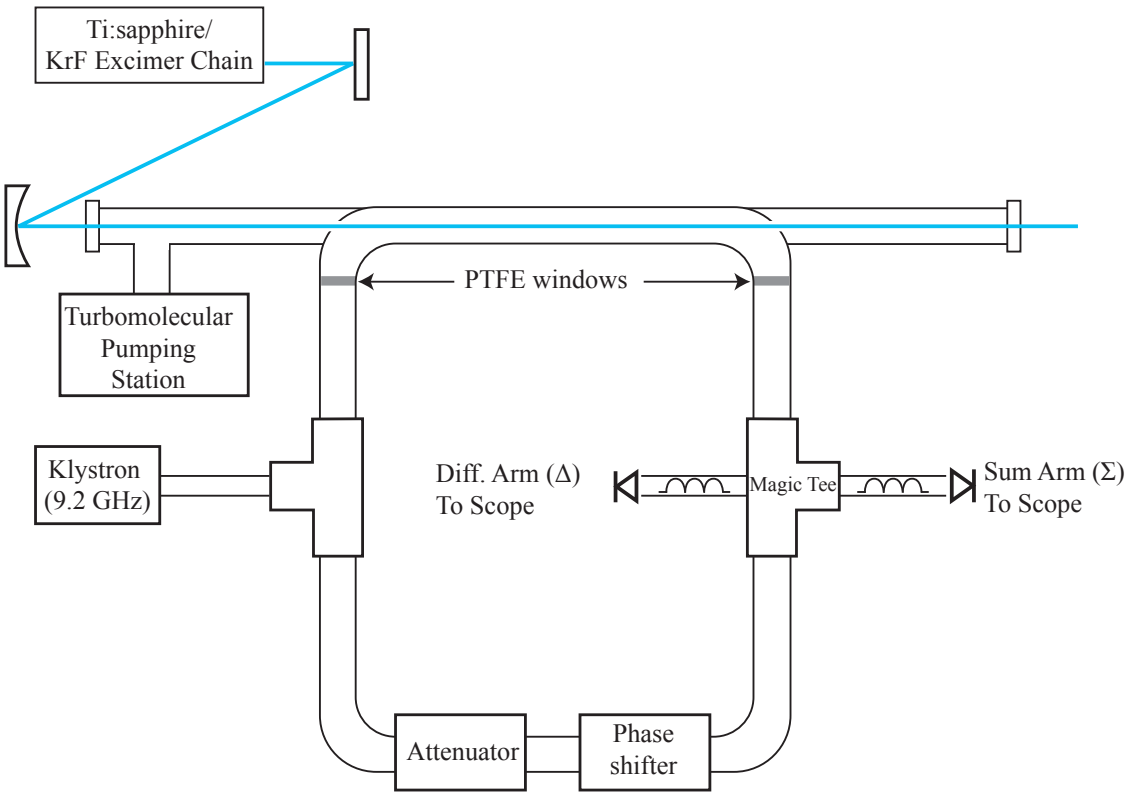

Figure 3.8: Diagram of the full-bridge microwave interferometer.

component that is used here is the magic- or hybrid tee, which is shown in Fig. 3.6. The two unlabeled arms shown in the diagram are the input ports, and the two perpendicular arms are the sum (Σ) and difference (Δ) output ports. As the names indicate, these arms transmit the sum and difference of the signals coming into the two input arms. This is useful because microwave diode detectors only measure the integrated microwave electric field intensity, and all phase information is lost. With the sum and difference measurements, however, both amplitude and phase information can be extracted, as is discussed further in Sec. 4.2.

The interferometer is a construction commonly referred to as a "full-bridge", and is illustrated in Fig. 3.8. This diagram is not a circuit diagram, in order to better indicate the

non-waveguide elements of the experiment. The output of a klystron operating at 9.2 GHz was split into two equal beams by a tee, and one entered the experimental arm, which is described further below. The other microwave beam entered a reference arm, along which an attenuator and phase shifter were adjusted to balance with the experimental arm in the absence of any plasma formation. The microwaves exiting these two arms are recombined in a magic-tee, and the sum and difference ports of the magic-tee were used to extract the phase shift and attenuation between the reference and experimental arms. The time evolution of the attenuation and phase shift due to the plasma production and decay was measured by power-voltage calibrated microwave diodes. This is described in more detail in Section 4.2.

As mentioned in the introduction to Chapter 3, the waveguide in part of the interaction arm of the interferometer was vacuum sealed. Sections of brass and stainless steel pipe were welded to the waveguide bends, and the ends of the pipe were sealed with UV-grade fused silica vacuum windows. The waveguide sections were sealed to each other by placing a viton o-ring in the circular grooves visible in Fig. 3.5. The vacuum region was isolated from the rest of the interferometer by polytetrafluoroethylene (PTFE), commonly known as Teflon®, windows. Glass was used initially, but was found to reflect almost 50% of the signal; PTFE is impermeable, vacuum safe and has negligible insertion loss. Flat disks were cut from a 1/16" thick sheet of PTFE to fit inside the raised circular ridge on the face of the waveguide connection. Vacuum grease on both the PTFE and the o-rings ensured a good seal.

To prevent damage to the end windows from the high intensity of the focused laser beam, the waveguide section was extended on both sides by three foot sections of stainless steel pipe (this is not to scale in the diagram). The experimental arm and extension pipes were pumped to a base pressure of 1×10^{-5} Torr by a turbomolecular pumping station to remove impurities, especially oxygen, as its fast attachment rates would prevent accurate studies of gases with slower recombination times. A gas handling system allowed the controlled introduction of the desired gas into the vacuum sealed section of the interferometer. Two Baratron® Gauge Capacitance Manometers were used to monitor the pressure, one at 1000 Torr full scale and

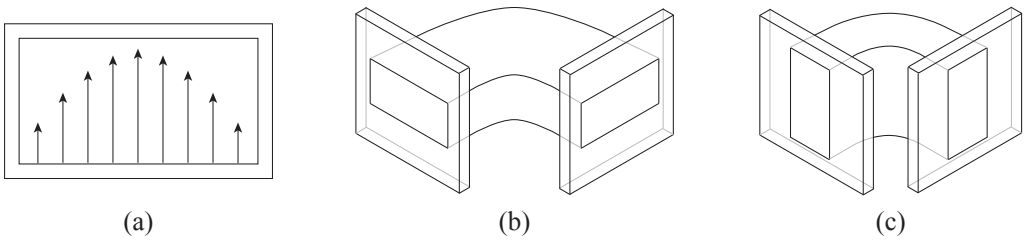

Figure 3.9: (a) Cross-section of waveguide showing the electric field strength. Note the field vanishes at the short sides. (b) Waveguide H-bend. (c) Waveguide E-bend.

one at 100 Torr full scale, for accurate pressure measurements in the range $10^3 - 10^{-2}$ Torr.

In order to couple the laser beam into the waveguide, it was necessary to drill holes in waveguide bend sections. Rectangular waveguide can be bent along one of two axes, creating an E-bend or an H-bend. Figure 3.9 shows a cross section of the electric field amplitude and outline diagrams of the two types of waveguide bends. The critical walls of the waveguide are the short sides, as the conductivity must be high enough to short out the electric field. For this reason, holes were drilled in an E-bend section, where the hole would be on the long side of the rectangle. Transmission tests showed negligible losses for the $\approx 3/8$" holes that were drilled.

3.2.2 Characterization and Calibration

This type of microwave bridge interferometer is no longer common in academic scientific studies, so extensive characterization was done to ensure correct operation of all the components. Uniline isolators were tested for reflection and backward transmission, circulators and switches were tested for reflection and transmission, and splitters and tees were tested to ensure they split the input signal equally between the two output ports. The variable attenuator and phase shifter were fitted with stepper motors and calibrated potentiometers to enable computer control and readout of the position. All power readings in the following tests were taken with an HP 437B power meter and an HP 8481A microwave sensor module.

The first critical test was to determine the calibration of the microwave diodes. Microwave

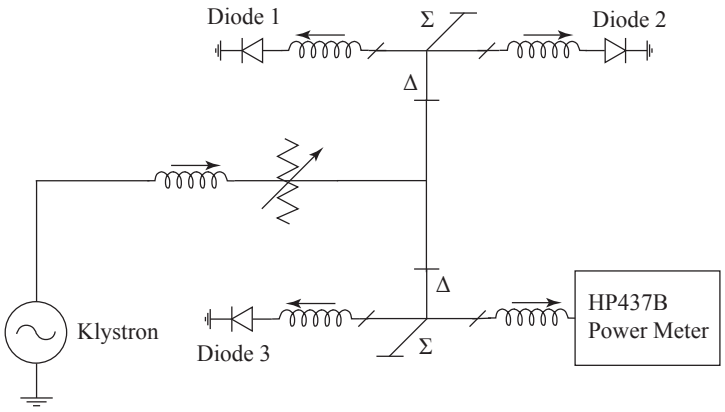

Figure 3.10: Circuit diagram for measuring the calibration curves for three diodes simultaneously with one power meter.

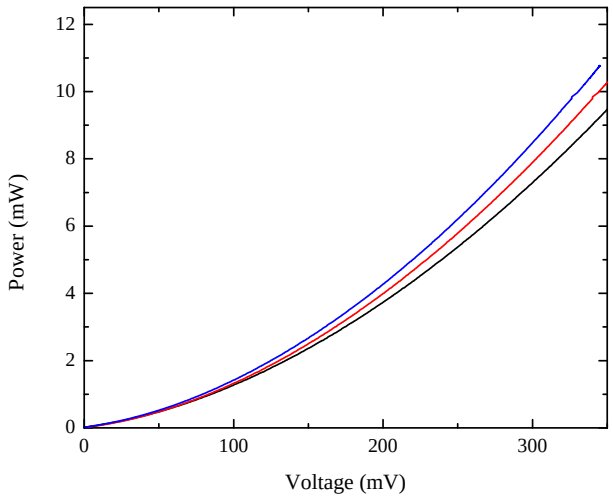

Figure 3.11: Representative diode calibration curves for three model 1N23E diodes.

diodes are read out in voltage, so calibration is necessary to determine the corresponding microwave power in watts. Even though several diodes with identical model numbers were used, the calibration was discovered to be different for each one, which necessitated measurement of power/voltage curves for each diode. The circuit in Fig. 3.10 was used to measure the curves for three diodes simultaneously, and sample calibration curves are shown in Fig. 3.11.

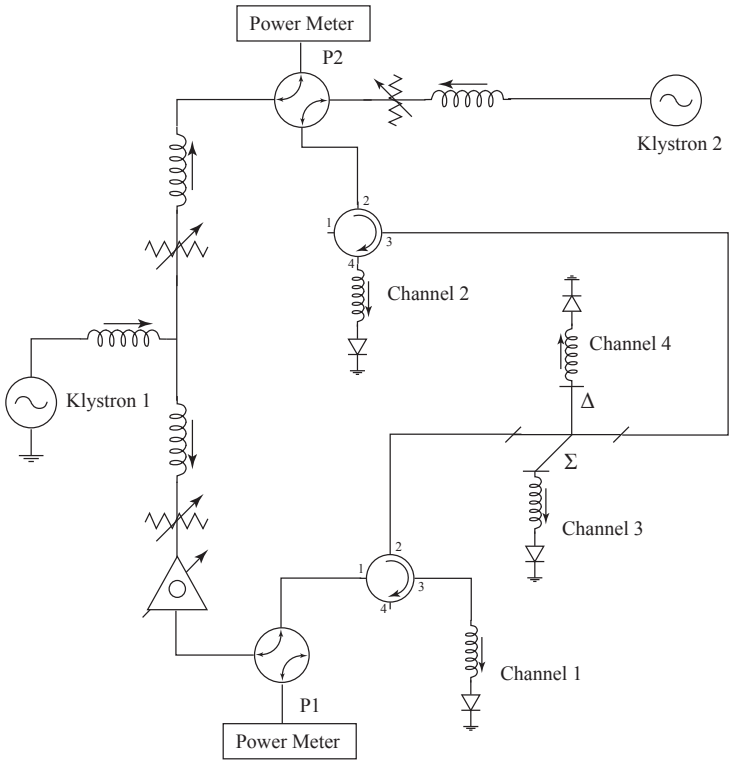

Figure 3.12: Circuit used to test the frequency response of the magic-tee. Note the two klystron sources and channel labels.

Because the laser-induced plasma was expected to produce signals on a very short time scale (≈5 ns for atmospheric pressure in air), it was important to verify the bandwidth of some of the components. Data was collected using a Tektronix TDS5104B 1 GHz Digital Phosphor Oscilloscope, which has a mainframe bandwidth of 1 GHz, so all measurements are averaged over 1 ns by the scope, but tests were done to ascertain whether the bandwidth of any components were lower than that. The complex tuning required for the magic-tee to operate necessitated careful testing to determine the bandwidth response. To simulate a high speed signal, a circuit was constructed that used two klystron sources tuned to different frequencies to create a beat signal at the magic-tee, as is shown in Fig. 3.12. Table 3.1 summarizes the tests that were conducted, listing the settings for the two klystrons for each test, their relative power, and the expected beat frequency.

As is evident from the sample beating data in Fig. 3.13, output on channels 1 and 2 are

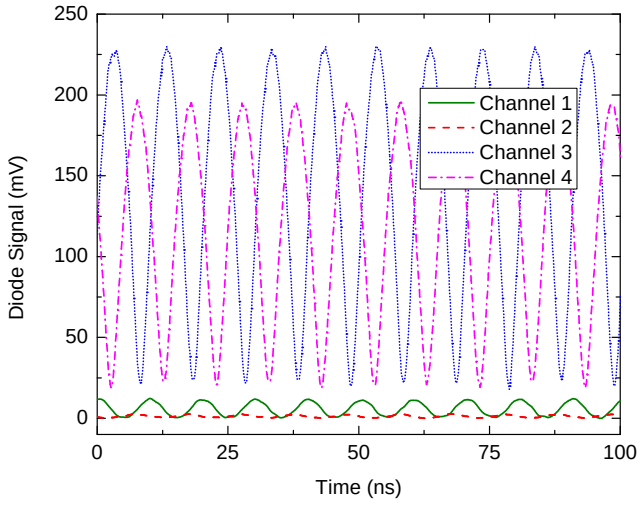

Figure 3.13: Sample beating data. Channels indicated are the same as the labels on Figure 3.12.

f_1 (GHz)	f_1 Power (mW)	f_2 (GHz)	f_2 Power (mW)	beat frequency (MHz)
9.9	5.24	9.8	4.49	100
9.3	5.24	10.1	11.4	800
9.5	3.17	10.1	11.4	600
9.2	2.5	10.1	11.4	900

Table 3.1: Table of klystron frequencies tested, their relative powers, and the expected beat frequencies.

negligible compared to the signals transmitted to the sum and difference arms (channels 3 and 4). This is expected, as those two channels measure the sum of any reflected microwave signal and microwaves that are transmitted straight through the tee instead of diverted to the two outputs. To determine if the the magic-tee was responding appropriately, Fourier transforms were performed on the beating data, recorded on the sum arm of the magic-tee; the signal from the difference arm would give the same information, as the phase shift and amplitude difference does not affect the frequency information. The first set of data, shown in Fig. 3.14, includes data for beat frequencies Δf of 100 MHz and 600 MHz, and at these frequencies, the beating signal occurs at the correct value in the corresponding

Fourier transform. In Fig. 3.15, data for larger frequency shifts is shown, specifically beat frequencies Δf of 800 MHz and 900 MHz. As the Fourier transforms show (on the right), the beating signal peak does not occur at the expected frequency. For $\Delta f = 800$MHz, the beating occurs at ≈ 200 Mhz, and for $\Delta f = 900$MHz, the beating occurs at ≈ 350 Mhz. It can be concluded from this that for frequency shifts larger than 800 MHz, the magic-tee does not transmit an accurate signal.

Given that the TDS5104B oscilloscope has only a 1 ns mainframe bandwidth, there was some question whether it might be the scope or the microwave diodes limiting the response time, which would not be detected by the oscilloscope. During another operation of the interferometer, data was acquired using a Tektronics DSA70804 Digital Serial Analyzer, which had a mainframe bandwidth of 8 GHz. Data recorded by this scope showed a large noise component at the microwave signal frequency of 9.2 GHz, which indicated that the microwave diode was not limiting the frequency response of the interferometer measurements. Figures 3.16 and 3.17 show representative data from this experiment, before and after filtering out the 9.2 GHz signal, and a Fourier transform of the unfiltered data, showing the large peak at 9.2 GHz. Given that the magic-tee transmission was unreliable above 800 MHz, and the TDS 5104B oscilloscope has a bandwidth of 1 GHz, we conclude that the magic-tee is the time-response limiting factor.

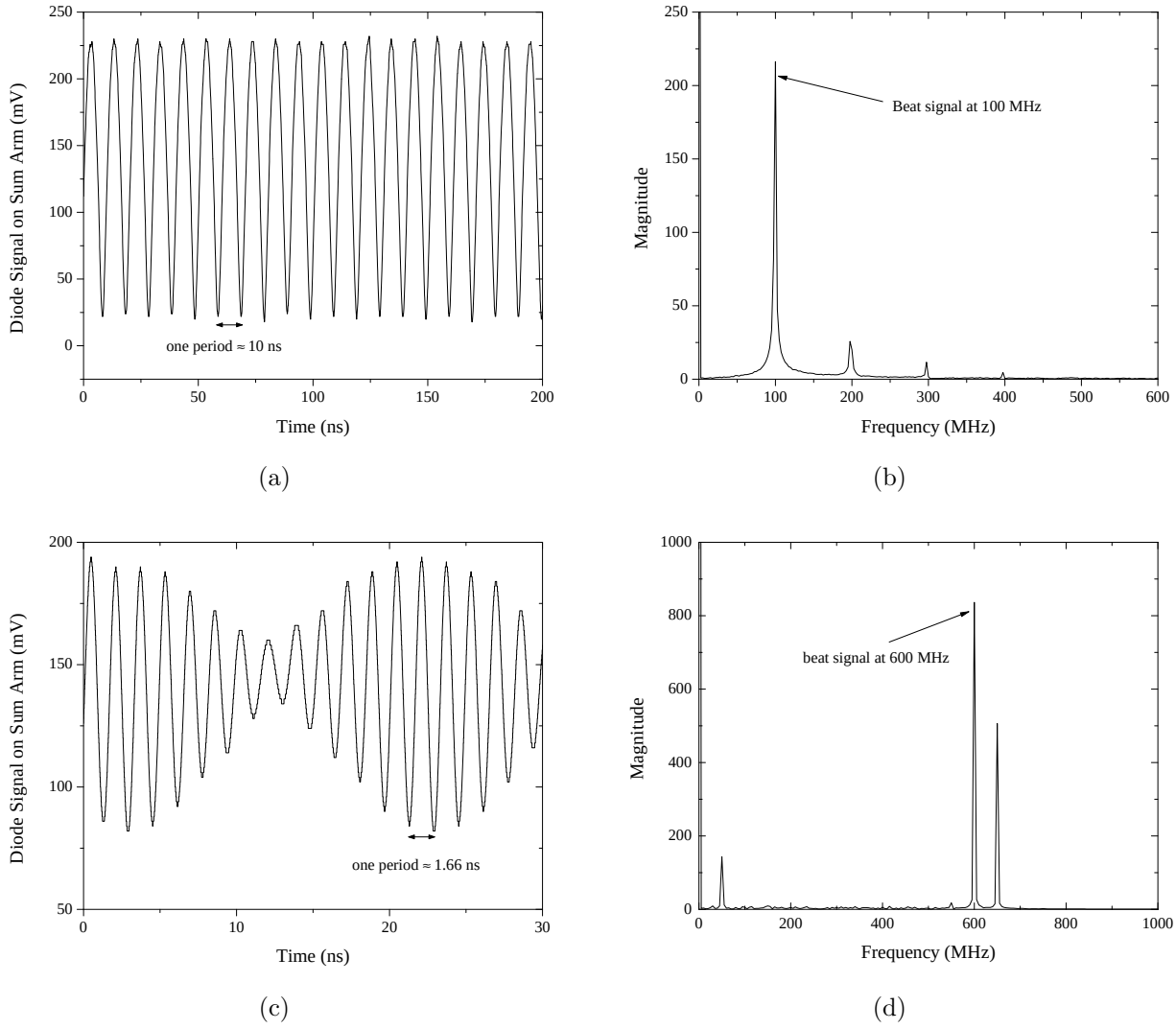

Figure 3.14: Diode signal from the sum arm of the magic-tee for Δf of 100 MHz (top) and 600 MHz (bottom). On the right are the Fourier transforms of the data on the left, showing the beating signal peak at the expected value.

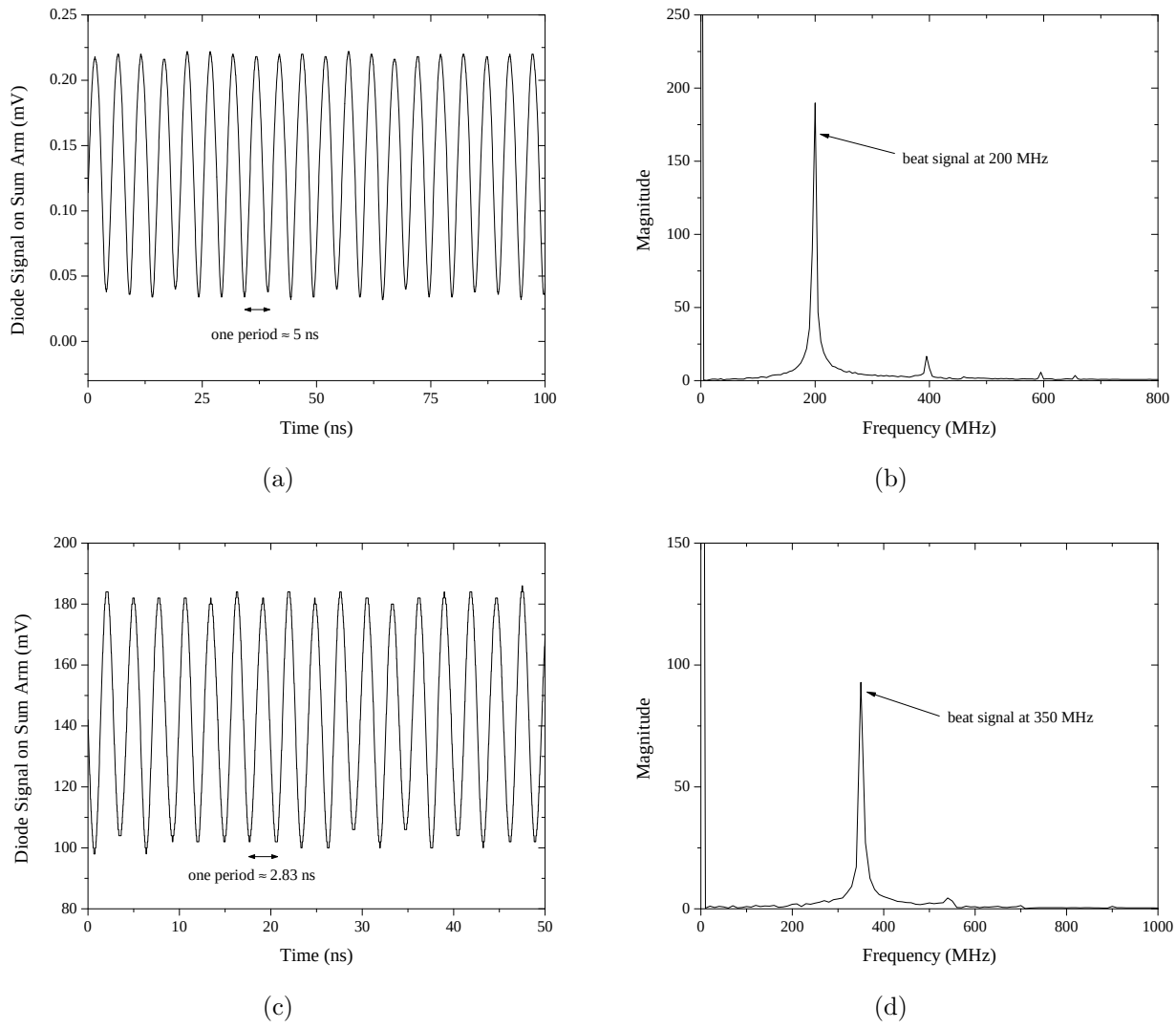

Figure 3.15: Diode signal from the sum arm of the magic-tee for Δf of 800 MHz (top) and 900 MHz (bottom). On the right are the Fourier transforms of the data on the left, showing the beating signal peak at a lower frequency than expected.

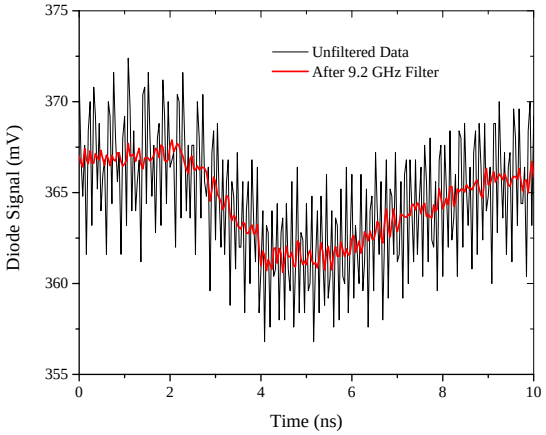

Figure 3.16: Sample data from the data run using the DSA70804, before (black) and after (red) filtering the 9.2 GHz noise.

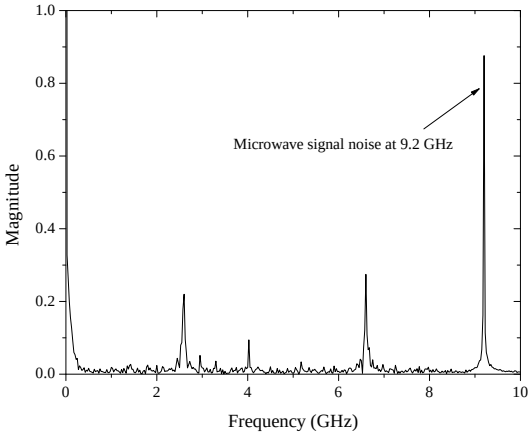

Figure 3.17: Fourier transform of unfiltered data, showing 9.2 GHz peak.

Chapter 4

Microwave Interferometer Analysis

4.1 Theory

For an electromagnetic wave propagating in a waveguide partially filled with a plasma, the magnitude of the complex propagation constant $\gamma = \alpha + \imath\beta$ is given by

$$\gamma^2 - \gamma_0^2 = \imath\omega\mu_0 \frac{\int\int \mathbf{E}_0 \cdot \mathbf{J}\, dA}{\int\int \mathbf{E}_0 \cdot \mathbf{E}\, dA}, \tag{4.1}$$

where γ_0 and $\mathbf{E_0}$ are the propagation constant and electric field in the empty waveguide, respectively, $\mathbf{E}$ is the electric field in the presence of the plasma, ω is the radian frequency of the microwave field, and $\mathbf{J}$ is the current density. For an arbitrary plasma, the current density is expressed as:

$$\mathbf{J} = \sigma\mathbf{E} = \frac{ne^2}{m}\,\frac{\nu - \imath\omega}{\nu^2 + \omega^2}, \tag{4.2}$$

where m is the electron mass and ν is the collision frequency in the plasma. Because n, the electron density, is spatially dependent, it must remain within the integrand of Eqn. 4.1. In an evacuated waveguide, the propagation constant is purely imaginary, and, hence, $\gamma_0 = \imath\beta_0$. Therefore, Eqn. 4.1 reduces to

$$\gamma^2 + \beta_0^2 = \imath\omega\mu_0 \frac{e^2}{m}\,\frac{\nu - \imath\omega}{\nu^2 + \omega^2}\,\frac{\int\int n\mathbf{E}_0 \cdot \mathbf{E}\, dA}{\int\int \mathbf{E}_0 \cdot \mathbf{E}\, dA}. \tag{4.3}$$

Assuming the collision frequency is much less than the microwave field frequency ($\nu \ll \omega$) and expanding γ in terms of α and β, Eqn. 4.3 becomes

$$\alpha^2 - \beta^2 + \beta_0^2 + 2\imath\alpha\beta = (\omega - \imath\nu)\,\frac{\mu_0 e^2}{m\omega}\,\frac{\int\int n\mathbf{E}_0 \cdot \mathbf{E}\,dA}{\int\int \mathbf{E}_0 \cdot \mathbf{E}\,dA}. \tag{4.4}$$

For simplicity, the electron density is defined as $n = n_e\,f(x,y)$, where n_e is an electron density scaling factor in the plasma region and $f(x,y)$ represents the spatial variation of the plasma in the plane transverse to the propagating microwave field. We also assume that $\mathbf{E} \approx \mathbf{E_0}$. The integral ratio in Eqn. 4.3 is then defined as the filling factor F

$$F = \frac{\int\int f(x,y)\mathbf{E}_0^2\,dA}{\int\int \mathbf{E}_0^2\,dA}. \tag{4.5}$$

Since the electron plasma frequency is given by $\omega_p = n_e e^2/m\epsilon_0$, and $c^2 = 1/\epsilon_0\mu_0$, then Eqn. 4.4 can be separated into real and imaginary parts:

$$\alpha^2 - \beta^2 + \beta_0^2 = \frac{\omega_p}{c^2}\,F \tag{4.6}$$

$$2\alpha\beta = \frac{\omega_p}{c^2}\frac{\nu}{\omega}\,F. \tag{4.7}$$

Consequently, to determine experimentally the electron density, we only need Eqn. 4.6. Expressing Eqn. 4.6 in terms of n_e yields:

$$n_e = \frac{1}{F}\,\frac{m}{\mu_0 e^2}(\alpha^2 - \beta^2 + \beta_0^2). \tag{4.8}$$

The plasma propagation constants α and β are related to the measured phase shift, $\Delta\phi$ (in radians), and the measured attenuation, a (expressed in dB), and the vacuum propagation constant, β_0, which is calculated from the dimensions of the waveguide (2.286 $\times$ 1.016 cm) by the relation:

$$\beta_0 = \left(\frac{\omega^2 - \omega_0^2}{c^2}\right)^{1/2} = 1.35\,\mathrm{cm}^{-1}, \tag{4.9}$$

where ω is the microwave frequency (9.2 GHz in the present experiment), and ω_0 is the low frequency cutoff for the X-band waveguide. The lower cutoff is related to the dimensions of the waveguide by the relation $f_{cutoff} = c/2a$, where a is the dimension of the broader wall of the waveguide. For X-band waveguide, $a = 2.286$ cm, so $f_{cutoff} = 6.557$ GHz. From β_0, we calculate

$$\beta = \beta_0 - \frac{\Delta\phi}{L} \tag{4.10}$$

$$\alpha\,(\text{expressed in Nepers/cm}) = \frac{\ln 10}{20}\frac{a\,(\text{in dB})}{L}, \tag{4.11}$$

where L is the interaction length in centimeters. The Neper (Np) is similar to the decibel (dB), being a unitless measure of ratios, with the difference that decibels are measured on a logarithmic scale with base 10, while Nepers use base e. The attentuation and phase shift measured in these experiments with the interferometer are converted to electron density n_e using these equations.

As discussed in Sec. 2.2, it is of interest to determine the detection limit of the measurement technique. The lower bound will be a low density plasma, in which it can be assumed that the attenuation is zero. With $\alpha = 0$ and substituting Eqn. 4.10 for β, Eqn. 4.8 reduces to

$$n_e = \frac{1}{F}\frac{m}{\mu_0 e^2}(\beta_0\frac{\Delta\phi}{L} - \left(\frac{\Delta\phi}{L}\right)^2). \tag{4.12}$$

With a conservative estimate for the minimum detectable $\Delta\phi$ of 20°, and assuming a filling factor of 0.1 and $L = 1$ m, the minimum detectable electron density is $\approx 10^{10}$ cm^{-3}.

4.2 Interferometer Calculations

As described in Sec. 3.2, the magic-tee combines the microwave amplitudes from the reference and experimental arms. The sum (Σ) arm transmits the two inputs summed without a phase shift. In contrast, the difference (Δ) arm transmits the two inputs summed with a π phase

shift on one input, essentially producing the difference of the two inputs. The intensity signals of the two output ports of the magic-tee are measured by calibrated microwave diodes. These intensities are given by the relations:

$$I_\Sigma = E_\Sigma^2 = (E_{\rm exp} + E_{\rm ref})^2 \tag{4.13}$$

$$I_\Delta = E_\Delta^2 = (E_{\rm exp} - E_{\rm ref})^2. \tag{4.14}$$

The phase and attenuation in the reference arm were adjusted so that the two arms had the same amplitude and yet are 90° out of phase. This was done by adjusting the phase shifter and attenuator of the reference arm until one diode signal was nulled (zero). In this situation, the electric fields propagating in the two arms of the interferometer had identical amplitudes and were 180° out of phase. The phase shifter was then adjusted until the other diode signal was nulled (zero). The 90° phase shift point lies halfway between these settings.

The general form of the microwave amplitude in each arm is then given by E_{ref}, the electric field amplitude in the reference arm, and E_{exp}, the electric field amplitude in the experimental arm:

$$E_{\rm ref} = A_r \sin(\omega t) \tag{4.15}$$

$$\text{and } E_{\rm exp} = A_p(t) \cos(\omega t + \delta(t)), \tag{4.16}$$

where $A_p(t)$ is the time dependent amplitude in the experimental arm, which provides attenuation information, and $\delta(t)$ is the time dependent phase, which provides phase shift information. To solve for these, we write the electric field at the sum arm as

$$\sin(\omega t) + \cos(\omega t + \delta) = A_\Sigma \sin(\omega t + b_\Sigma), \tag{4.17}$$

and then determine A_Σ and b_Σ. Expanding the left side of Eqn. 4.17 and grouping separately

the sin and cos terms (letting $\theta = \omega t$ and ignoring the time dependence), we find that:

$$\begin{aligned} A_r \sin\theta + A_p \cos\theta \cos\delta - A_p \sin\theta \sin\delta &= A_\Sigma \left(\sin\theta \cos b_\Sigma + \cos\theta \sin b_\Sigma\right) \\ \sin\theta : A_r - A_p \sin\delta &= A_\Sigma \cos b_\Sigma \qquad (4.18) \\ \cos\theta : A_p \cos\delta &= A_\Sigma \sin b_\Sigma, \\ A_\Sigma &= \sqrt{A_p^2 + A_r^2 - 2A_p A_r \sin\delta}, \qquad (4.19) \\ \text{and } b_\Sigma &= \sin^{-1}\left(\frac{A_p \cos\delta}{A_\Sigma}\right). \qquad (4.20) \end{aligned}$$

By a similar procedure,

$$\begin{aligned} A_\Delta &= \sqrt{A_p^2 + A_r^2 + 2A_p A_r \sin\delta}, \qquad (4.21) \\ \text{and } b_\Delta &= \sin^{-1}\left(\frac{-A_p \cos\delta}{A_\Delta}\right). \qquad (4.22) \end{aligned}$$

Inserting these into equations 4.13 and 4.14 and, by suitably combining the signals from the sum and difference arms, we can extract $A_p(t)$ and $\delta(t)$ as follows:

$$\begin{aligned} A_p^2(t) &= \frac{I_\Delta(t) + I_\Sigma(t)}{2} - A_r^2 \qquad (4.23) \\ a(t)(\text{in dB}) &= 10 \log_{10}\left(\frac{A_p^2(t)}{A_r^2}\right) \qquad (4.24) \\ \sin\delta(t) &= \frac{I_\Delta(t) - I_\Sigma(t)}{4A_p(t)A_r}. \qquad (4.25) \end{aligned}$$

With no plasma present in the experimental arm, at times $t < 0$, with $t = 0$ defined as the onset of the plasma in the experimental arm, the phase shift $\delta(t)$ is equal to zero, and the amplitude in the experimental arm is equal to the amplitude in the reference arm,

$A_p(t) = A_r$. Inserting this into Eqn. 4.23, we can determine A_r as follows:

$$\begin{aligned} A_p^2(t) = A_r^2 &= \frac{I_\Delta(t<0) + I_\Sigma(t<0)}{2} - A_r^2 \\ 4A_r^2 &= I_\Delta(t<0) + I_\Sigma(t<0). \end{aligned} \tag{4.26}$$

4.3 Representative Data and Analysis

To illustrate the procedure adopted for interpreting the data more concretely, representative data are presented here. For simplicity, this data are recorded in 300 Torr of argon. Figure 4.3 shows data from the two arms of the magic tee, after correction for the diode response. Note that the initial values (before the laser pulse at t=0) are the same. This is because the interferometer was balanced at 90°, as mentioned above. Using Eqs. 4.25 and 4.24, the attenuation and phase shift were calculated point by point. The portion of the signal before the trigger is used to calculate the DC value of A_r^2, using Eqn. 4.27. Attenuation and phase data representative of those obtained in these experiments are shown in Fig. 4.2.

To calculate the electron density, we need the phase shift δ. As shown in Fig. 4.2, the sine of the phase shift is given over the range $-1 < \sin\delta < 1$. The arcsin function, is typically defined over the range $-\pi/2 < \delta < \pi/2$, with $\arcsin(-1) = \pi/2$ and $\arcsin(1) = \pi/2$. In our case, negative values of $\sin\delta$ represent δ values greater than $\pi/2$, not values less than zero. Calculating δ this way results in a functional form for the electron density that has a discontinuity at the point where the phase shift equals $\pi/2$. To smooth the data, a simple polynomial fit is made to the curve on either side of the discontinuity, and the discontinuous data is replaced by the fit. This is shown in Fig. 4.3.

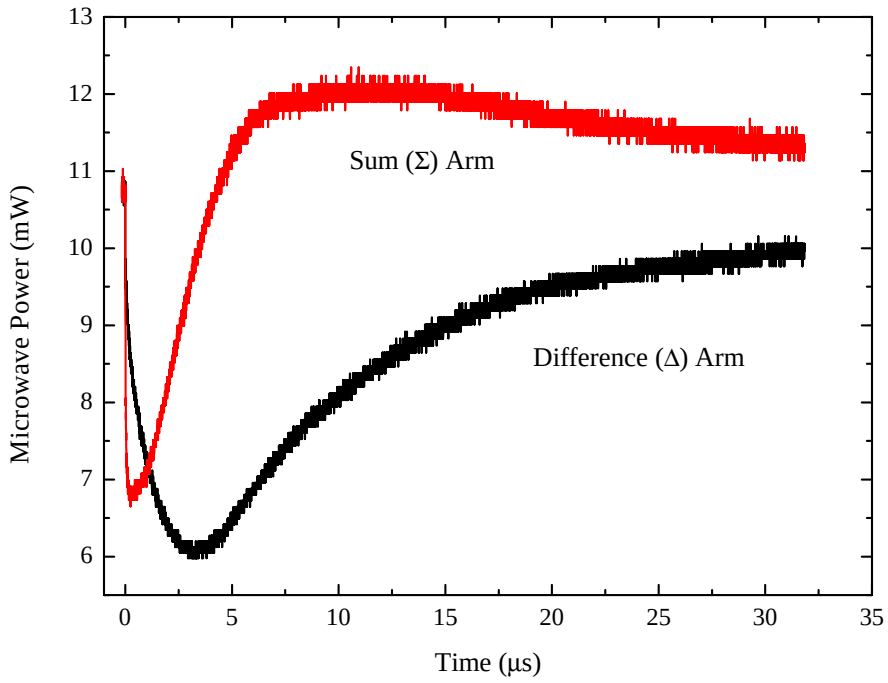

Figure 4.1: Representative data from the two arms of the magic-tee.

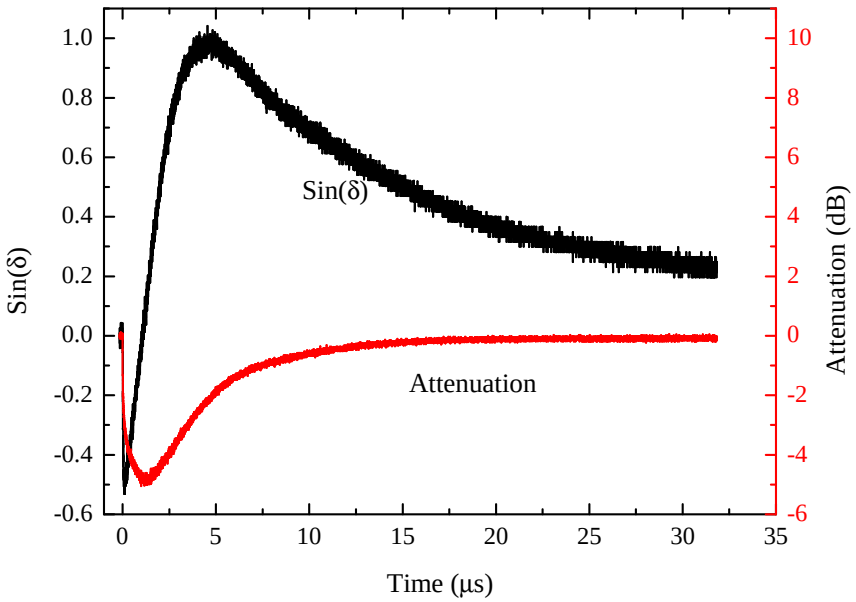

Figure 4.2: Representative data illustrating the temporal variation of the attenuation and the sine of the phase shift (δ).

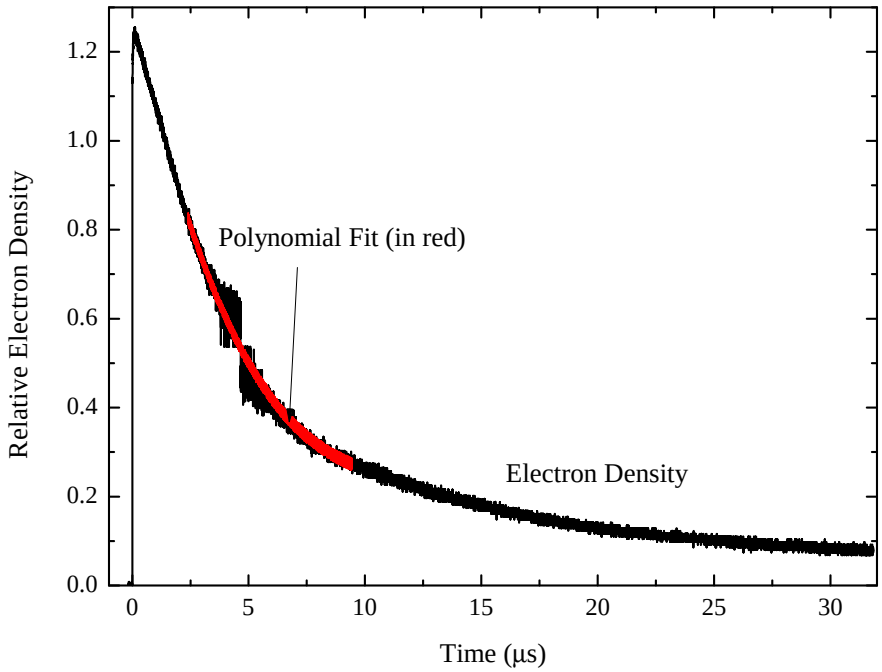

Figure 4.3: Representative electron density measurements showing the fit of a polynomial so as to traverse the region $\delta = \pi/2$ to smooth out the discontinuity due to the limited range of the arcsin function.

4.4 Electron Diffusion

Because the temporal constant for the decay of the electron density in the rare gases, and even in air at pressures below 100 Torr, are on the microsecond time scale, the diffusion of electrons becomes a process that cannot be ignored. Furthermore, this process impacts the electron decay in two ways. First, it changes the filling factor, F, as defined in Eqn. 4.5, because the plasma cross section $f(x, y)$ changes as the electrons diffuse out of the laser-induced channel. Secondly, if the electrons diffuse sufficiently far, they will reach the walls of the waveguide, and be lost.

To calculate the spatial profile of the electron density, the binary diffusion coefficient

$$D \approx \frac{3\pi}{16\sqrt{2}}\,\overline{v}\,l_{mfp} \tag{4.27}$$

is adopted, where $\overline{v}$ is the average velocity of an electron and l_{mfp} is the mean free path of the electrons. The mean free path is the defined by the relation $l_{mfp} = 1/n\sigma$, where n is the number density of particles, an σ is the cross-sectional area of a single particle. The cross section for nitrogen (the most abundant element in Earth's atmosphere) is calculated using the hard sphere approximation. Nitrogen has a radius of 0.71 $\mathring{A}$ [30], and occurs in the atmosphere as the triply-bonded molecule N_2, so the cross-sectional area of the nitrogen molecule is given by

$$\sigma = \pi r^2 = \pi \cdot 2 \cdot (1.42 \times 10^{-8}\text{cm})^2 = 6.33 \times 10^{-16}\text{cm}^2. \tag{4.28}$$

The number density is calculated using the ideal gas law, $PV = NkT$, where P, V, and T are the pressure, volume and temperature, respectively, N is the number of particles, and k is Boltzmann's constant, 1.38×10^{-23} expressed in $J\,K^{-1}$. The number density N/V, after converting units from Pascals to Torr, and calculated at 300 K, is given by

$$n = \frac{kT}{P} = 3.22 \times 10^{16} \cdot (P\,\text{inTorr}). \tag{4.29}$$

Combining Eqns. 4.28 and 4.29, the mean free path can be approximated by the expression

$$l_{mfp}\,(\text{in cm}) \approx \frac{5 \times 10^{-3}}{P(\text{in Torr})}. \tag{4.30}$$

To determine the average velocity of the electrons, the electron energy is taken to be the energy available after multiphoton ionization of the atom. For example, the ionization threshold of neon is 21.5 eV, and 248 nm photons have an energy of 5 eV. Consequently, the ionization of neon requires five photons, which gives a total absorbed photon energy of 25 eV, 3.5 eV is available above and beyond that required to photoionize the atom. Studies of the electron energy spectra of multiphoton ionization processes have shown that the liberated electron gains this energy as kinetic energy [31].

The diffusion of an ensemble of particles described by a density function $\phi(\mathbf{r}, t)$ is given by the diffusion equation

$$\frac{\partial \phi(\mathbf{r}, t)}{\partial t} = D\,\nabla^2 \phi(\mathbf{r}, t), \tag{4.31}$$

where D is the diffusion coefficient from Eqn. 4.27. This equation is also known as the heat equation. The fundamental solution, often referred to as the *heat kernel*, is the solution corresponding to the initial condition of a point source (see Ref. [32] or any partial differential equations textbook). The heat kernel is

$$\Phi(x, t) = \frac{1}{\sqrt{4\pi D t}} \exp\left(-\frac{x^2}{4Dt}\right). \tag{4.32}$$

Owing to symmetry considerations, only diffusion in the plane transverse to the optical axis of the photoionization source is of interest. Furthermore, the temporally varying diffusion profiles are assumed to be azimuthally symmetric. Thus, the diffusion calculation can be carried out in only one dimension, the radius from the center of the waveguide, r. To obtain a general solution for the initial condition $u(x, t = 0) = g(x)$, the convolution integral

$$u(x, t) = \int_{-\infty}^{\infty} \Phi(x - y, t) g(y) dy \tag{4.33}$$

is calculated for which the initial electron profile, is assumed to be a Gaussian with a full width (FWHM) of $\sigma = 0.5$ mm. The latter was estimated from the visible emission profile of the plasma channel. The integral of Eqn. 4.33 yields a Gaussian with FWHM $\sigma = \sqrt{d^2 + 2Dt}$, where d is the initial value of σ to give a FWHM of 0.5 mm.

To calculate the filling factor F as a function of time, the integral of Eqn. 4.5 is evaluated for $f(x, y)$ equal to a two-dimensional Gaussian, and the electric field

$$E_y = \cos\left(\frac{\pi x}{a}\right) - \frac{b}{2}, \tag{4.34}$$

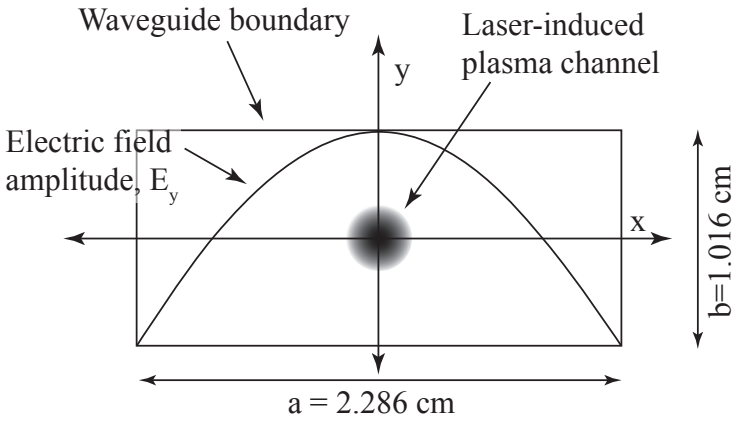

Figure 4.4: Diagram of X-band waveguide showing axis orientation, electric field amplitude, and the location of the plasma channel used for diffusion calculations.

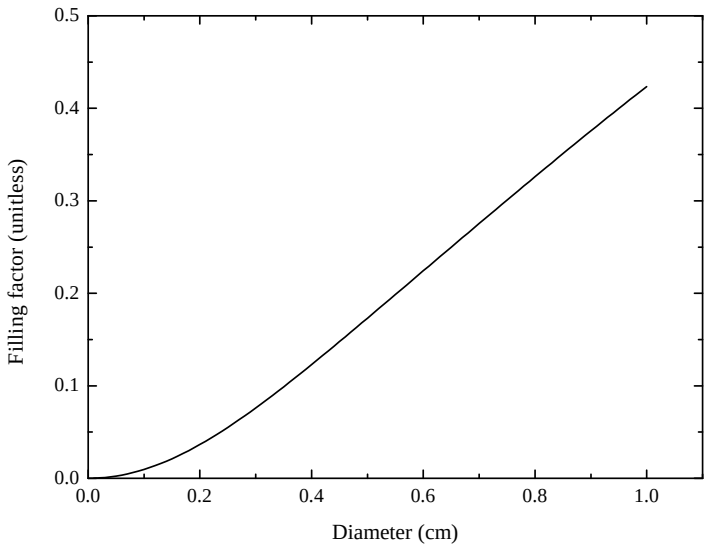

Figure 4.5: Filling factor as a function of diameter of plasma channel, as defined in Eqn. 4.5.

where a and b are the interior dimensions of the waveguide along the x- and y-coordinates, respectively. The axis orientation, waveguide dimensions, the electric field amplitude, and the location of the plasma channel are shown in Fig. 4.4. Figure 4.5 shows the filling factor as a function of the diameter of the plasma column, as defined in Eqn. 4.5, and Figure 4.6 shows the diffused diameter as a function of time for a pressure of argon of 50 Torr. To compensate the electron density profile of Fig. 4.3 for diffusion, the diameter of the diffusing

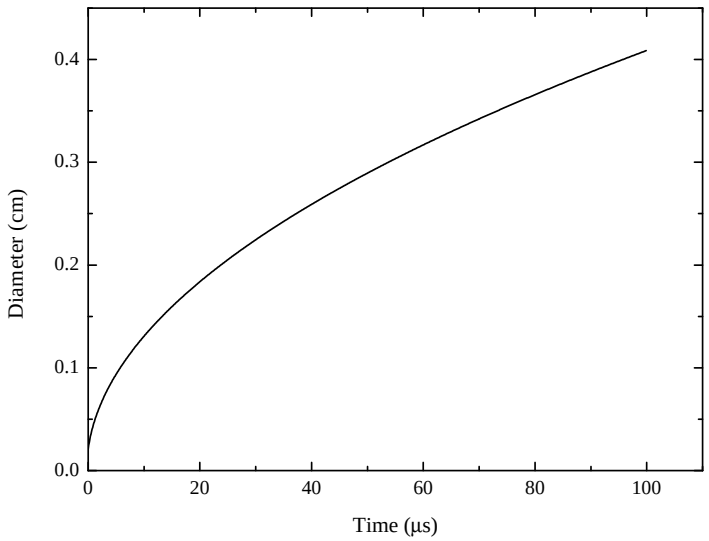

Figure 4.6: Diameter (σ) of the diffusing plasma channel as a function of time at P_{Ar}=50 Torr.

plasma cylinder is calculated as a function of time for a specific pressure, the filling factor is calculated as a function of time, and each point in the electron density is normalized to the filling factor at that time.

The second effect of diffusion is the loss of electrons to the walls of the waveguide. The data is not compensated for this effect, but is used to calculate electron loss terms for the models in Secs. 5.1.1 and 5.2.1. To determine the percentage of electrons lost to the walls as a function of time, the normalized spatial electron density distribution at a given time is integrated from 0.5 cm to infinity. This corresponds to the portion of the Gaussian profile that is at or beyond the interior wall of the waveguide. These electrons are considered lost. Figure 4.7 shows a representative calculation at a pressure of argon of 50 Torr.

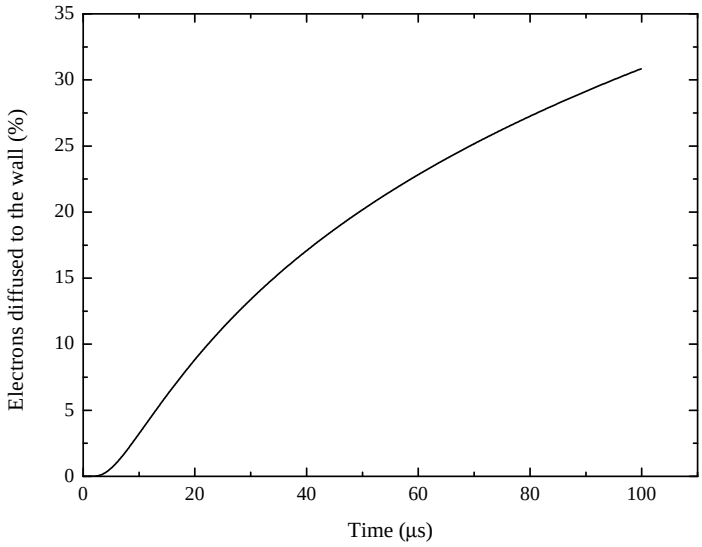

Figure 4.7: Percentage of electrons lost to the walls of the waveguide at 50 Torr.

Chapter 5

Representative Data and Discussion

5.1 Electron Decay Processes in Argon and Determination of Critical Constants

As a test of the microwave interferometry technique, a gas kinetic model was developed for argon. Argon was chosen for initial study because the noble gases have been studied most extensively with regard to the kinetics. In addition, argon is used for many applications, including inert gas welding, packing of high-purity or reactive chemicals, filling incandescent light bulbs to prevent oxidation of the filament, and as thermal insulation in energy efficient windows. These factors make it an ideal choice, both as a means to evaluate the experimental method but also determine rate constants that remain unknown or poorly characterized.

Data was acquired for pressures ranging from 1 Torr to 650 Torr, a range of almost three orders of magnitude. Between 50 and 650 Torr data were acquired in increments of 50 Torr, between 10 and 50 Torr, data were acquired in increments of 10 Torr, and additional data were acquired at 5, 2.5, and 1 Torr. For each pressure value, electron density profiles were recorded for 20 laser shots. The electron density was calculated using the method described in Sec. 4.3 for each shot separately and the final electron density curves were averaged point-by-point, and the standard deviation calculated. Figure 5.1 shows data at 250 Torr, averaged over 20 shots, with profiles representing plus and minus the standard deviation. This data has not been corrected for the $\sin\delta$ discontinuity or diffusion. Figures 5.2 and 5.3 show data (corrected for diffusion) for the entire pressure range measured. The decays

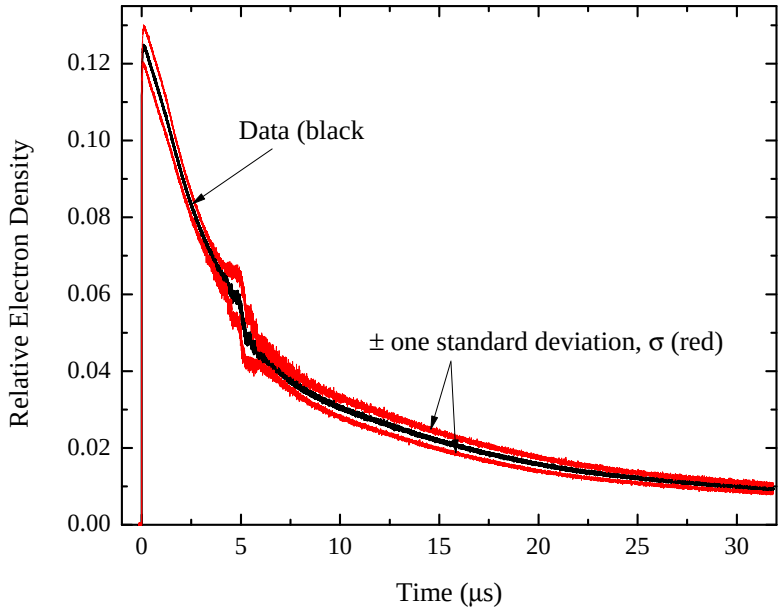

Figure 5.1: Electron density decay at 250 Torr, averaged over 20 shots, showing plus and minues one standard deviation.

are shown on a semi-log scale, on which a straight line would indicate a simple exponential decay. In Fig. 5.2, the electron density clearly decays according to a single exponential, while in Fig. 5.3, the decays are clearly more complex. A gas kinetic model was employed to examine these results.

5.1.1 Gas Kinetic Model for Argon

A graphical representation of the kinetic model developed for the analysis of the data is shown in Fig. 5.4. The states included in the model are the ground state of the argon atom, both atomic and molecular ions, a composite atomic excited state, and two molecular excited states. For the laser used in these experiments, λ=248 nm, so $\hbar\omega$=5 eV. The first ionization energy of argon is 15.76 eV, so four photons are required to produce atomic ions. The first excited states of argon, 4s (E = 11.6 eV) are populated by three-photon excitation. These are the two laser excitation processes considered by the model, and the initial population in

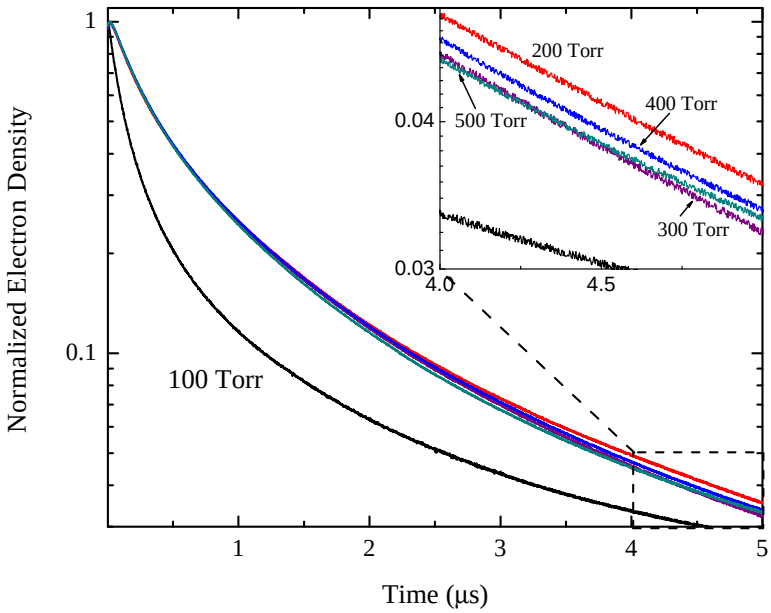

Figure 5.2: Normalized electron density decay for 100-500 Torr of argon.

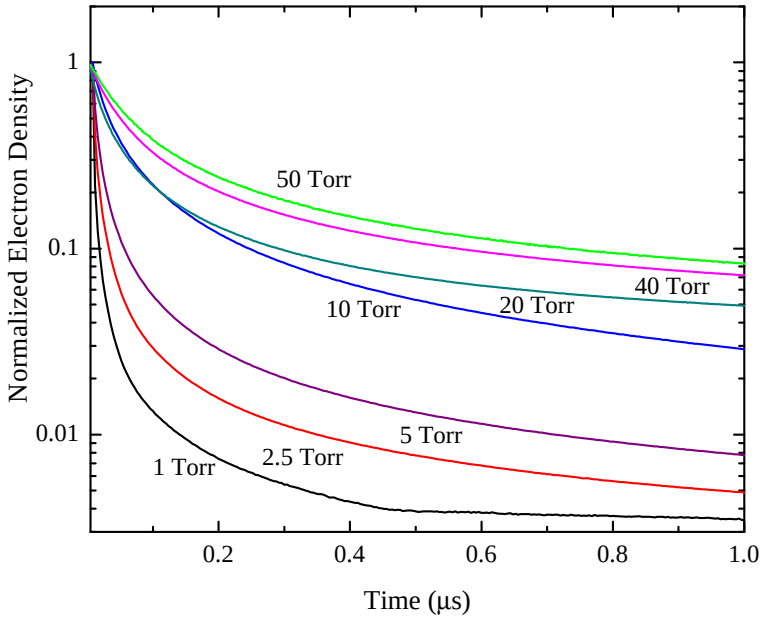

Figure 5.3: Normalized electron density decay for 1-50 Torr of argon.

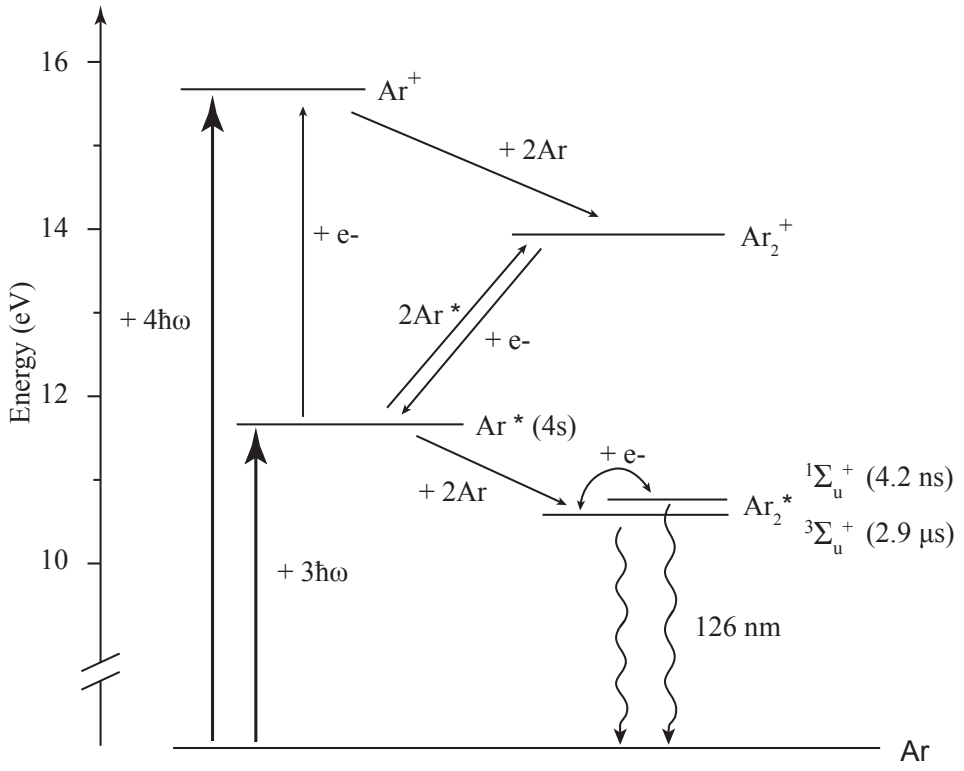

Figure 5.4: Diagram showing the processes in the kinetic model used in this work. Note the different lifetimes for the two $Ar_2^\star$ excimer states. (Diagram presumes a photon energy of $\hbar\omega$=5 eV.)

all of the molecular states is assumed to be zero. The two molecular excited states, singlet and triplet Σ_u^+, are of interest as excimer laser levels, with emission at 126 nm. The model here was adapted from Ref. [11], which was specifically concerned with the formation of these excimer states. As will be made apparent by the sensitivity analysis, the interactions involving these states are not critical to the decay of the electron density. A list of the reactions included in the model is shown in Table 5.1.

Two reactions, (4) and (5), produce additional electrons after the laser pulse has exited the plasma channel. Reaction (4) is electron impact ionization. Following as a result of four photon ionization of the atom, electrons are generated with a kinetic energy of over >4 eV. The lowest excited state of the atom is 11.6 eV, so higher lying atomic states have

Table 5.1: Argon reactions, rate constants, and references used in the kinetic model. T_e is the electron temperature in eV. The number in the left-hand column is used in the text to reference specific equations.

Equation	Reaction	Rate constant (Initial value)	References
(1)	$Ar + 4\hbar\omega \rightarrow Ar^+ + e^-$	1×10^{-116} cm^8 s^{-3}	[33, 34]
(2)	$Ar^+ + 2Ar \rightarrow Ar_2^+ + Ar$	2.5×10^{-31} cm^6 s^{-1}	[10]
(3)	$Ar_2^+ + e^- + \rightarrow Ar^\star + Ar$	$2 \times 10^{-7}\, T_e^{-0.67}$ cm^3 s^{-1}	[35]
(4)	$Ar^\star + e^- \rightarrow Ar^+ + 2e^-$	$1 \times 10^{-6} e^{-4/T_e}$ cm^3 s^{-1}	[36]
(5)	$2Ar^\star \rightarrow Ar_2^+ + e^-$	5×10^{-10} cm^3 s^{-1}	[10, 37–39]
(6)	$Ar^\star + 2Ar \rightarrow Ar_2^\star(^3\Sigma_u) + Ar$	1×10^{-32} cm^6 s^{-1}	[40]
(7)	$Ar^\star + 2Ar \rightarrow Ar_2^\star(^1\Sigma_u) + Ar$	3×10^{-34} cm^6 s^{-1}	[41, 42]
(8)	$Ar_2^\star(^3\Sigma_u) + e^- \rightarrow Ar_2^\star(^1\Sigma_u) + e^-$	5×10^{-8} cm^3 s^{-1}	[11]
(9)	$Ar_2^\star(^3\Sigma_u) \rightarrow h\nu + 2Ar$	3.5×10^5 s^{-1}	[42, 43]
(10)	$Ar_2^\star(^1\Sigma_u) \rightarrow h\nu + 2Ar$	2.4×10^8 s^{-1}	[41]

sufficient energy so as to be ionized in a collision with a 4 eV electron. Reaction (5), known as associative ionization, is a critical reaction, as it produces both additional electrons and molecular ions, which is the principle species with which electrons recombine. Two excited state atoms pool their energy to produce a molecular ion and an electron. Molecular ions are also produced by reaction (2), which rapidly converts atomic ions to molecular ions. The electron loss mechanism, dissociative ionization, is described by reaction (3). A molecular ion captures an electron, and subsequently dissociates into an excited state atom and a ground state atom. This reaction has been the subject of considerable interest over several decades, as discussed further in detail in Sec. 5.1.2. The dissociative recombination rate depends strongly on the electron temperature, because higher energy electrons will be less likely to be captured by the molecular ion.

Reactions (6)-(10) are molecular excited state (excimer) interactions. Production of these states occurs through a collision by reaction of two neutrals with an excited state atom. The branching ratio of excimer production between the singlet and triplet states has been measured to be about 30:1 in favor of the triplet state [41, 42]. As shown in Fig. 5.4 and

indicated in the rates for reactions (9) and (10), the triplet state has a much longer lifetime, so a spin transfer reaction to convert the triplet state to the singlet state is included (reaction (8)). The spontaneous spin flip rate is 10^{-13} [44], as compared to 10^{-8} when effected by an electron collision.

The reactions summarized in Table 5.1 were converted to a system of differential equations and solved using Mathematica. To determine which constants were the most significant in comparing the model and data, a sensitivity analysis was performed. Each constant was varied, individually, and the effect on the electron density temporal profile was observed.

A representative sample of sensitivity analyses is shown in Fig. 5.5. Note in panel (c) of the figure that the lower bound for the variation range is "-100%". This is equivalent to removing the excimer states from the model. Sensitivity analyses for the other reaction rates showed no significant effect on the electron density. The three rates that proved to be the most significant were the ionization cross section (reaction (1), Table 5.1), which dictates the initial electron density, the dissociative recombination rate (reaction (3)), which is the only electron loss mechanism in the model, and the electron cooling rate, which effectively controls the ionization by electron impact (reaction (4)), as well as influencing recombination.

The electron cooling rate is not included in the list of reactions, but must be included in the system of differential equations. The primary electron cooling mechanism was by momentum transfer collisions with atoms and molecules, and the momentum transfer cross section for electrons in argon has been studied extensively. At low electron energy (less than 10 eV) the cross section exhibits a complex structure known as the Ramsauer minimum [45], which is a result of interference between the free particle e^- wavefunctions. The cross section, illustrating this minimum, is shown in Fig. 5.6.

The model used here is not sufficiently complex to require such a detailed form of the cross section, and for these purposes the cross section was taken to be 10^{-16} cm^2. To determine the cooling rate, an analysis similar to that described in Sec. 4.4 was employed. The mean free path is calculated from the momentum transfer cross section, and the velocity is related

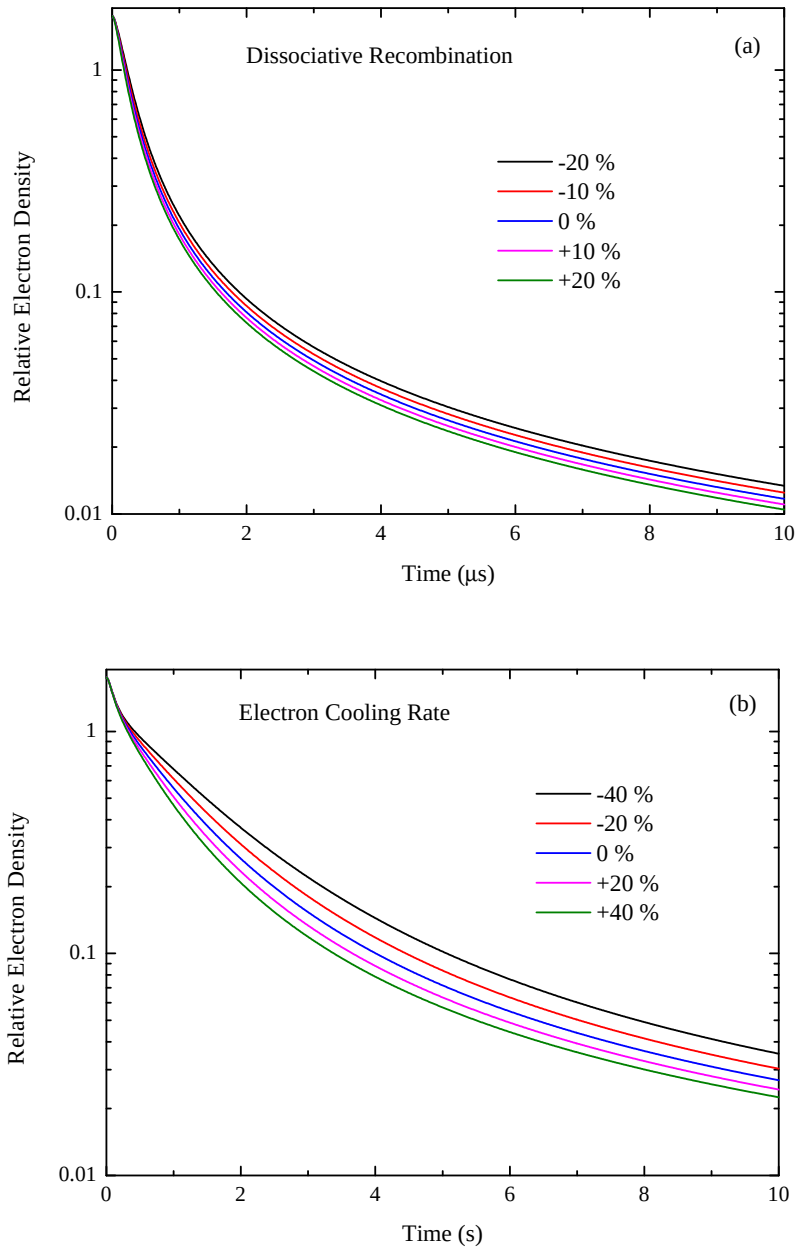

Figure 5.5: Sensitivity analysis of argon model. Note the different ranges for varying the constant, especially in (c), where the line for "-100%" shows the effect of completely removing the excimer states from the model.

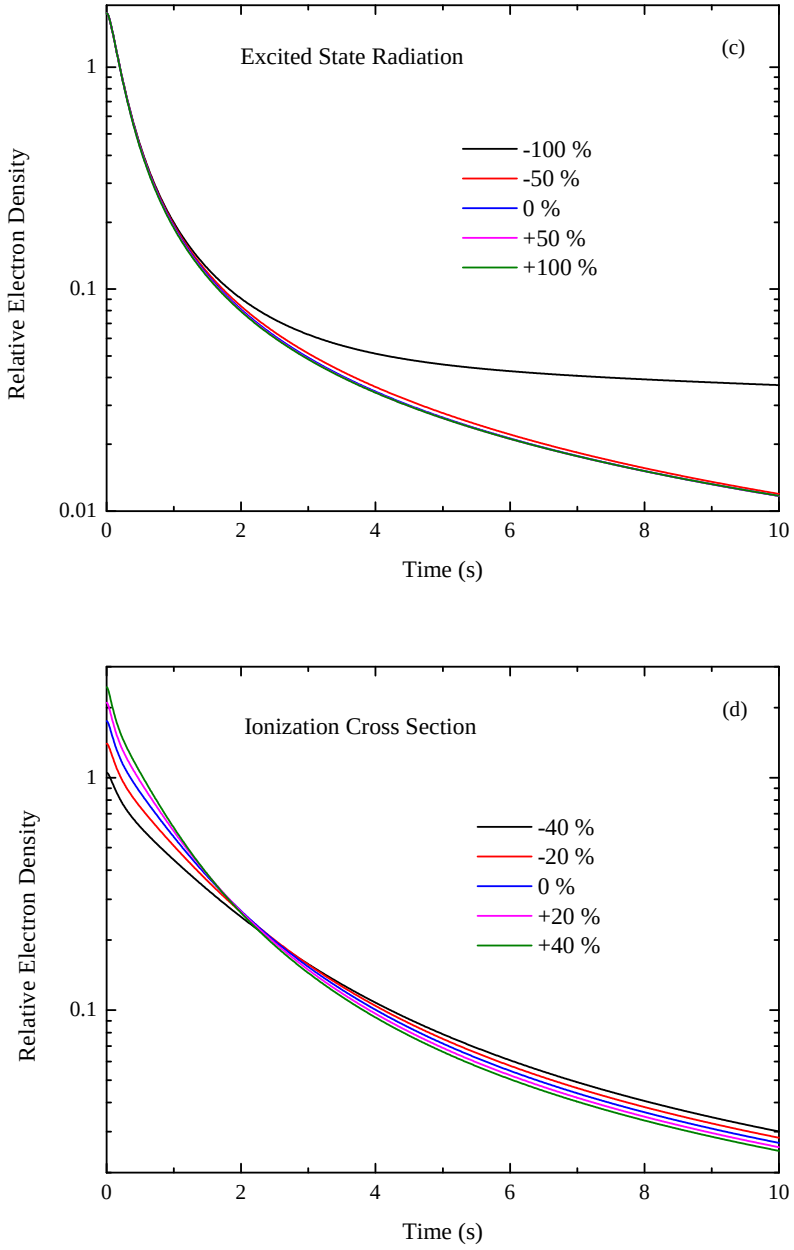

Figure 5.5: (continued)

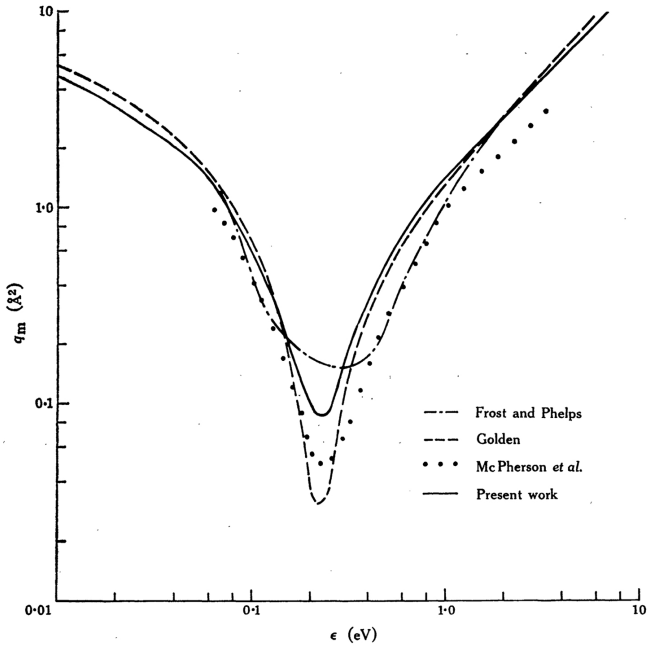

Figure 5.6: Reproduced from [45] "Present work". Comparison of results for the momentum transfer cross section $q_m(\varepsilon)$ for electron-argon scattering. References Frost and Phelps [46], Golden [47], and McPherson *et al.* [48].

to the electron temperature by the expression $\overline{v} = \sqrt{2E/m}$. The conservation of energy and momentum give an average energy loss per collision of 10^{-4} times the electron energy [3]. Because the collision rate is determined by the velocity and the electron-neutral mean free path, and the energy loss per collision is known, the total electron cooling rate is given by

$$\frac{d}{dt}T_e = -T_e^{3/2} \cdot 2 \times 10^{-7} \cdot n_e. \tag{5.1}$$

To fit the model to the data, a modified version of simulated annealing [49] (a type of genetic optimization algorithm) was used. With three constants to be adjusted, the parameter space is quite large. The rates are interconnected with regards to their effect on the electron density decay, and must be adjusted simulataneously. The constants were not varied randomly, as in true simulated annealing, but were first varied by ±40% in increments of 20%. The best fit was found by a weighted sum of residuals. The weighting was necessary because there are many more points in the tail of the decay, so the initial decay of the

Table 5.2: Constants used to fit model to data.

Pressure (Torr)	Cooling Rate ($\times 10^{-8}$cm^3 s^{-1})	Ionization cross section, σ_4 ($\times 10^{-118}$cm^8 s^{-3})	α_D ($\times 10^{-6}$ cm^3 s^{-1})
150	3.2	9.4	6.0
200	3.8	8.3	3.2
250	4.8	8.9	1.4
300	4.4	5.4	1.6
350	5.0	3.0	2.3
400	6.2	3.5	1.2
450	1.0	1.8	3.0
500	4.6	1.8	3.7
550	4.0	2.3	2.3
600	6.0	1.8	2.6

electron density profile must be weighted to fit both portions with equal significance. The model was adjusted using the constants for the minimum sum of residuals, and the process was repeated, varying the constants ±20% in increments of 10%. Finally, the constants were varied ±10% in increments of 5%. The optimized fit constants are those that produce the minimum sum of residuals for this final stage. Figure 5.7 shows an example of the optimized fit using this technique. To demonstrate the sensitivity of this technique, Fig. 5.8 shows two curves generated by the *maximum* sum of squares in the final stage of optimization. The curves shown are produced by constants which vary from the optimized value by at most 20%.

This optimization procedure was conducted for pressures from 150 to 600 Torr, and the constants derived are shown in Table 5.2. The cooling rate scaling factor shows a slight increase with increasing pressure, which is likely due to the fact that the calculation of the cooling rate assumed a constant value for the number density of Ar, while clearly at higher pressures the mean free path between collisions will be shorter, so the cooling rate will increase. The ionization cross-section shows a decrease with increasing pressure. This implies a nonlinear dependence on pressure for the ionization of the gas. The initial

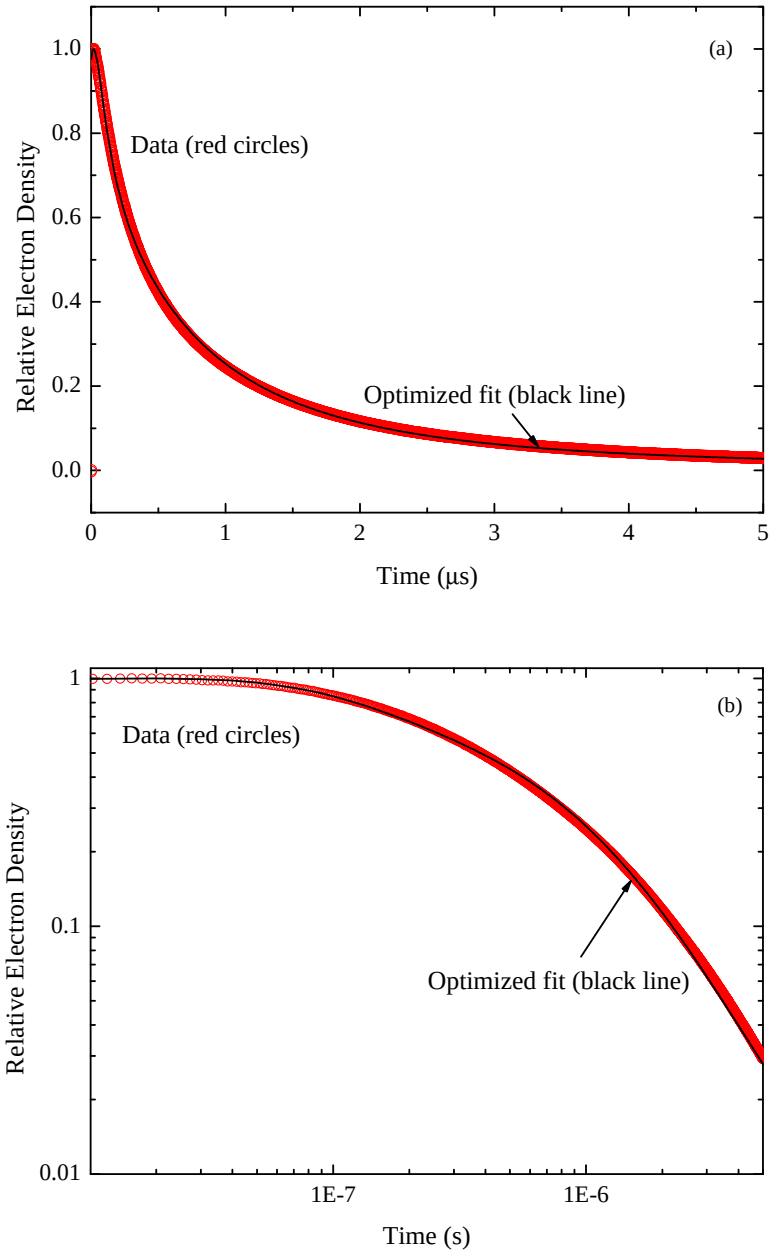

Figure 5.7: Sample fit data for 300 Torr. The (red) circles are the data and the black line is the calculated best fit from the model. The two graphs show the same data and fit, (a) on a linear scale and (b) on a log scale.

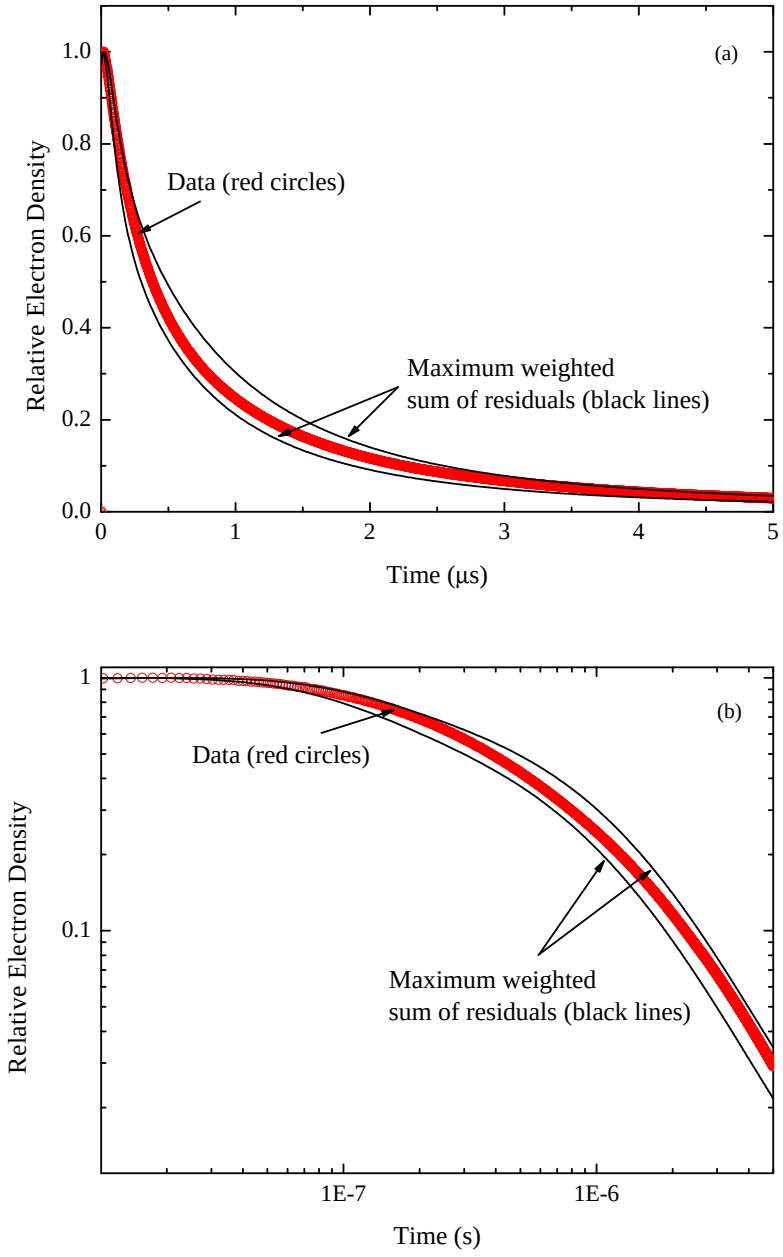

Figure 5.8: Sample fit data with two curves corresponding to the maximum sum of residuals from the final stage of optimization.

ion/electron density is calculated as

$$n_e = \Delta t \left(\frac{I}{\hbar\omega} \right)^4 [Ar]\, \sigma, \tag{5.2}$$

where Δt is the pulse duration, I is the laser intensity expressed in W/cm^2, ω is the laser frequency, $[Ar]$ is the neutral argon number density, and σ is the multiphoton ionization cross-section expressed in units of cm^8 s^3. Clearly, this should result in a linear dependence on pressure of the initial density. The likely explanation for this discrepancy is that the diffusion calculations, both to adjust the electron density measurements and to include diffusion in the model, were not sufficiently detailed. This is discussed further in Sec. 5.1.3. The values for the dissociative recombination rate are the subject of the next section.

5.1.2 Dissociative Recombination

Because the three-body ion association reaction

$$\mathrm{Ar}^+ + 2\mathrm{Ar} \rightarrow \mathrm{Ar}_2^+ + \mathrm{Ar} \tag{5.3}$$

rapidly converts atomic ions, Ar^+, into molecular ions, Ar_2^+, the electron recombination process relies primarily on the molecular ion. In fact, the only recombination process included in the present model is that for the molecular ion. This means the dissociative recombination process is critically important for determining the decay behavior of an argon plasma. Table 5.3 summarizes previous measurements of α_D, specifying the pressure, temperature, and production and analysis techniques. It is significant to note that the most recent measurement is from 1993. Additionally, the most frequently cited work is that of Shin and Biondi in 1978 [50]. More recent studies of dissociative recombination have focused on the decay products and not on measuring the rate constant itself.

The first measurement of electron-ion recombination in any gas was made in 1928 in

Table 5.3: Previous measurements of the dissociative recombination rate in argon. Adapted and expanded from [35].

Reference (Year)	α_D (cm^3 s^{-1})	Pressure (Torr)	Temperature (K)	Production Technique	Analysis Technique
[51] (1928)	2×10^{-10}	<30		Arc discharge	Optical spectroscopy
[52] (1949)	3×10^{-7}	15-30	300	Microwave	Microwave cavity
[53] (1951)	8.8×10^{-7}	14	300	Ionization by Ne metastable	Microwave cavity
[54] (1951)	1.1×10^{-6}	20-30		Microwave	Microwave and Optical spectroscopy[a]
[55] (1958)	$4 - 9 \times 10^{-7}$	5-50		Microwave	Microwave cavity[b]
[56] (1960)	2×10^{-7}	18.3		Microwave	Microwave cavity
[57] (1963)	$10^{-7} < \alpha < 10^{-6}$	1.9-7.1		Microwave	Microwave cavity
[58] (1963)	$(6.7 \pm 0.5) \times 10^{-7}$	9-35		Microwave	Microwave cavity[c]
[59] (1966)	$5 \times 10^{-7} T_e^{-1.3}$	3	1000-3000	Shock tube	Langmuir probe[d]
[60] (1968)	$8.5 \times 10^{-7} T_e^{-0.67}$	5-20	300-10000	Microwave	Microwave cavity
[50] (1978)	$9.1 \times 10^{-7} T_e^{-0.61}$	5-15	300-8500	Microwave	Microwave and Optical spectroscopy
[61] (1969)	$6 - 10 \times 10^{-7}$	flow	T_g=400-900	Discharge tube	Microwave and Mass spectrometry
[62] (1983)	2×10^{-7}	200-12000		Electron beam	Optical spectroscopy[e]
[35] (1992)	$1.07 - 1.55 \times 10^{-6}$	150-1065	295-375	Electron beam	Microwave attenuation[e]
[63] (1993)	$(8.2 \pm 0.5) \times 10^{-7}$	5	300	Discharge tube	Microwave cavity
[64] (2006)	$5 - 20 \times 10^{-7}$		100-1100		Calculation[f]
Present work	$1 - 6 \times 10^{-6}$	150-600		Laser-induced breakdown	Microwave Interferometry

[a] No α_D values derived from optical work
[b] Anomalous pressure dependence
[c] Acknowledged electron loss by diffusion
[d] First temperature dependence study
[e] Resolved two- and three-body processes
[f] Calculated temperature dependence $T_e^{-0.67}$, $T_e < 800$K, $T_e^{-1.5}$, $T_e > 800$K

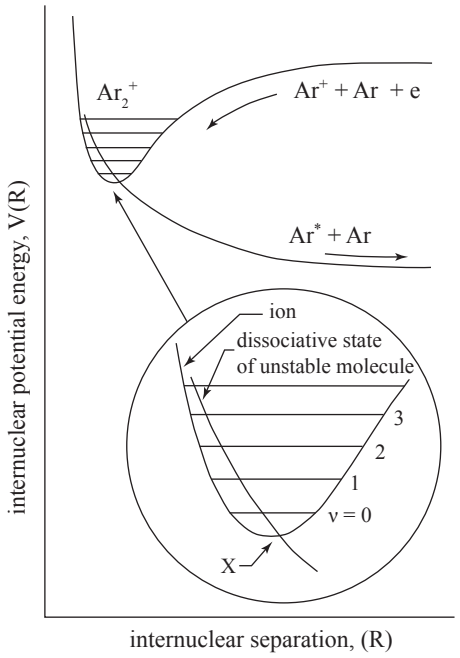

Figure 5.9: Schematic representation of the mechanism of dissociative recombination. $X_2^+ + e \rightarrow (X_2^\star)_{dissoc.} \rightarrow X^\star + X + \text{kinetic energy}$ Adapted from [57].

argon by Kenty [51], but the experiment was rather crude and did not account for any other loss mechanisms for the electrons. The earliest modern measurements were made by Biondi and Brown [52], using the microwave probing techniques that, at the time, were pioneering. Most of the early experiments involved gas samples of questionable purity, implying that the measured rates might actually be a result of the impurities, the most likely of which was nitrogen. In 1963, Biondi summarized the results to date and analyzing the process of dissociative recombination [57]. Theoretical calculations for atomic ion-electron capture, $X^+ + e \rightarrow X^\star + h\nu$, had estimated values in the range 10^{-11} - 10^{-12} cm^3 s^{-1} [65] much less than the measured values. The process of dissociative recombination was suggested to explain the large values observed in experiments. The schematic representation of the process is shown in Fig. 5.9. At low partial pressures of argon, usually with a helium buffer gas, the dominant ion is the atomic ion, and the recombination rates are in line with the theoretical predictions.

Dissociative recombination involves electron capture and, thus, the rate constant will

depend strongly on temperature. High energy electrons will be less likely to be captured by the molecular ion. The first temperature dependence study was reported in 1966 by Fox and Hobson [59] who generated high temperature plasmas in a shock tube. However, shock heating also heats the gas (not simply the electrons), which could result in a reduced value for α_D owing to the less favorable overlap between vibrationally excited Ar_2^+ molecules and the repulsive $Ar_2^\star$ states. In 1968, Mehr and Biondi [60] heated the electrons with a microwave source, measuring the now-accepted temperature dependence of $T_e^{-0.67}$. This along with the 1978 work by Shui and Biondi [50], is regarded as the seminal work on the dissociative recombination rate constant. In recent papers examining the decay products of the recombination, as well as papers modeling argon plasmas, these are the values used for the rate constant.

Since 1978, there have only been two additional measurements, Kuo and Keto [62] in 1983 and Cooper *et al.* [35] in 1992. Both measurements ionized high pressure ($>$ 100 Torr) gas samples with an electron beam. Kuo and Keto used optical emission spectroscopy to measure the decay of radiation from the $Ar(3p^5 4p)$, which, on the basis of Ref. [50] is expected to be the product of the recombination of the dimer ion. Cooper *et al.* measured the electron decay directly with a more conventional a.c. microwave conductivity technique. These two results are discussed in more detail later. One additional relevant reference is the theoretical paper of Royal and Orel [64], which reported calculated dissociative recombination cross sections and rate constants for a range of pressure and temperature dependence. The results were consistent with experimental measurements, and reproduced the temperature dependence of $T_e^{-0.67}$.

With the exception of the work of Kuo and Keto [62] and Cooper *et al.* [35], previous measurements of α_D were made at low pressure, that is, $<$ 50 Torr, which appears to be attributable to the difficulty of producing a plasma in argon at high pressure. Both high pressure measurements used an electron beam source to produce the plasma. The pressure range explored by the present work was similar to those, so Fig. 5.10 shows data from

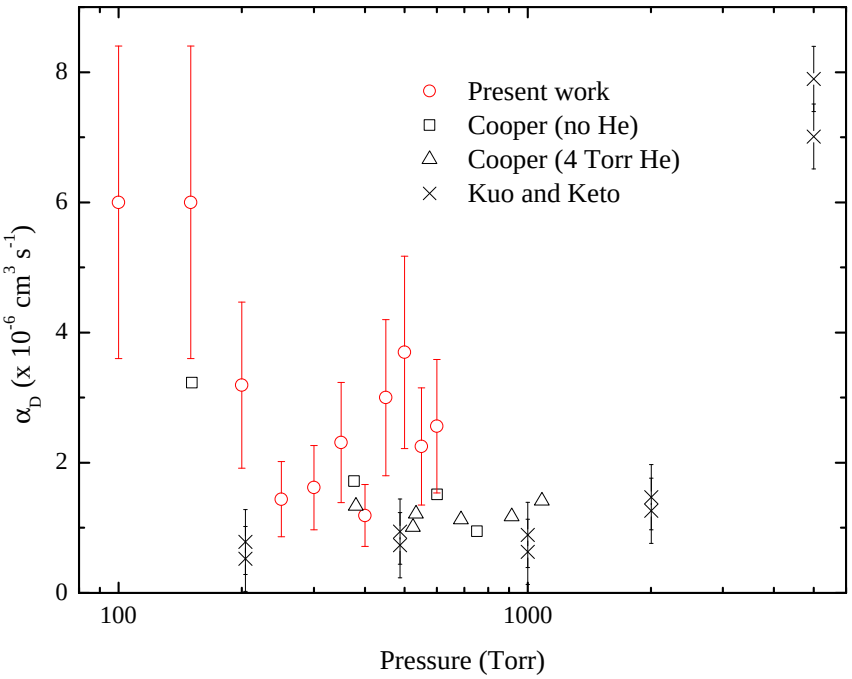

Figure 5.10: Pressure dependence of α_D. Data from Cooper *et al.* [35] (black squares and triangles, see helium explanation in text), Kuo and Keto [62] (black crosses), and present work (red circles).

Refs. [62] and [35] with the present work. The two sets of points from Cooper *et al.* [35] show data both with and without an addition of 4 Torr of helium to effect rapid electron thermalization. No error bars were reported by Cooper *et al.*. The monotonic decrease of the ionization cross-section, shown in Table 5.2, indicates the likelihood of some systematic error in the model, as discussed in Sec. 5.1.1. In addition, the present work determination of α_D displays oscillatory behavior between 300 and 600 Torr which is not reproduceable by a physical model. The uncertainty in the model fit determination of α_D has several sources, including that introduced by the averaging of 20 electron density decay profiles (shown in Fig. 5.1), as well as the acknowledged uncertainty in the diffusion analysis. A comprehensive error propagation analysis was not performed, but it is clear from the data that the uncertainty must be at least large enough to neutralize the oscillatory behavior. The error bars shown in Figs. 5.10 and 5.11 represent $\pm 40\%$ of the value of α_D.

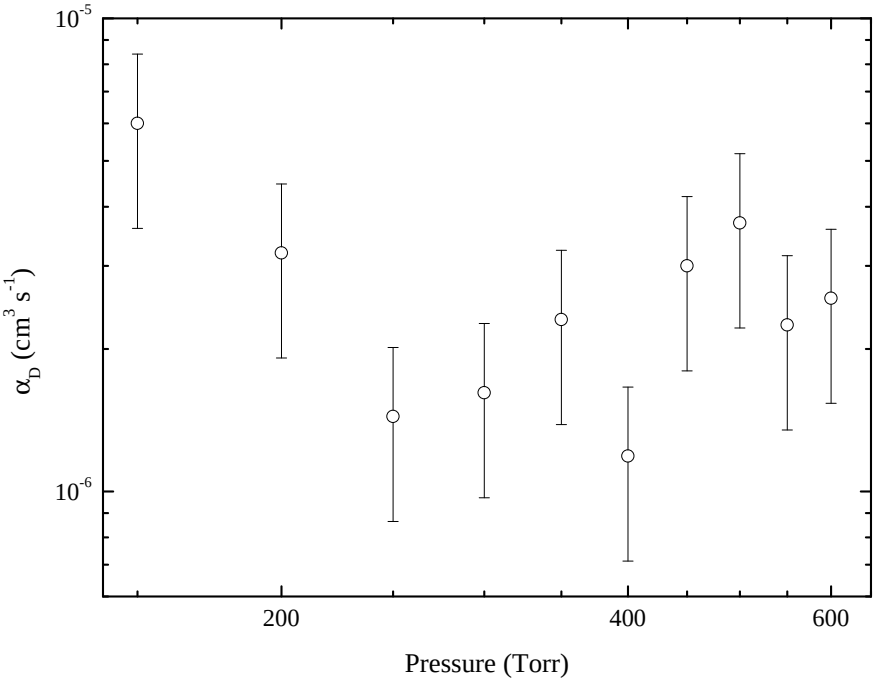

Figure 5.11: Pressure dependence of α_D showing only the present work.

To highlight some features of the present work, Fig. 5.11 shows the pressure dependence of α_D from only the present work, for clarity. The trend for the rate constant shows a minimum at about 350 Torr. Above this point, α_D increases with increasing pressure. This is attributed to the introduction of three-body recombination processes, which have a negligible rate at lower pressures. The work of Kuo and Keto [62], as shown in Fig. 5.10, demonstrates this trend, although the minimum occurs at a higher pressure, above 1000 Torr. Their data show a monotonically increasing decay rate, however, and the lowest pressure shown is 200 Torr, possibly obscuring a minimum at lower pressure. The focus of their experiment was the high pressure value, so there are only four points (the pairs of points at each pressure in Fig. 5.10 are at two different initial electron densities) between 200-1100 Torr, and the data as presented in the paper is not accurate enough to discern a trend in that pressure range. This is a strength of the present work, that it spans pressure range that bridges the older, lower pressure studies and the modern electron beam high pressure studies. The data from Cooper *et al.* is in the range 400-1100 Torr, and has a slight curvature with a minimum

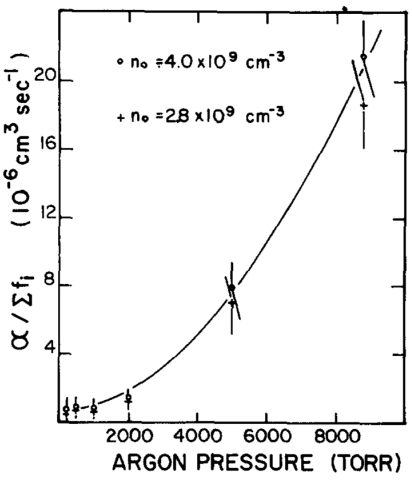

FIG. 6. The rate $\alpha/\sum f_i$, obtained from the decay of the $Ar(3p^5 4p)$ configuration, plotted as a function of argon pressure.

Figure 5.12: Data from Kuo and Keto [62] with original caption. Reprinted with permission from [62]. Copyright 1983, American Institute of Physics.

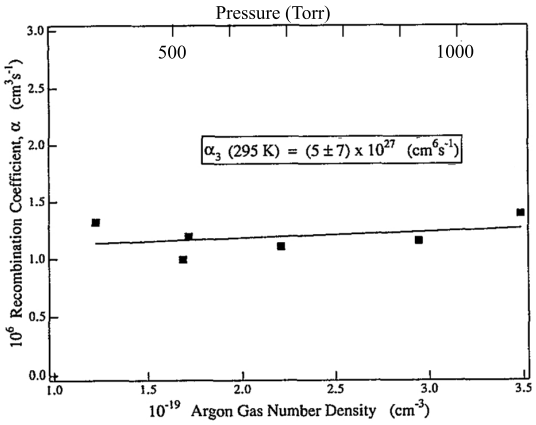

FIG. 6. The pressure variation of the ion-electron recombination rate constant α in pulse irradiated argon at 295 K. Bulk gas pressures are expressed as gas number densities. Within the experimental uncertainty, no pressure dependence for α is observed.

Figure 5.13: Data from Cooper *et al.* [35] with original caption, Pressure (Torr) axis added for clarity. Reprinted with permission from [35]. Copyright 1993, American Institute of Physics.

at approximately 600-700 Torr, but Ref. [35] claims that within the limits of experimental uncertainty (which are not explicitly stated, nor are any error bars shown) there is no pressure dependence. For reference, the original figures from these two references are shown in Figs. 5.12 and 5.13, with the original captions.

There is a marked pressure gap in the previous measurements of the dissociative recombination rate constant, between the low pressure studies (1-50 Torr) and the atmospheric pressure studies (200+ Torr). The current work bridges this gap with results that are consistent with the previous work, and offer new insight into the 200-400 Torr pressure range, where previous data is thin. The turning point for three-body reactions is observed in the present work at ≈350 Torr, lower than the one previous measurement (Kuo and Keto [62]), but determined from more complete data. In addition to providing data for the recombination rate constant in this unique pressure range, the present work also demonstrates the successful use of a new production and measurement technique combination and verifies the results with a gas kinetic model.

5.1.3 Multiphoton Ionization Cross Section

Multiphoton ionization (MPI) occurs when two or more photons, whose combined energy is greater than the ionization threshold, are simultaneously absorbed by an atom or molecule. The intensity required for non-neglible ionization rates for N-photon ionization increases with increasing N. The ionization rate varies as $\sigma_N I^N$, of which Eqn. 5.2 is a specific example, σ_N is a generalized ionization cross section with units of $\mathrm{cm}^{2N}\ \mathrm{s}^{N-1}$, and I is the laser intensity [66]. Because the intensities required for multiphoton ionization are $> 10^{10}$ W cm^{-2}, studies were limited to those wavelengths for which high-energy lasers were available. Commonly used wavelength ranges are 1047-1064 nm, 524-532 nm (Nd:YLF, Nd:glass, and Nd:YAG and second harmonics), 800 nm and 400 nm (Ti:sapphire and second harmonic).

For argon irradiated by 248 nm photons, only one experimental study has been done [33]. A hybrid dye-excimer laser system [67] produced ≈500-fs pulses with a maximum pulse energy of 14 mJ. The system is similar to the one described in Sec. 3.1, with a dye laser seed replacing the frequency tripled Ti:sapphire seed. Above threshold ionization (ATI) electron energy spectra were measured for the noble gases He, Ne, Ar, and Kr with a time-of-flight spectrometer. Above threshold ionization is an extension of MPI in which the number of photons absorbed by the electron is greater than the number required to escape the atomic binding energy. The resulting electron energy spectra show a series of ATI peaks separated by the photon energy of the incident radiation. An example of this is shown in Fig. 5.14 for xenon irradiated by an Nd:YAG (λ = 1064 nm, $\hbar\omega$ = 1.165 eV) laser. It was previously observed that the amplitudes, widths and positions of the peaks in the ATI photoionization spectra were dependent on the laser pulse energy and pulse duration (see Ref. [69] and references therein). Uiterwaal *et al.* [33] extracted generalized cross sections from observations of this shift in the rare gases. Their results are summarized in Table 5.4.

After the first ATI experiments, it was clear that the previous theories, which relied on treating the laser-field as a pertubation of the atomic Hamiltonian, were no longer sufficient

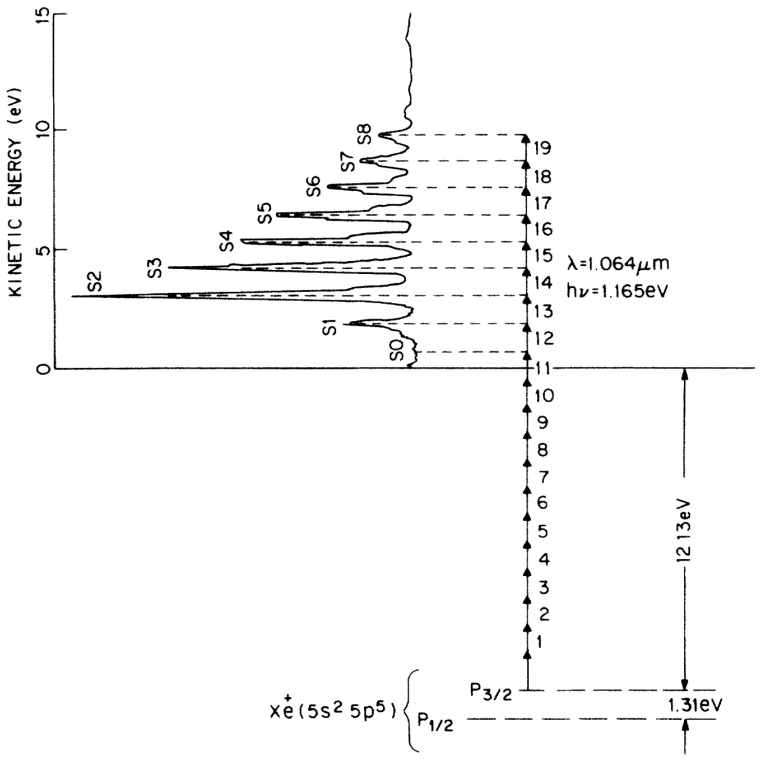

Figure 5.14: ATI spectrum for xenon irradiated by 1064-nm light. The small arrows indicate the number of photons absorbed, and the peaks are labeled SN, where N is the number of photons absorbed above threshold. Reproduced figure with permission from [68]. Copyright 1986 by the American Physical Society.

Table 5.4: Adapted from [33]. Experimental values for the generalized MPI cross sections $\sigma_{(N)}$ for the noble gases extracted from the shift in ATI electron energy spectra with increasing laser pulse energy. It was determined that the behavior of neon was not consistent with the model, so the cross section could not be determined.

Gas	Ionization threshold (eV)	Number of photons (N)	Cross section
Helium	24.6	5	$(0.9^{-0.4}_{+9}) \times 10^{-152}$ cm^{10} s^{4}
Neon	21.6	5	see caption
Argon	15.8	4	$(1.3^{-0.5}_{+1}) \times 10^{-116}$ cm^{8} s^{3}
Krypton	14.0	3	$(1.2^{-0.6}_{+1.7}) \times 10^{-82}$ cm^{6} s^{2}
Xenon	12.1	3	$(50^{-45}_{+350}) \times 10^{-82}$ cm^{6} s^{2}

to describe experimental results. Non-perturbative theories were then considered and developed. In 2006, van der Hart [70] obtained a four-photon ionization cross section for argon of $\sigma^{(4)} = 1.9 \times 10^{-115}$ cm^{8} s^{3}. The order of magnitude difference between this result and

the the work of Uiterwaal *et al.* was attributed to the different laser intensities at which the experiments and calculations were performed (see also Refs. 19-21 in [70]).

The MPI cross sections predicted by the model in the present work are in the range $10^{-117} - 10^{-118}$ cm^8 s^3, an order of magnitude lower than the values obtained by Uiterwaal *et al.*, and two orders of magnitude lower than the calculated values. This is likely a result of the way the cross section is obtained from the model. What is optimized in the model is the initial ion and electron density, from which the cross section is determined by estimating the laser pulse energy, pulse width, and the focal spot size. Due to the jitter in the excimer thyratrons (see Sec. 3.1), the shot to shot variation in the pulse energy can be as high as 20%. The pulse width, likewise, is not well characterized, given the absence of techniques to determine fs pulse widths in the UV. The focal spot size is estimated from visible emission from the laser channel. Because the four-photon ionization rate scales as the fourth power of the laser intensity, uncertainty in the laser pulse energy and width has a large impact on the value of the cross section. A error of 20% in the estimation of the laser intensity would change the prediction for the cross section by a factor of 2.5. Consequently, the predictions of the present work for the MPI cross section must be considered estimates of order of magnitude only. With improvements in the measurement of pulse characteristics, it would be possible to predict the cross section more accurately using the present experimental method.

5.2 Electron Decay Processes in Nitrogen and Determination of Critical Constants

Following the completion of the experiments and analysis of the argon data, a second gas kinetic model was developed for electron density decay in nitrogen. As the most abundant gas species in Earth's atmosphere (78% by volume), nitrogen is a uniquely important gas molecule. The molecular triple bond has a bond energy of 9.8 eV, making N_2 almost as chemically inactive as the noble gases. It is often used as a less expensive alternative to argon (for argon applications see the introduction to Sec. 5.1). This utility and abundance, as well as the unique properties of the triple bond make nitrogen one of the most studied gases in plasma physics. The kinetic model described here is adapted from several more complex models discussed in Refs. [9, 71, 72].

Data were collected and analyzed in the same manner as that described for argon, with 20 laser shots per pressure measurement, and the pressure range investigated was again 1-650 Torr. Figures 5.15 and 5.16 show electron density decays for pressures ranging from 1 to 500 Torr. Note that the ordinate of both figures is logarithmic. Also similarly to argon, the decay of the electron density exhibits a multi-exponential decay.

5.2.1 Gas Kinetic Model

Nitrogen plasmas are the subject of several complex models, some of them in combination with oxygen, which may include literally hundreds of reactions [9, 71, 72]. The model developed for the present work includes the minimal set of reations required to capture the essential physics. The ground state of the nitrogen molecule is denoted $N_2(X)$, and corresponds to the $X^1\Sigma_g^+$ state. The excited states denoted $N_2(A)$ and $N_2(B)$ correspond to the $A^3\Sigma_u^+$ and $B^3\Pi_g$ states, respectively. The $N_2(B)$ is a composite second excited state that includes the states $C^3\Pi_u$ and $a'^1\Sigma_u^-$. Spectroscopic studies and previous models have indicated that these are the excited molecular states of interest. There are two atomic states

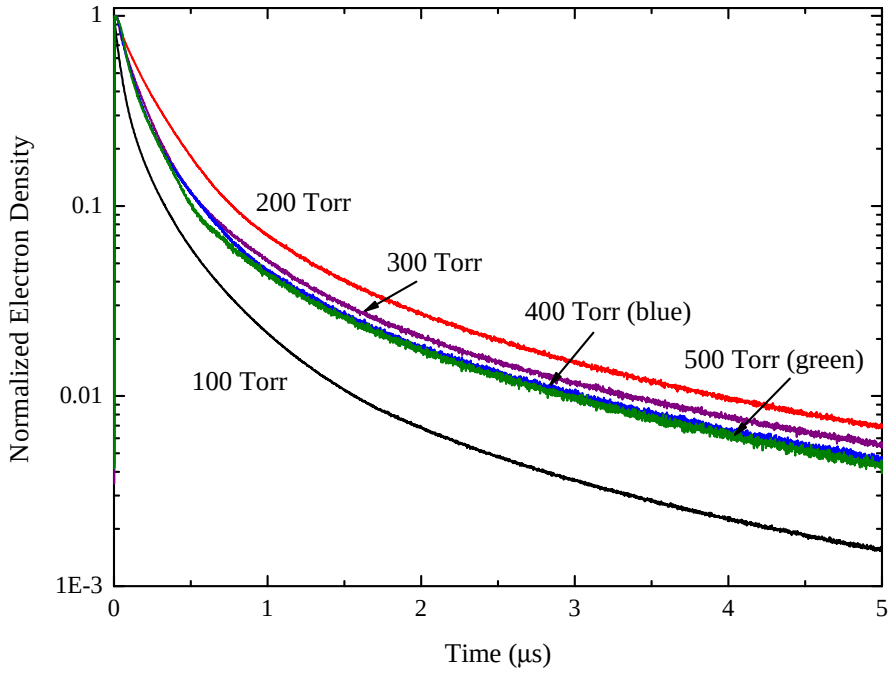

Figure 5.15: Normalized electron density decay for 100-500 Torr of nitrogen.

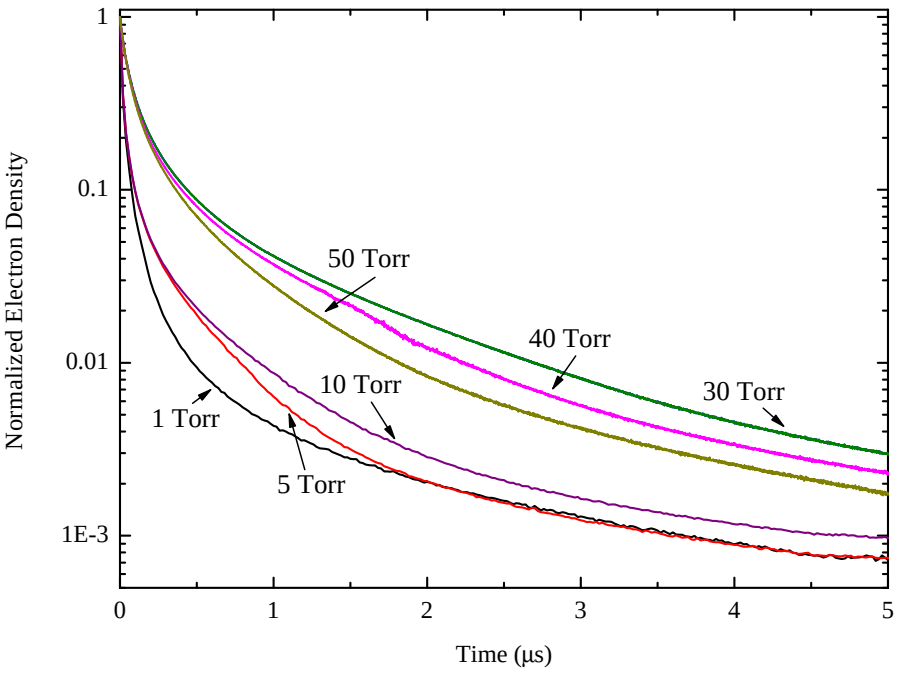

Figure 5.16: Normalized electron density decay for 1-50 Torr of nitrogen.

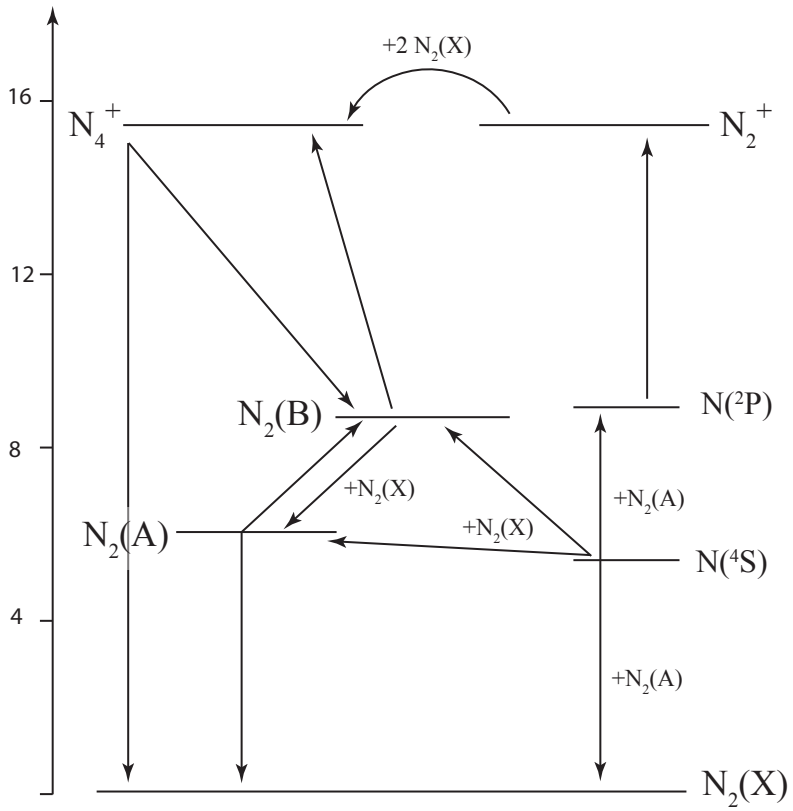

Figure 5.17: Diagram of the processes included in the gas kinetic model. The energy of the atomic ground state is given as 5 eV above the molecular ground state, as the binding energy of N_2 is ≈10 eV. The ionization threshold is 15.5 eV.

included in the model, the ground state, $N(^4S)$ and the second excited state, $N(^2P)$, and two ionic species, N_2^+ and N_4^+. A diagram of the model used is shown in Fig. 5.17.

A list of reactions included is shown in Table 5.5. Reactions (1)-(4) involve only neutral atoms and molecules. The sensitivity analysis demonstrated that these reactions were not critically important to the electron density decay. Reactions (5)-(7) describe ionization and ion reactions. Note the much smaller values for the rates of associative ionization ($10^{-12} - 10^{-11}$ cm^3 s^{-1}) as compared to that of argon (10^{-10} cm^3 s^{-1}). The only ion reaction with significant impact on the electron density is reaction (7), the three-body ion association reaction. As in argon, this reaction rapidly converts the N_2^+ ions produced by multi-photon ionization into the N_4^+ ions. Also similarly to argon, the recombination reaction is dissocia-

Table 5.5: Nitrogen reactions and rate constants used in the kinetic model. tT_e is the electron temperature in eV. All constants are from Refs. [9, 71].

Equation	Reaction	Rate Constant
Reactions involving only neutrals:		
(1)	$2N_2(A) \rightarrow N_2(X) + N_2(B)$	3×10^{-10} cm^3 s^{-1}
(2)	$N_2(B) + N_2(X) \rightarrow N_2(A) + N_2(X)$	$(1-5) \times 10^{-11}$ cm^3 s^{-1}
(3)	$N_2(A) + N(^4S) \rightarrow N_2(X) + N(^2P)$	5×10^{-10} cm^3 s^{-1}
(4)	$2N(^4S) + N_2(X) \rightarrow N_2(X) + N_2(A)$	$8.3 \times 10^{-34} \exp(0.61/T_e)$ cm^6 s^{-1}
	$2N(^4S) + N_2(X) \rightarrow N_2(X) + N_2(B)$	$8.3 \times 10^{-34} \exp(0.61/T_e)$ cm^6 s^{-1}
Ionization and ion reactions:		
(5)	$2N(^2P) \rightarrow N_2^+ + e^-$	10^{-12} cm^3 s^{-1}
(6)	$2N_2(B) \rightarrow N_4^+ + e^-$	5×10^{-11} cm^3 s^{-1}
(7)	$N_2^+ + 2N_2(X) \rightarrow N_4^+ + N_2(X)$	$5 \times 10^{-29} \left(\frac{0.39}{T_e}\right)^{1.64}$ cm^6 s^{-1}
Recombination:		
(8)	$N_4^+ + e^- \rightarrow N_2(X) + N_2(B)$	$2 \times 10^{-6} \left(\frac{0.39}{T_e}\right)^{\frac{1}{2}}$ cm^3 s^{-1}

tive, involving only the tetratomic ion (reaction (8)). A sensitivity analysis was performed, and the results are shown in Fig. 5.18. The model fitting procedure was identical to that used for argon (outlined in Sec. 5.1.1).

At pressures above 100 Torr, the model was only partially successful. The model predictions did not converge reliably because the data showed a slight increase in electron density immediately following the laser pulse, which was not reproduced by the model. This was not a problem in argon, with its larger associative ionization rate constants, but in nitrogen the associative ionization was insufficient to produce additional electron ionization. Also, electron impact ionization (reaction (3) in Table 5.1 for argon) was not included in the model. Electron impact ionization could be possible from higher lying excited states than those included in the model, such as the $^1\Sigma_u^+$ and $^1\Pi_u$ levels. The results shown in Figs. 5.19 and 5.20 show the data and fit for 300 Torr of nitrogen, where the first 300 ns interval is expanded to show the increase in electron density. The results for 200-500 Torr were similar. The value of α_D used for this fit was 1×10^{-6} cm^3 s^{-1}, but the fit was not conclusive.

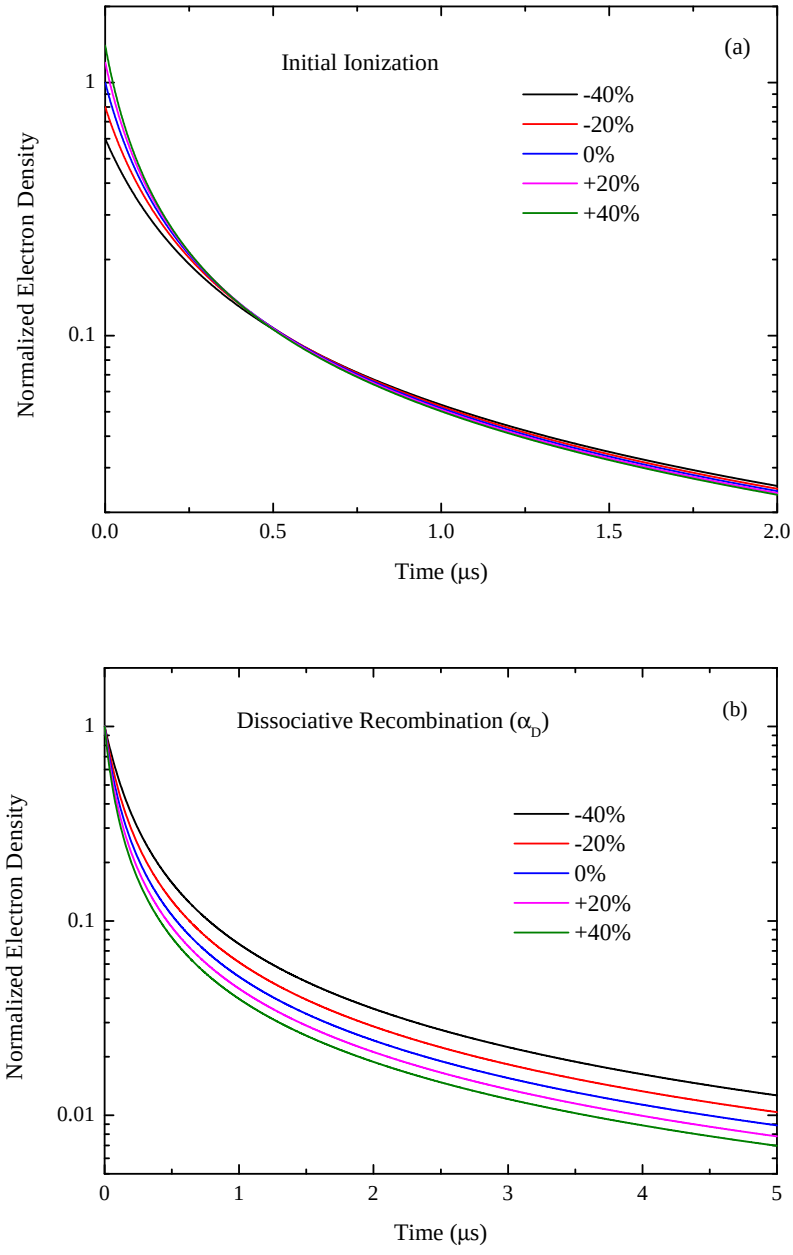

Figure 5.18: Sensitivity analysis of nitrogen model. All of the variation percentages are the same, but (a) shows only 2 μs, to better show the variation with changing initial ionization. (d) is included as an example of the insensitivity of the model to the neutral interaction reaction rates.

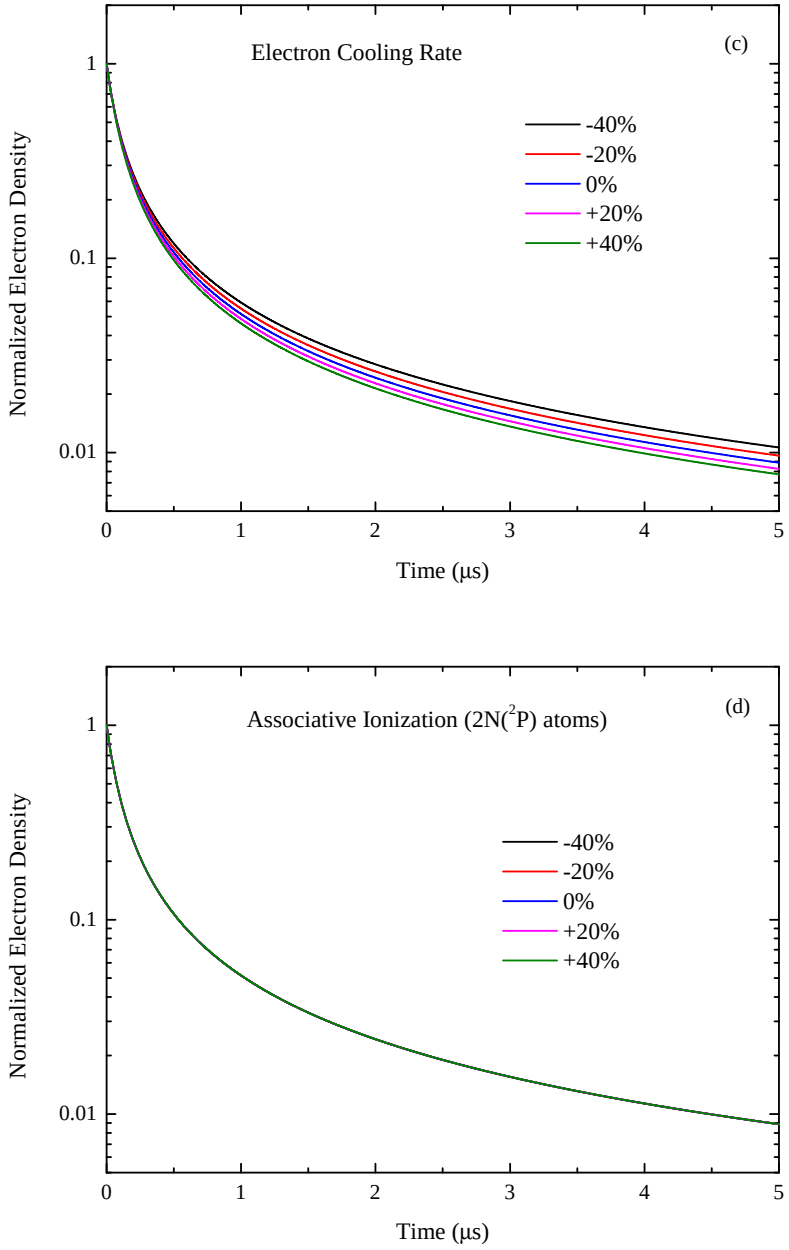

Figure 5.18: (continued)

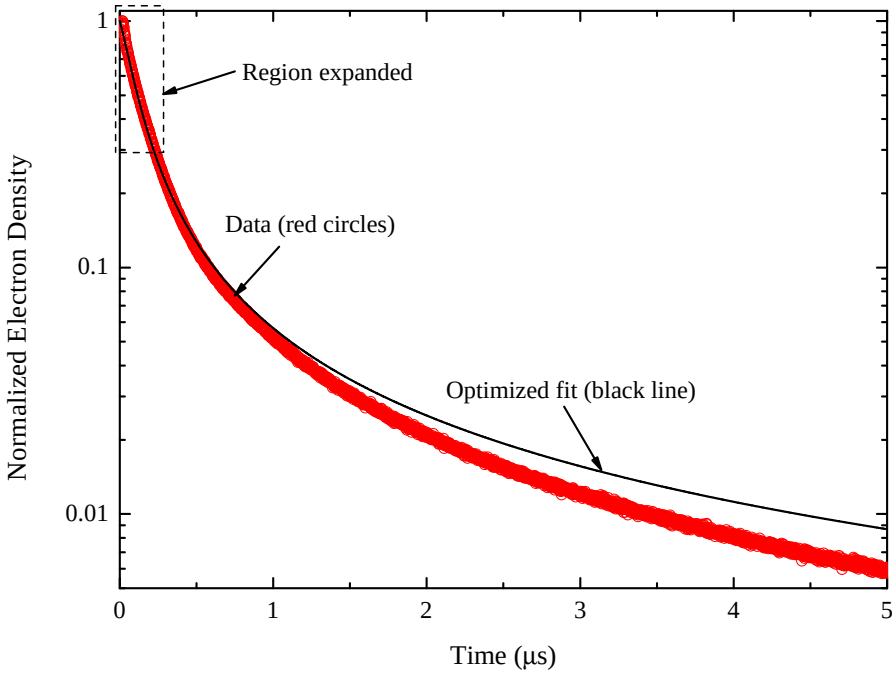

Figure 5.19: Fit data for 300 Torr of nitrogen, using $\alpha_D = 1 \times 10^{-6}$ cm^3 s^{-1}. Fits for 200-500 Torr were similar.

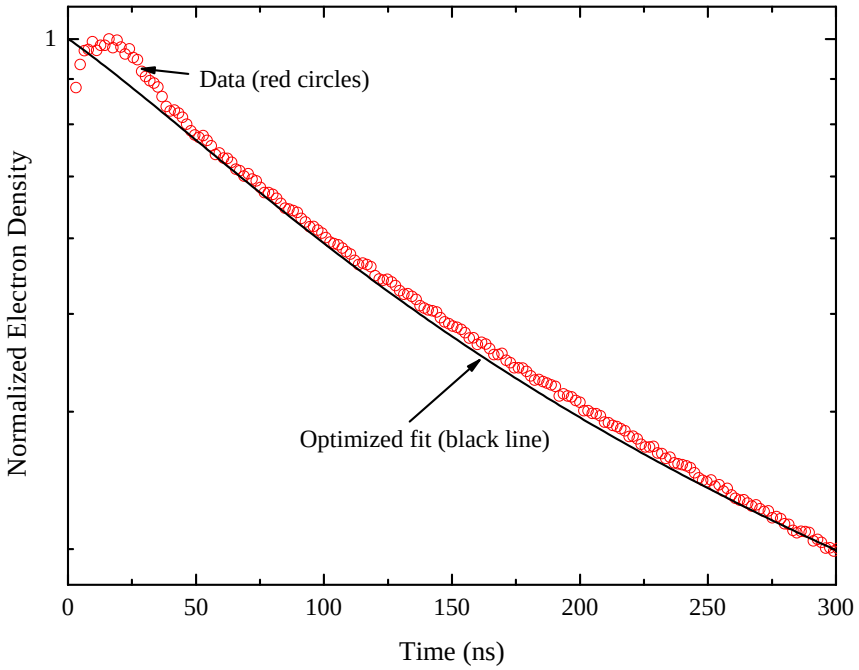

Figure 5.20: Expanded section of the graph in Fig. 5.19, showing the fit inconsistency at times <50 ns.

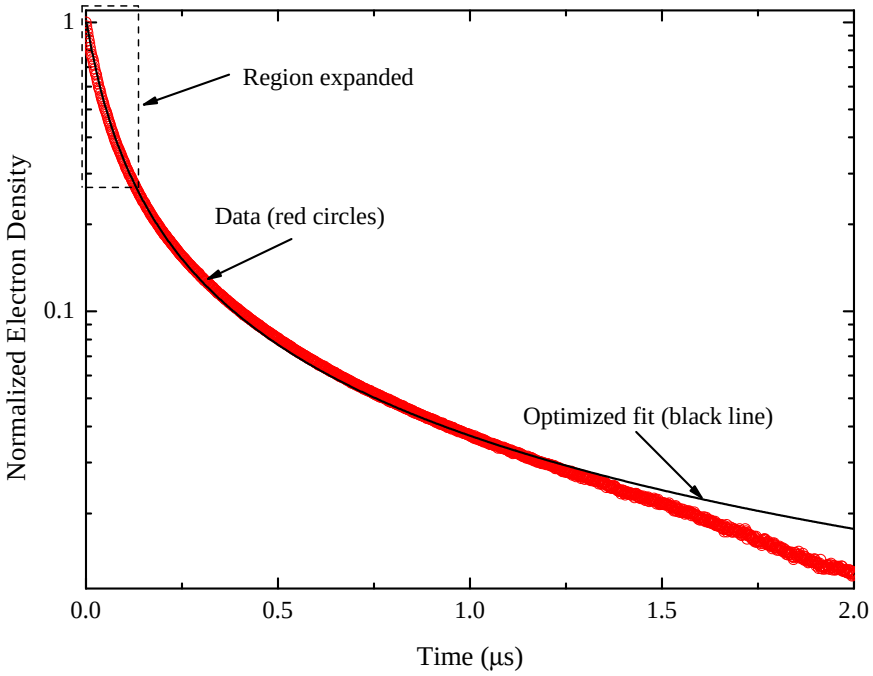

Figure 5.21: Fit data for 30 Torr of nitrogen, using $\alpha_D = 3.25 \times 10^{-6}$.

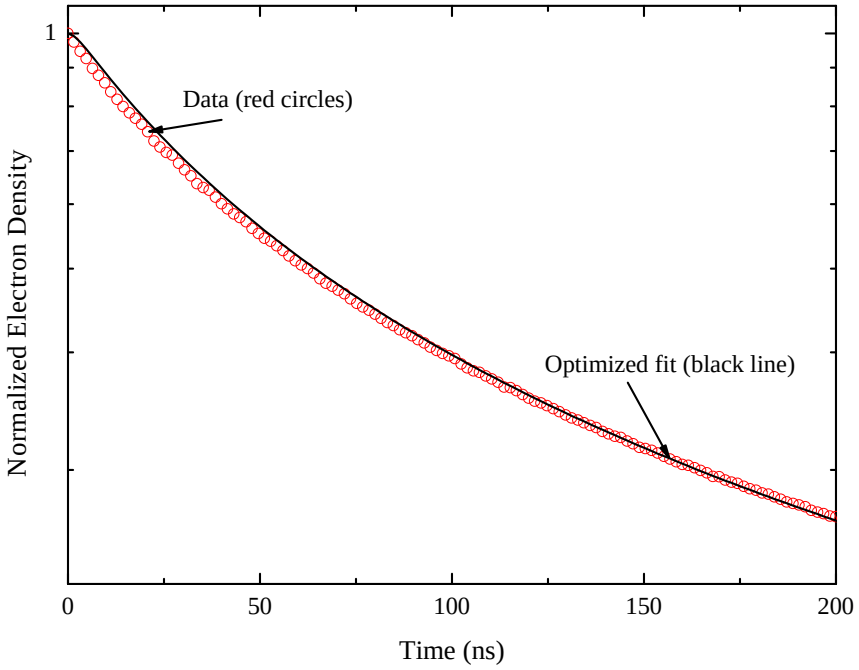

Figure 5.22: Expanded section of the graph in Fig. 5.21, showing the monotonically decreasing electron density.

At pressures below 100 Torr, the electron density decreased monotonically from time $t = 0$, so the fit converged more reliably. This is shown in Figs. 5.21 and 5.22. The extracted values for α_D were in the range 2.55-3.25$\times 10^{-6}$ cm^3 s^{-1} for pressures in the range 100-30 Torr. In these and the graphs for 300 Torr, the fit diverges at the longer timescales. The behavior in this region is dictated more by the excited state interactions, which are not included in detail in the present model, accounting for this divergence.

5.2.2 Discussion

The dissociative recombination reaction in nitrogen has not been the subject of as much research as that of argon. The principal research interest in the nitrogen afterglow focuses on the long-lived "pink afterglow", which lingers on the millisecond time scale. This is much longer than the region of interest in this thesis. A summary of previous measurements is listed in Table 5.6.

The first measurement of recombination rates in nitrogen was by Biondi and Brown in 1949, who measured a rate of 1.4×10^{-6} cm^3 s^{-1}, noting a marked rise in the rate with increasing pressure [52] over a range of 2-8 Torr. In a later study, Kasner and Biondi [73] observed that the prevalence of the tetratomic ion at pressures greater than 10^{-2} Torr made the previous studies not applicable to the diatomic atom, as was previously thought, "leading to considerable confusion in the literature." They also noted that the long lived excited states in the nitrogen afterglow made it difficult to achieve the appropriate experimental conditions to isolate the recombination processes. They estimated the rate of N_4^+ recombination to be 2×10^{-6} at pressures 0.1-0.5 Torr.

Optical emission spectroscopy was employed by Sauer and Mulac in 1972 [74], who made the first temperature dependence measurement, estimating it to be $T^{-1/2}$, with $\alpha_D = 1.4 \times 10^{-6}$. More recently, the temperature dependence was measured by Whitaker *et al.* in 1981, who reported $\alpha_D = 1.6 \times 10^{-6} \left[T_e(K)/300\right]^{-0.41}$ [75]. Two studies in 1991 reported considerably higher values for the dissociation rate constant. Cao and Johnsen reported $(2.6 \pm 0.3) \times$

Table 5.6: Previous measurements of the tetratomic ion (N_4^+) dissociative recombination rate in nitrogen.

Reference	α_D ($cm^3\ s^{-1}$)	Pressure (Torr)	Temperature (K)	Production Technique	Analysis Technique
[52], 1949	1.4×10^{-6}	2-8	300	Microwave	Microwave cavity
[73], 1965	2×10^{-6}	0.1-0.5	300	Microwave	Microwave cavity and Mass spec
[74], 1972	$(3 \pm 0.6) \times 10^{-6}$	280-980[a]	300-500	Electron beam	Optical emission
[75], 1981	$(1.4 \pm 0.2) \times 10^{-6}$	0.01-0.1[b]	300-5600	Microwave	Mass spectrometry
[76], 1991	$(2.6 \pm 0.3) \times 10^{-6}$	<10[c]	300	Photoionization by He resonance	Optical emission
[77], 1991	$(4.6 \pm 0.9) \times 10^{-6}$	760-1315		Electron beam	Mass spectrometry[d]
Present work	$1 - 3.25 \times 10^{-6}$	10-300		Laser-induced breakdown	Microwave interferometry

[a] Measured $T^{-1/2}$ dependence

[b] Used 8-20 Torr of neon, and measured $[T_e(K)/300]^{-0.41}$ dependence

[c] Helium pressure 300-800 Torr, less than 1% nitrogen.

[d] Used a unique "time-resolved atmospheric pressure ionization mass spectrometer" (TRAPI)

10^{-6} [76], and Ikezoe *et al.* reported $(4.6 \pm 0.9) \times 10^{-6}$ [77]. Cao and Johnsen attributed the discrepancy with the results of Whitaker *et al.* to the difference in the plasma production methods. The microwave method employed by Whitaker *et al.* results in a higher vibrational temperature of the nitrogen molecules and ions, which could affect the recombination coefficient. The method used by Ikezoe *et al.* was too different from the others for meaningful comparison.

The result from the fit in the present work is significantly lower than the previously reported values in the higher pressure regime, especially for those measurements of comparable pressure ranges (Ikezoe and Sauer and Mulac). The lower pressure data is more consistent with previous results. Similarly to argon, there is a pressure "gap" between the high pressure and low pressure studies, from 10-250 Torr, which is where the fit converged well in the present work. As regards the higher pressure regime, many of the studies only measure the recombination rate in the late afterglow, on the millisecond timescale. From Fig. 5.15, it is clear the the decay rate is different in the early afterglow. Some of this can be attributed to the cooling rate of the electrons and the temperature dependence of α_D, but there may be other factors. The slow rate constants for the excited state neutral interactions that result in the long-lived afterglow will also impact electron production mechanisms in the late afterglow, resulting in a different electron density profile than in the short afterglow.

The present work offers both a new measurement technique and data in a unique pressure range not previously studied. Filling the gap between the low and high pressure studies of the nitrogen tetratomic recombination coefficient, it also provides new insight into the short-term (<1 ms) afterglow in atmospheric pressure plasmas. Furthermore, the data shown in Fig. 5.20 suggest that there are additional electron production mechanisms not accounted for by the associative ionization reactions.

Chapter 6

Conclusions

This thesis has demonstrated a new laboratory tool for the study of plasma gas kinetics using an ultrafast laser as a δ-function excitation source and an X-band microwave interferometer for time-resolved electron density measurements. While separately, neither ultrafast lasers nor microwave interferometry is a new technique, the synthesis has resulted in a rich environment for electron density decay measurements. Gas kinetic models in argon and nitrogen have yielded remarkable agreement with the measured electron density over almost an order of magnitude in pressure. The models were developed from the minimal set of reactions necessary to capture the essential physics, resulting in a sufficiently small parameter space that key dissociative recombination rate constants were extracted from optimized model predictions.

With the advancement of both computing technology and theoretical methods, the most recent experimental data for recombination rate constants and MPI cross sections predates theoretical calculations by at least a decade. New measurement techniques are crucial to continue moving the field of plasma gas kinetics forward. The ubiquity of compact fluorescent light bulbs, plasma television displays, and semiconductor plasma processing has made an accurate understanding of plasma reactions more important than ever, for which task the diagnostic system developed in this thesis is uniquely suited. One of the key advantages is the capability to investigate plasma channels in any non-corrosive gas at a pressure range of at least three orders of magnitude, enabling analysis of the wide range of plasma environments that occur in industrial and commercial plasmas.

Rigorous testing of the microwave interferometer has shown a time resolution of a few

nanoseconds (bandwidth of ≈1 GHz), which proved to be more than sufficient to study the decay dynamics in the rare gases and nitrogen. Even in oxygen, in which, at atmospheric pressure, free electrons have a lifetime of only a few nanoseconds, the sensitivity of the interferometer to electron densities below 10^{11} cm^{-3} would allow the electron density decay in the late afterglow to be probed. Furthermore, data acquired with an oscilloscope with a bandwidth of 8 GHz has demonstrated that the microwave diodes have a potential for time resolution of hundreds of picoseconds, if the temporal response of the magic-tee can be improved.

Gas kinetic models in argon and nitrogen have been developed, and have demonstrated impressive predictive capabilities. Rate constants for dissociative recombination in both gases have been determined by optimizing the model to reproduce the measured electron density decay profiles. In good agreement with previous measurements, the present work reports rate constants in a pressure range that has remained poorly characterized, with no values previously reported in the pressure range of 20-200 Torr. In argon, the MPI cross section was estimated to within a few orders of magnitude, with the possibility of improving the estimate with better knowledge of the laser pulse parameters. With only one previous measurement of this cross section, and several recent theoretical calculations, the combination of microwave interferometry and ultrafast UV laser pulses provides an exciting new opportunity to measure this and other rare gas MPI cross sections.

While the ultrafast UV laser system described here will likely be superseded by rapid advances in reliable high power lasers, the interferometer has proven the worth of revisiting diagnostic techniques that have "gone out of style." Old techniques applied to new technology has demonstrated advantages over even the most cutting edge optical spectroscopic methods. With appropriate end windows the interferometer described here could be used with any laser source with sufficient intensity to ionize a gas, which, combined with the pressure range, low detection limit, and gas versatility allows an almost unparalled range of possible gas-phase plasma investigations.

Appendix A

Absolute Electron Density Measurements of Plasma Filaments

As discussed in Sec. 2.2, there has been considerable interest in determining the electron density behavior in filaments generated in air by ultrafast laser pulses. In addition to the rare gas and nitrogen pure gas studies described in Chapters 3-6, experiments were done using a few-picosecond laser operating in atmospheric pressure in air. These experiments were done at the laboratories of Ionatron, Corp. (now Applied Energetics) in Tucson, Arizona. Many of the methods are the same as those used in Sec. 3.2, so only differences will be highlighted.

A.1 Experimental Techniques

Few-picosecond near-IR laser pulses with energies up to 450 mJ were produced by a Ti:sapphire Chirped Pulse Amplification (CPA) system. A regenerative amplifier was seeded by a femtosecond oscillator, which was followed by a cryogenically cooled multi-pass linear amplifier with two Q-switched pump lasers and a double grating compressor. The laser pulses were generated at a repetition rate of up to 10 Hz with pulse energies up to 450 mJ. Pulse widths were limited to 900 fs by the damage threshold of the steering optics. Focusing optics produced self-propagating filaments, which were sustained for many meters. A diagram of the laser system is shown in Fig. A.1.

The electron density profiles of the plasma filaments produced by the laser described above were measured by the same interferometer equipment described in Sec. 3.2. There were a few differences between the two experimental arrangements, the primary difference being that the interferometer was not vacuum sealed for the measurements of the plasma fil-

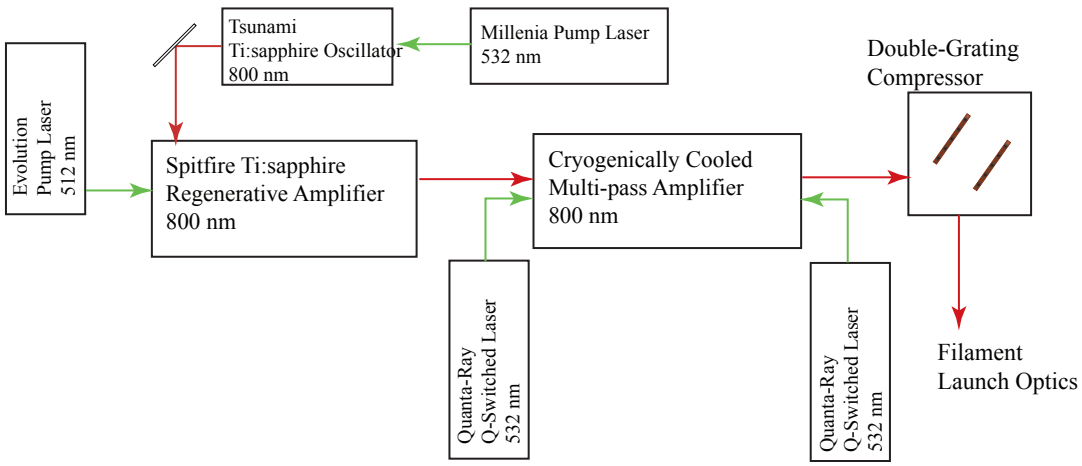

Figure A.1: Schematic of the CPA laser system at Ionatron, Corp. in Tucson, Arizona. Output is few-picosecond, up to 450 mJ pulses at a rate of 10 Hz.

aments. It was not necessary to seal the interferometer because the filaments were generated at atmospheric pressure in air. Additionally, there were multiple monitoring systems and locations to capture other information about the filaments. The experimental run was limited to three days, and could not be repeated, so it was critical to gather all relevant information during operation. A diagram showing the physical arrangment of the interferometer and all the monitoring systems is shown in Fig. A.2.

Filaments were produced by focusing the laser pulses with a lens, as compared with the UV laser generated plasma channels, which were produced by focusing with a curved mirror. To control the filling factor in the waveguide, and to select the number of filaments, the focused laser pulses were directed through an aperture before entering the holes in the waveguide E-bends. This also reduced the contribution to the measured electron density profile of electrons from impact ionization as a result of the beam periphery hitting the edge of the waveguide. Real time power measurements of the pulse were not possible without perturbing the pulse propagation and thereby disrupting filament production, and also damaging the

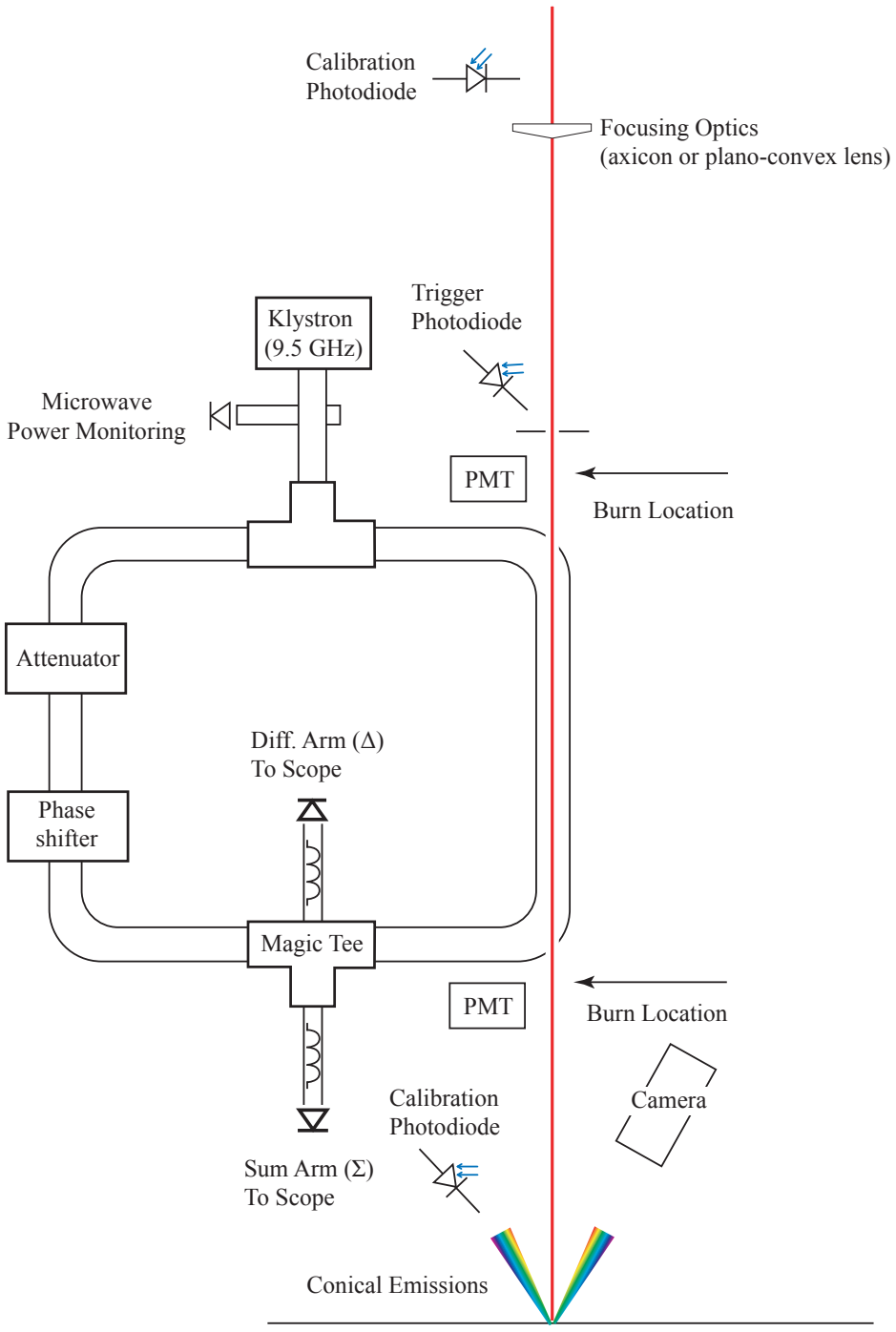

Figure A.2: Schematic of full-bridge interferometer used to measure IR filaments, showing the positions of all calibration, monitoring, and measurement detectors.

power meter. Periodic calibrations were performed at low power by measuring laser power with a power meter at positions before and after the waveguide, and simultaneously recording data from two photodiodes. The photodiode data was used to extrapolate the actual shot-to-shot power before and after the waveguide. For further data filtering and analysis, conical emissions [78] were imaged with a CCD camera, two photomultiplier tubes (PMTs) recorded the relative intensity of N_2^+ fluorescence, and burn patterns were recorded on plastic film before and after the waveguide. The burn patterns were imaged with a microscope and a CCD camera. A portion of the microwave signal was monitored to verify that there was no significant drift in the klystron output. The theory and data analysis of the electron density measured by the interferometer was identical to that described in Chapter 4.

A.2 Results

A.2.1 Investigation of Filaments Generated by an Axicon Lens

The first data were acquired with the laser beam passing through an axicon lens, producing consistent filaments a few meters from the lens. The filaments were directed through a 10 mm aperture before entering the 9.5 mm holes in the waveguide E-bends, with the goal of maximizing the filling factor in the waveguide, but but reducing electron production by impact ionization as a result of the beam periphery hitting the waveguide. The lens and interferometer were adjusted to locate the median filament creation point at the beginning of the waveguide interferometer arm.

The PMT signals and the microwave diode signals were collected by a Tektronics TDS5104B 1 GHz Digital Phosphor Scope. The photodiode signals were collected by a Tektronics TDS5054B 500 MHz Digital Phosphor Scope. Representative microwave data from the sum (Σ) and difference (Δ) arms is shown in Fig. A.3 and sample phase, attenuation, and electron density are shown in Figs. A.4 and A.5. The bandwidth of the scope was only 1 GHz, as discussed in Sec. 3.2.2, so features shorter than 1 ns were not captured. The initial peak

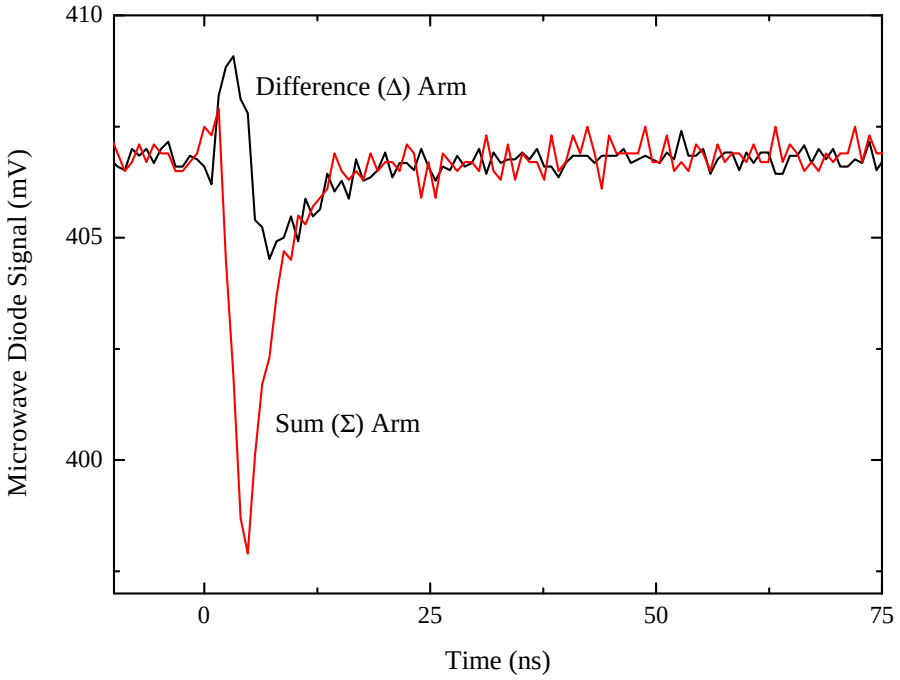

Figure A.3: Representative data from the two arms of the magic-tee

in the electron density has been measured to be shorter than 1 ns [28], and as a result of the limited bandwidth of the oscilloscope and the interferometer, the peak electron density measurements were lower than previously measured (see Sec. 2.2 for discussion of previous measurements).

To examine peak electron density as a function of pulse energy, the pulse energy (measured before any lenses or apertures) was decreased incrementally from the maximum laser power, a pulse energy of 235 mJ, down to the point at which filament formation became sporadic and unreliable, which occured at a pulse energy of 190 mJ. Using the calibration photodiode data, the laser pulse energy entering the waveguide was extrapolated from calibration data acquired at low power. Figure A.6 indicates peak electron density variation with pulse energy. There were several calibration low power calibration measurements used to extrapolate pulse energy, giving an error range for the actual laser/filament power entering the waveguide. The pulse width was measured by autocorrelation to be 4 $\pm$ 0.1 ps

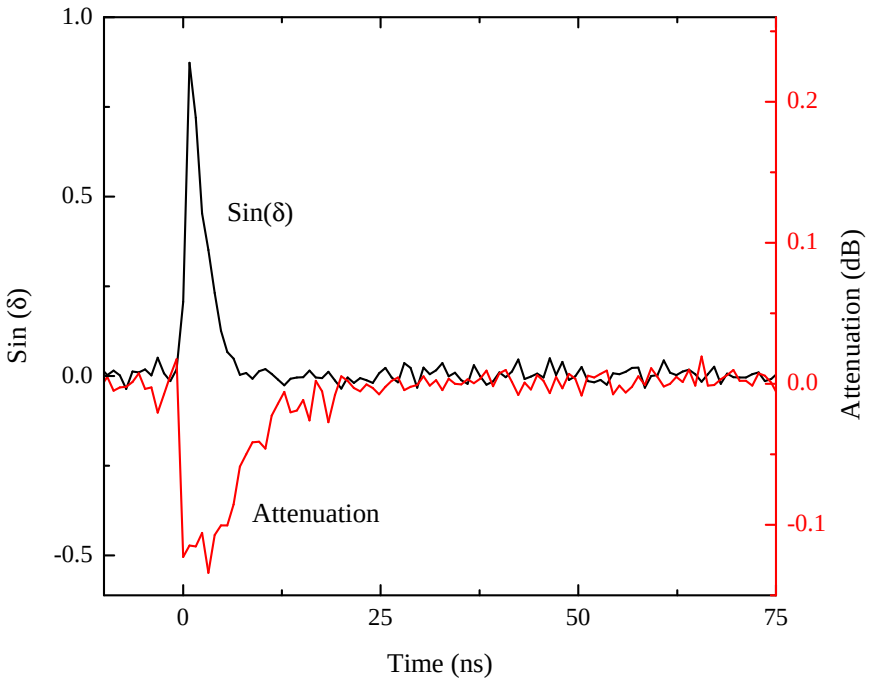

Figure A.4: Representative data illustrating the temporal variation of the attenuation and the sine of the phase shift (δ)

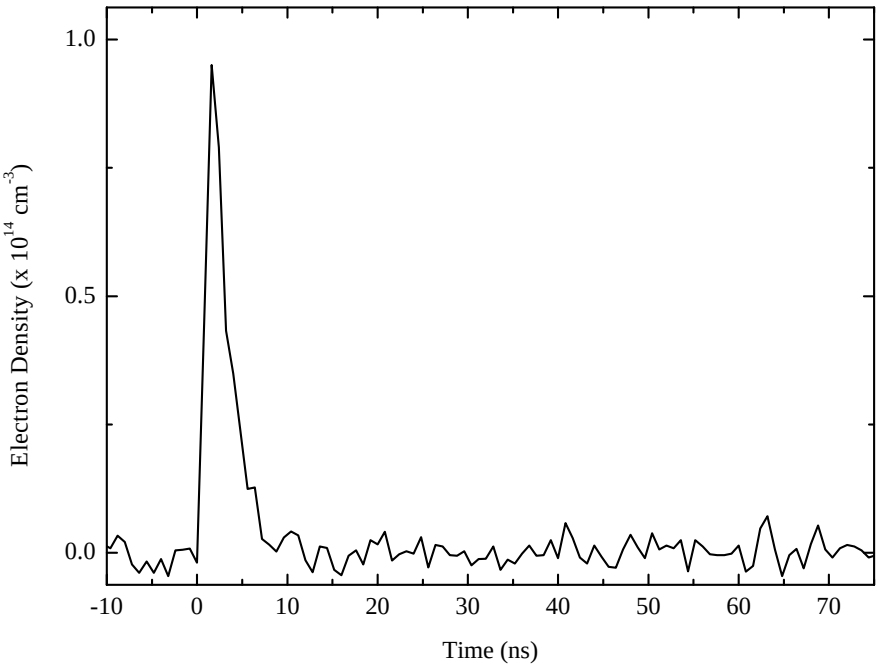

Figure A.5: Representative electron density measurements.

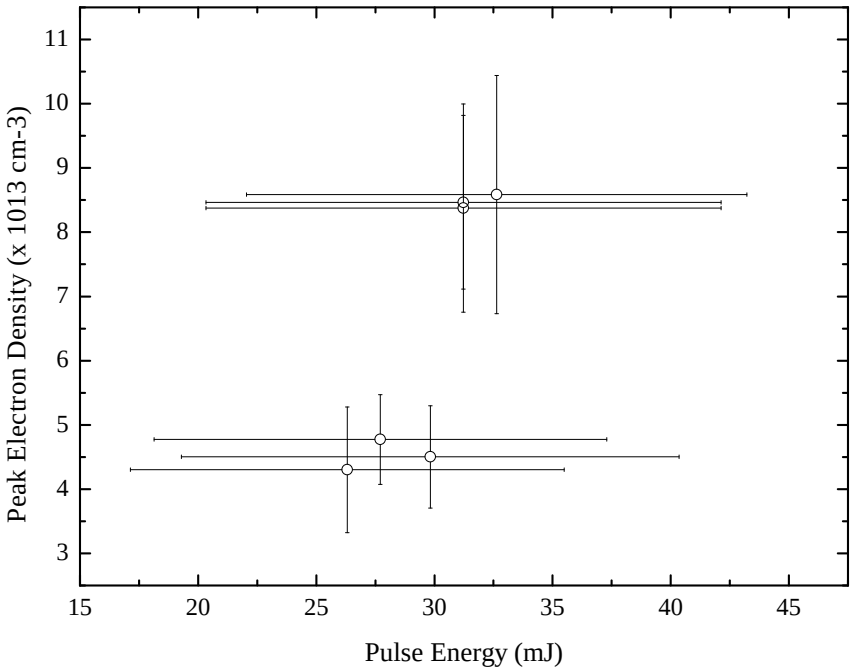

Figure A.6: Peak electron density variation with pulse energy.

The peak electron density is expected to fit to an equation of the form $n_e \propto I^n$, where n_e is the electron density, I is the laser intensity, and n is some power that indicates the order of the nonlinear process that produces the electrons, as discussed in Sec. 5.1.3 with reference to multiphoton ionization (MPI). The data are consistent with a value of n in the range 5-11, which overlaps well with the order of MPI that would be necessary to ionize atmospheric gases, given a photon energy of 1.55 eV ($\lambda = 800$ nm). The ionization threshold and number of photons necessary for MPI listed in Table A.2.1 for the major gas constituents of Earth's atmosphere.

A similar investigation was undertaken to determine the effect of pulse width on peak filament electron density. The pulse width decreased incrementally from 3.2 ps to 0.9 ps, at which point the peak intensity of the laser pulse reached the damage threshold of the steering optics. The pulse width was measured between each data acquisition by autocorrelation. Pulse energy calibrations showed no significant drift in laser power over the range of pulse widths tested. With no variation in pulse energy, a shorter pulse width results in a higher

Gas	Ionization Energy (eV)	Number of photons for MPI
O_2	12.06	8
N_2	15.58	10
Ar	15.76	10
CO_2	13.77	9

Table A.1: The ionization energies of atmospheric gases, and the number of 800 nm, 1.55 eV photons required to ionize them.

peak laser power which, in turn, is expected to produce a higher peak electron density. This is consistent with the results shown in Fig. A.7

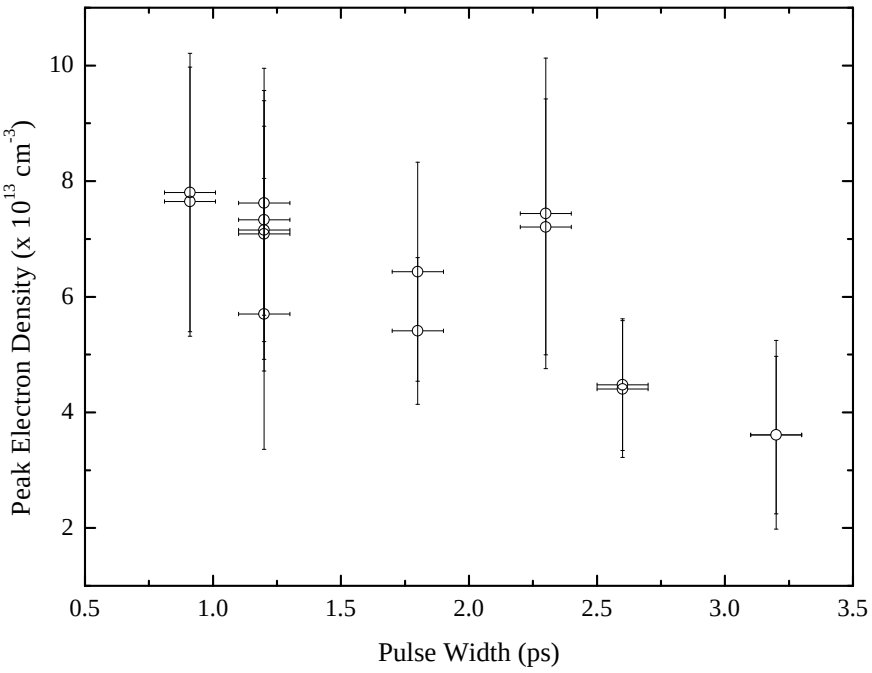

Figure A.7: Peak electron density variation with pulse width, showing the expected decrease in peak density for longer pulse durations.

There has been significant recent research into the effects of the filament energy reservoir, a low intensity background region as much as 10 times the cross-sectional area of the filament itself, and containing up to 50% of the pulse energy [79][80]. Shown in Fig. A.8 are false-color burn patterns taken before (top) and after (bottom) the waveguide. Plastic film was placed in the path of the beam, and the resulting burn was imaged using a microscope

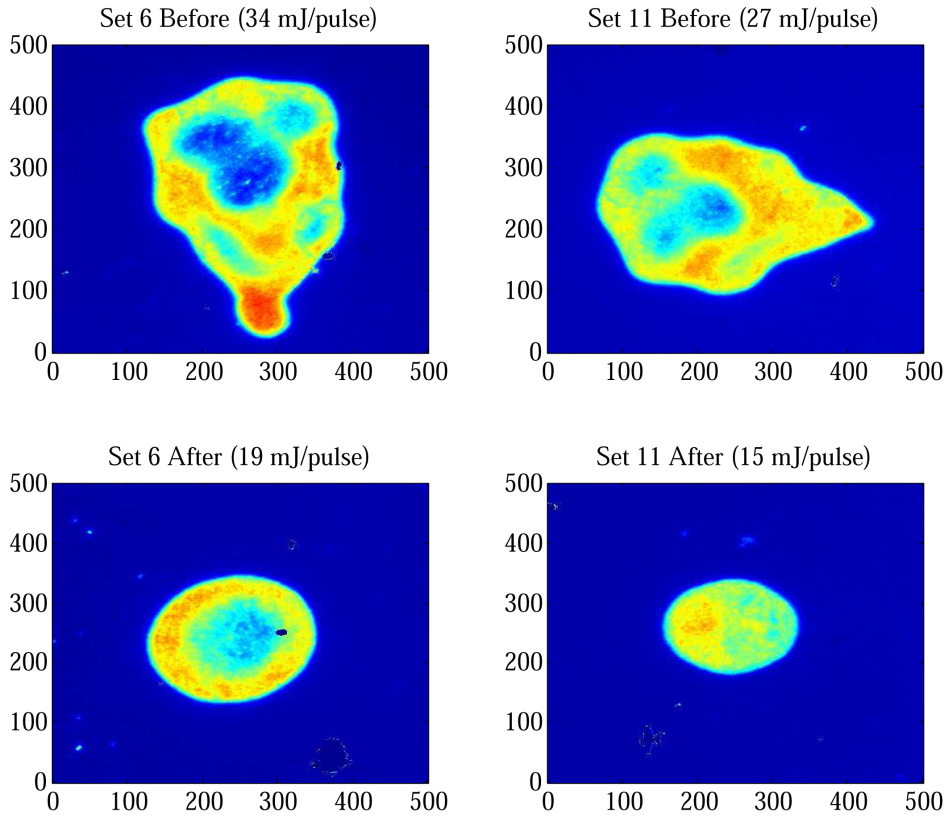

Figure A.8: False color burn patterns taken before (top) and after (bottom) the waveguide. Both axes are in microns (μm).

and a monochrome CCD camera. The burn patterns shown in the top row imaged the filament immediately after the first aperture, so the reduction in the energy reservoir had not yet affected the filament. Burn patterns imaging the filament after exiting the waveguide are rounder and more uniform, most likely as a result of the cylindrical aperturing of the background reservoir. Figure A.9 shows the change in the filament cross section with changing pulse energy, imaged after exiting the waveguide. The burn intensity shows a change in structure, transitioning from a ring to a uniform circle as pulse energy was decreased, additionally, the radii of the filaments decreased from 200μm to 150 μm.

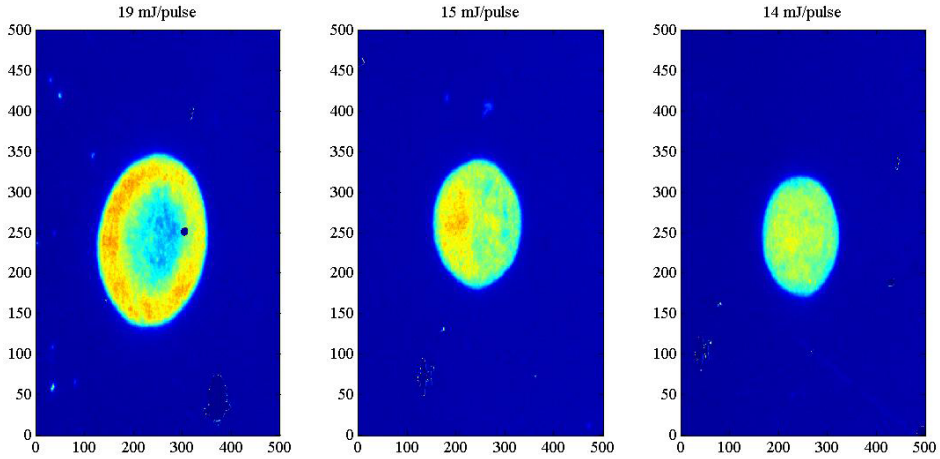

Figure A.9: False color burn patterns taken after the waveguide for several energy levels, showing the the change in the shape and profile of the filament cross section with pulse energy variation. Axes in microns.

A.2.2 Investigation of Filaments Generated by an Traditional Plano-convex Lens

The axicon lens produces consistent and reliable filaments, but it is not the most common focusing optic used to generate filaments. To examine filaments that are more consistent with other investigations, the beam was directed through a plano-convex lens with a focal length of several meters. The microwave interferometer was moved ten meters from the lens, with the same calibration and monitor detectors shown in Fig. A.2. The peak filament production point was adjusted to coincide with the entrance of the experimental arm of the interferometer. The lens produced filaments in consistent locations in the plane perpendicular to filament propagation, so one filament was apertured out using a steel plate with a 1 mm hole in it.

To increase the time resolution of data acquisition with the goal of capturing more of the initial peak of the electron density profile, the microwave diode signals from the sum and difference arm of the interferometer were collected by an 8 GHz bandwidth Tektronics DSA 70804 Digital Serial Analyzer. The sampling rate of this scope was 25 GS/s, and the signal contained a large noise component at 9.2 GHz, which was the frequency of the microwaves

propagating in the interferometer. The Fast Fourier Transform (FFT) of the signal is shown in Fig. A.10, and a sample waveform before and after filtering the 9.2 GHz is shown in Fig. A.11. This is the same data discussed in Sec. 3.2.2 regarding the bandwidth of the interferometer.

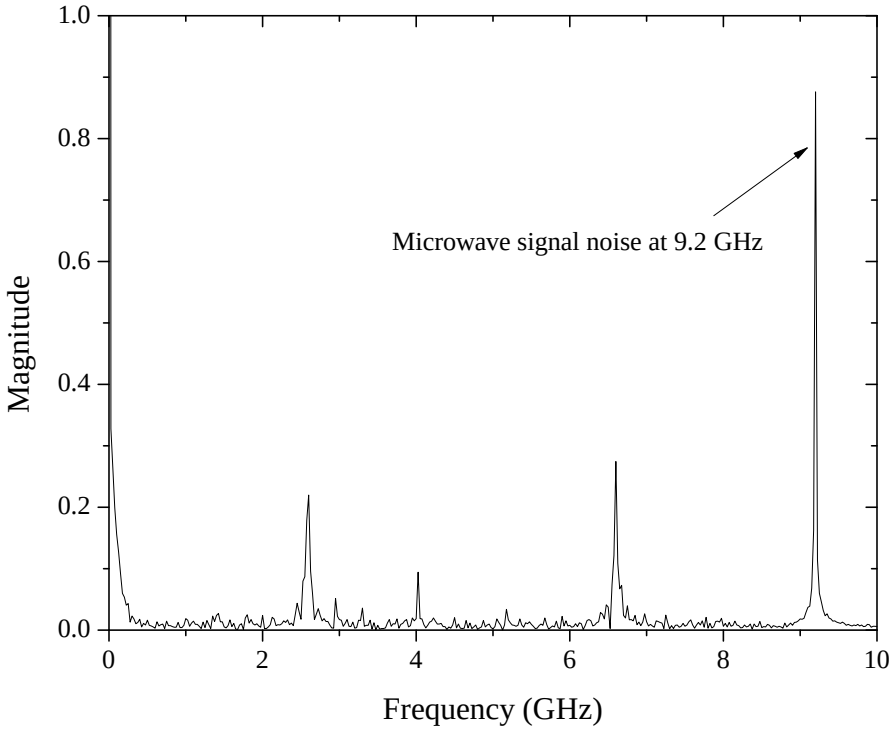

Figure A.10: Fast Fourier Transform (FFT) of a sample waveform, showing the large contribution at 9.2 Ghz.

Representative data from the sum and difference arms of the interferometer, calculated phase shift and attenuation, and electron density are shown in Figs. A.12, A.13, and A.14, respectively, all after filtering out the 9.2 GHz noise component. The peak electron densities are about a factor of two higher than those measured for filaments produced by the axicon lens focusing optic. This could be due to different filament production methods, which result in filaments of a smaller diameter (measured by burn patterns), or to the higher bandwidth of the DSA 70804, which captures more of the initial peak of the electron density profile.

In a manner similar to that described for the filaments generated by focusing the laser

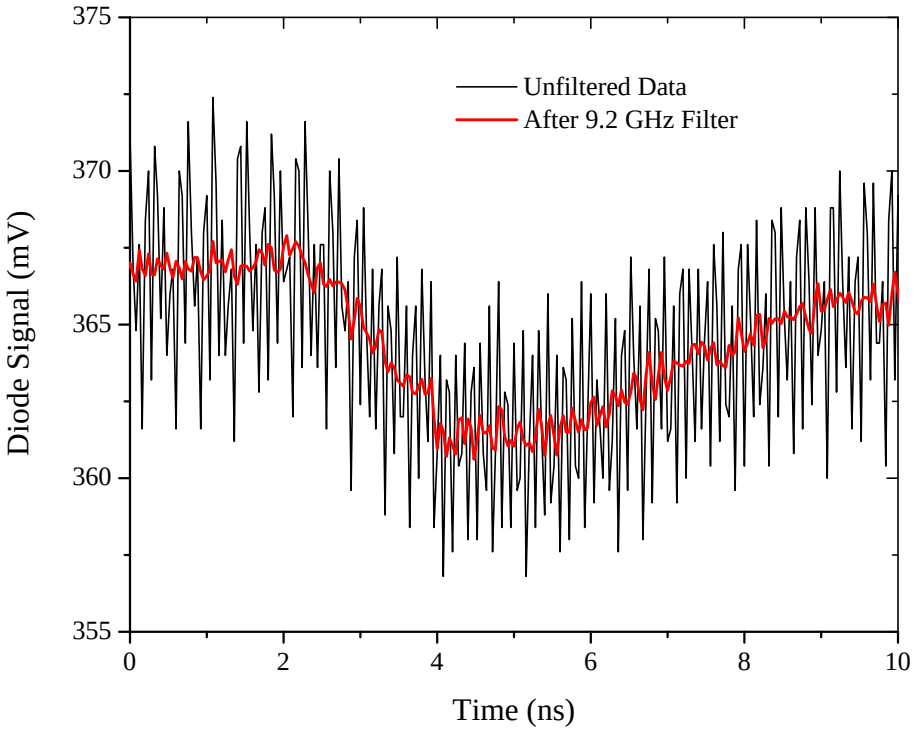

Figure A.11: A sample raw waveform and the filtered data with the 9.2 GHz noise removed.

with the axicon lens, the effect of pulse energy on peak electron density was investigated. The maximum pulse energy was 250 mJ and the energy was again decreased incrementally to the point at which filament formation became sporadic and unreliable, which occured at a pulse energy of 175 mJ. This is slightly below the lowest pulse energy sufficient to form filaments when the laser was focused with the axicon lens. The pulse width during these measurements was 1.6 ps, which is shorter than the 4 ps pulse width of the laser pulses resulting in the data summarized in Fig. A.6, possibly explaining the lower pulse energy threshold. Pulse energy was extrapolated from the low power calibration data in the same manner as for the data in Sec. A.2.1. Figure A.15 shows peak electron density variation with pulse energy. Unfortunately the error in pulse energy extrapolation and the variation in peak electron density were so large that it is not possible to draw definite conclusions regarding the effect of pulse energy on peak electron density. There is a slight upward trend with increasing pulse energy, which is the expected result, but the data would also be consistent

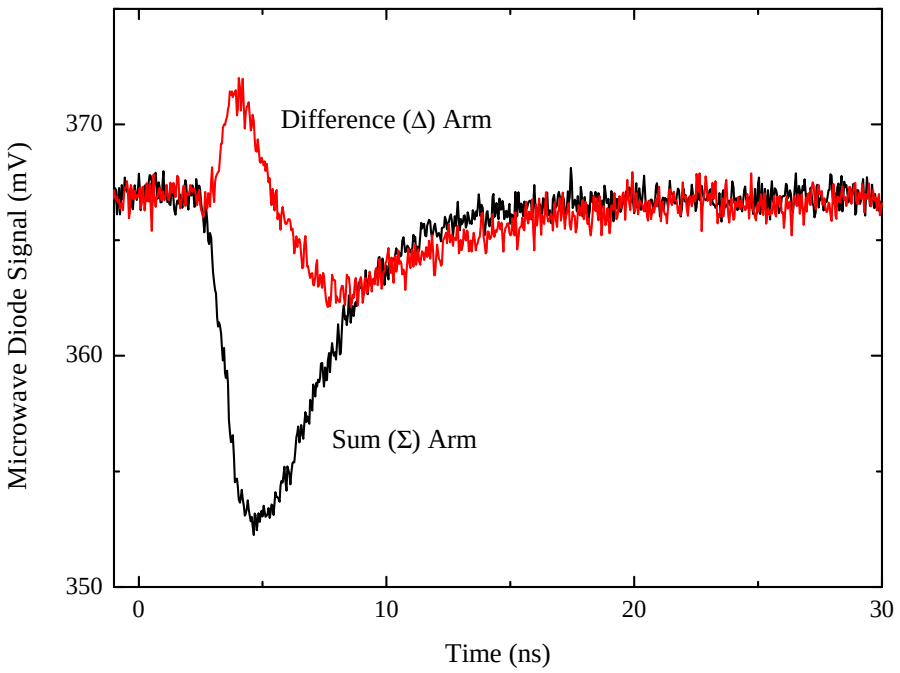

Figure A.12: Representative (filtered) data from the sum and difference arms of the interferometer.

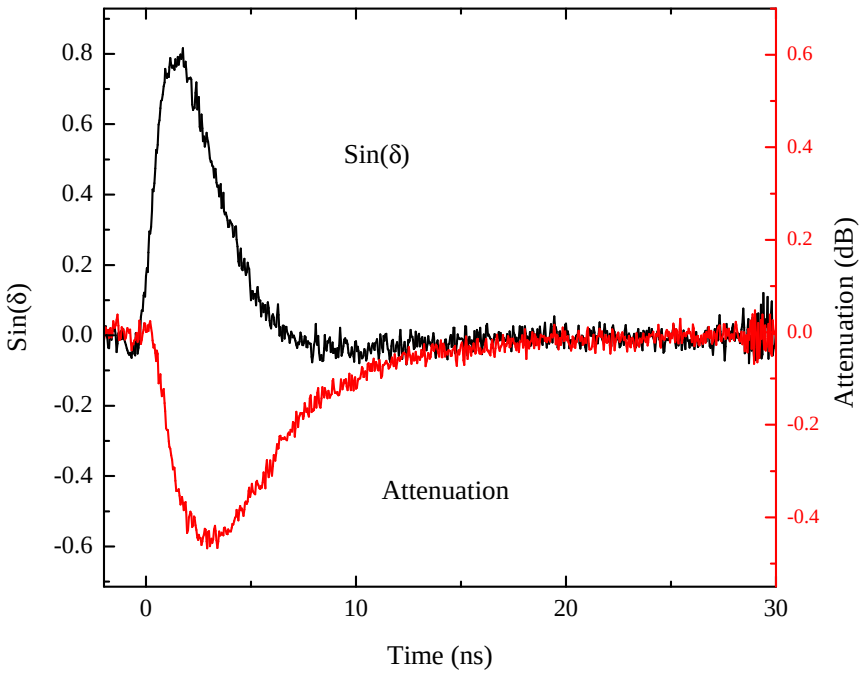

Figure A.13: Representative data illustrating the temporal variation of the attenuation and the sine of the phase shift (δ).

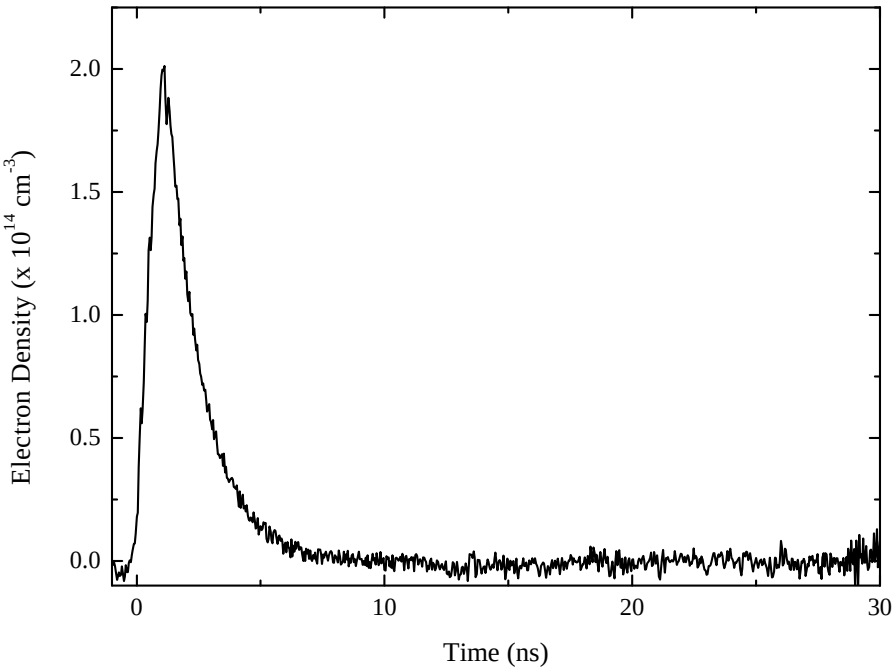

Figure A.14: Representative electron density measurements.

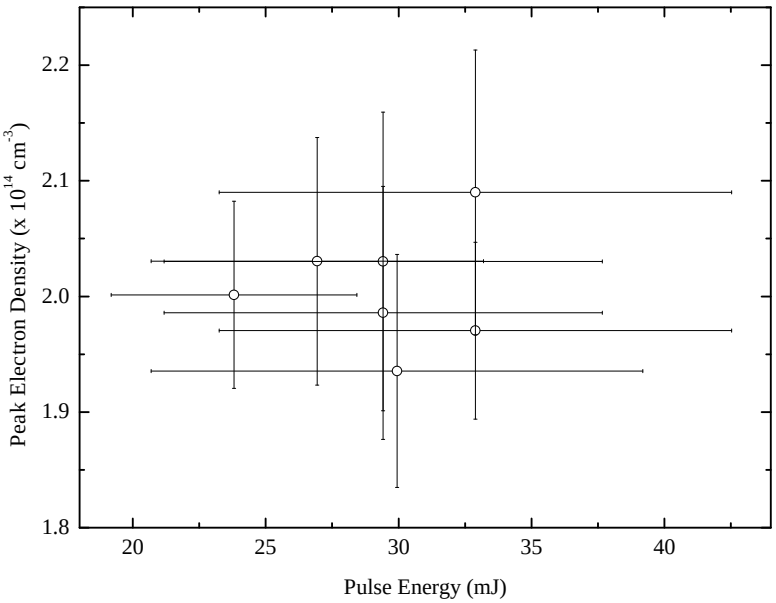

Figure A.15: Peak electron density variation with pulse energy for filaments generated by focusing the laser with a traditional plano-convex lens.

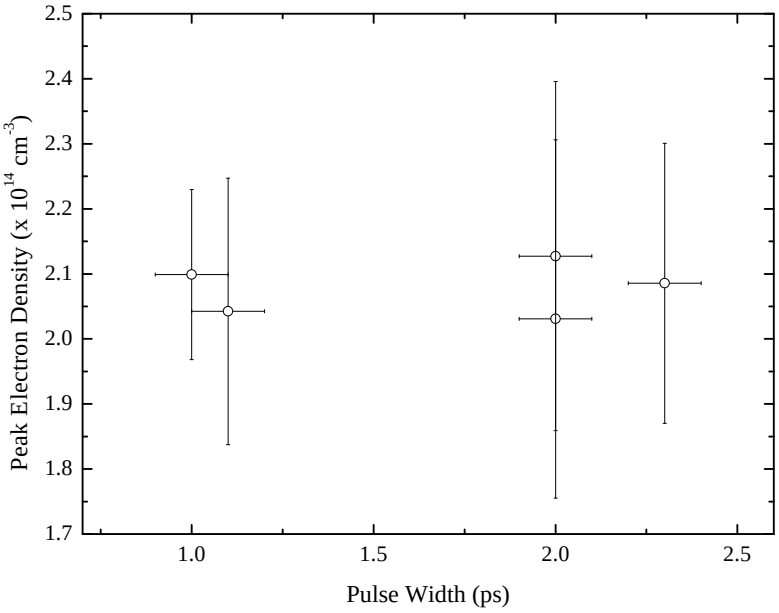

Figure A.16: Peak electron density variation with pulse width.

with the conclusion that pulse energy had no effect on peak electron density

The effect of pulse width on peak electron density was investigated in a range of pulse widths between 1 ps and 2.3 ps. The data, shown in Fig. A.16 are, in a similar manner as the data shown in Fig. A.15, obscured by the large variation in peak electron density, as indicated by the error bars. Even in the absence of such large error, the average peak electron density shows no discernable trend over the pulse widths investigated.

While the burn patterns from the data acquired when focusing the laser pulse by an axicon lens, discussed in section A.2.1, showed a marked difference in shape after passing through the waveguide, the burn patterns from the plano-convex lens showed no systematic shift in filament cross-sectional structure after passing through the waveguide. The size of the filaments was smaller than those produced by the axicon lens, averaging around 50-60 μm, compared to 220-150 μm. The filament cross sections were found to match one of three distinct structural forms, spots, rings, and targets, comparable to Laguerre-Gaussian TEM_{00}, $TEM_{01}*$, and TEM_{10} modes, commonly used to describe laser beam mode structure. Representative burns, all acquired at the same pulse energy (175 mJ per pulse before lenses

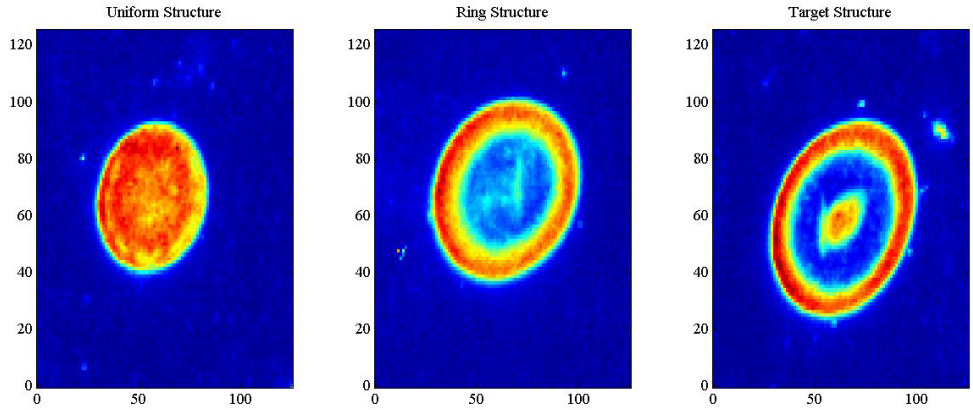

Figure A.17: False color burn patterns showing filament intensity cross sections for pulses with a width of 1.6 ps and a pulse energy of 175 mJ. Axes in μm.

and apertures) and pulse width (1.6 ps) are shown in Fig. A.17. These ring structures have been observed in other IR-laser filament experiments, and have been explained as being a result of the self-focusing of the laser pulse and defocusing due to the plasma [81].

In conclusion, we have non-perturbatively measured the absolute time-resolved electron density for laser induced filaments for two different filament production methods, and over a range of pulse width and pulse energy. In the measurements of filaments produced by focusing the laser with an axicon lens, the energy reservoir was largely unperturbed by apertures, leading to the expected dependencies of peak electron densities on pulse width and energy. These results were also consistent with the multiphoton ionization of atmospheric gases. The axicon lens also produced fewer, larger diameter filaments than the plano-convex lens, all of which were allowed into the waveguide, as compared to the one filament which was selected by an aperture out of those produced by the plano-convex lens. The two clusters of peak densities shown in Fig. A.6 could be a result of filament number quantization, resulting in one density when there was one filament in the waveguide, and another when there were two filaments. The long focal length lens produced many smaller filaments, the aperture was much smaller and selected just one filament to be guided into the interferometer. This drastically reduced the energy reservoir, and resulted in a much more uniform distribution of the peak electron density of pulse width and energy variations.

The peak electron densities reported here are several orders of magnitude lower than those reported by the experiments discussed in Sec. 2.2, likely due to the bandwidth limitations of the magic-tee. Rodriguez *et al.* [28] reported peak electron densities of $1 - 2 \times 10^{16}$ cm^{-3}, but the temporal profile of the electron density decayed past the detection limit of their experimental technique in less than 1 ns. The present work therefore represents a unique capability to investigate the plasma filament behavior for times >1 ns. Detailed knowledge of the decay behavior, at all time scales, of these laser-induced filaments is critical to their use as transient conductors, because it dictates, among other things, the length of time during which the electron density is sufficiently high for the desired application. The experimental methods described here provide an ideal complement to optical-frequency interferometric methods, enabling the investigation of the electron density profile of laser-induced filaments across the full range of time scales and densities.

References

[1] William Crookes. On radiant matter. Lecture to the British Association for the Advancement of Science, August 1879. Friday, August 22nd.

[2] Irving Langmuir. Oscillations in ionized gases. *Proceedings of the National Academy of Sciences of the United States of America*, 14:627–637, 1928.

[3] Michael A. Lieberman and Allan J. Lichtenberg. *Principles of Plasma Discharges and Materials Processing*. John Wiley & Sons, Inc., 2005.

[4] T. J. M. Boyd and J. J. Sanderson. *The Physics of Plasmas*. Cambridge University Press, 2003.

[5] Alexander Fridman and Lawrence Kennedy. *Plasma physics and engineering*. Taylor & Francis Books, Inc., 2004.

[6] D. A. Gurnett and A. Bhattacharjee. *Introduction to plasma physics: with space and laboratory applications*. Cambridge University Press, 2005.

[7] A. G. Gaydon and I. R. Hurle. *The Shock Tube in High Temperature Chemical Physics*. Chapman and Hall, 1963.

[8] National Research Council (U.S.). Plasma 2010 Committee. *Plasma science: advancing knowledge in the national interest*. The National Academies Press, 2007.

[9] I A Kossyi, A Yu Kostinsky, A A Matveyev, and V P Silakov. Kinetic scheme of the non-equilibrium discharge in nitrogen-oxygen mixtures. *Plasma Sources Science and Technology*, 1(3):207–220, 1992.

[10] Blake E. Cherrington. *Gaseous Electronics and Gas Lasers*. Pergamon Press, 1979.

[11] S. Neeser, T. Kunz, and H. Langhoff. A kinetic model for the formation of Ar_2 excimers. *Journal of Physics D-Applied Physics*, 30:1489–1498, 1997.

[12] David J. Rose, Donald E. Kerr, Manfred A. Biondi, Edgar Everhart, and Sanborn C. Brown. Methods of measuring the properties of ionized gases at microwave frequencies. Technical Report 140, Massachuesetts Institute of Technology, Research Laboratory of Electronics, 1949.

[13] J. J. Thomson. Cathode rays. *Philosophical Magazine*, 44:293–316, 1897.

[14] Richard H. Huddlestone and Stanley L. Leonard, editors. *Plasma Diagnostic Techniques*, volume 21 of *Pure and Applied Physics*. Adademic Press, 1965.

[15] J. G. Hirschberg and R. W. Palladino. Deviations from kinetic equilibrium in a stellarator plasma. *Physics of Fluids*, 5(1):48–51, 1962.

[16] Shang-yi Ch'en and Makoto Takeo. Broadening and shift of spectral lines due to the presence of foreign gases. *Rev. Mod. Phys.*, 29(1):20–73, Jan 1957.

[17] R. E. B. Markinson, P. C. Thonemann, R. B. King, and J. V. Ramsay. Dielectric constant and electron density in a gas discharge. *Proceedings of the Physical Society B*, 64:665–670, 1951.

[18] Ladislas Goldstein, M. A. Lampert, and R. H. Geiger. Determination of electron density and collision frequency in a gaseous discharge by microwave propagation measurements. *Electrical Communication*, 29(3):243–245, September 1952.

[19] M. Hercher. Laser-induced damage in transparent media. *Journal of the Optical Society of America*, 54(4):563, 1964.

[20] K. L. Bowles. Observation of vertical-incidence scatter from the ionosphere at 41 Mc/sec. *Physical Review Letters*, 1:454–455, 1958.

[21] A. Javan and P. L. Kelley. Possibility of self-focusing due to intensity dependent anomalous dispersion. *IEEE Journal of Quantum Electronics*, 2(9):470–473, 1966.

[22] A. Braun, G. Korn, X. Liu, D. Du, J. Squier, and G. Mourou. Self-channeling of high-peak-power femtosecond laser-pulses in air. *Optics Letters*, 20:73–75, 1995.

[23] H Schillinger and R Sauerbrey. Electrical conductivity of long plasma channels in air generated by self-guided femtosecond laser pulses. *Applied Physics B-Lasers and Optics*, 68(4):753–756, APR 1999.

[24] S Tzortzakis, MA Franco, YB Andre, A Chiron, B Lamouroux, BS Prade, and A Mysyrowicz. Formation of a conducting channel in air by self-guided femtosecond laser pulses. *Physical Review E*, 60(4, Part A):R3505–R3507, OCT 1999.

[25] S. Tzortzakis, B. Prade, M. Franco, and A. Mysyrowicz. Time-evolution of the plasma channel at the trail of a self-guided ir femtosecond laser pulse in air. *Optics Communications*, 181(1-3):123–127, July 2000.

[26] B. La Fontaine, F. Vidal, Z. Jiang, C. Y. Chien, D. Comtois, A. Desparois, T. W. Johnston, J. C. Kieffer, H. Pepin, and H. P. Mercure. Filamentation of ultrashort pulse laser beams resulting from their propagation over long distances in air. *Physics of Plasmas*, 6(5):1615–1621, May 1999.

[27] F. Theberge, W. W. Liu, P. T. Simard, A. Becker, and S. L. Chin. Plasma density inside a femtosecond laser filament in air: Strong dependence on external focusing. *Physical Review E*, 74(3):36406, SEP 2006.

[28] George Rodriguez, Anthony R. Valenzuela, Balakishore Yellampalle, Mark J. Schmitt, and Ki-Yong Kim. In-line holographic imaging and electron density extraction of ultrafast ionized air filaments. *Journal of the Optical Society of America B-Optical Physics*, 25(12):1988–1997, DEC 2008.

[29] P. N. Butcher and D. Cotter. *The Elements of Nonlinear Optics*. Cambridge University Press, 1990.

[30] Frank H. Allen, Olga Kennard, David G. Watson, Lee Brammer, A. Guy Orpen, and Robin Taylor. Tables of bond lengths determined by x-ray and neutron diffraction. part 1. bond lengths in organic compounds. *J. Chem. Soc., Perkin Trans. 2*, 12:S1–S19, 1987.

[31] J. H. Eberly, J. Javanainen, and K. Rzazewski. Above-threshold ionization. *Physics Reports*, 204(5):331–383, 1991.

[32] Lawrence C. Evans. *Partial Differential Equations*. American Mathematical Society, 2nd edition, 2010.

[33] C. J. G. J. Uiterwaal, D. Xenakis, D. Charalambidis, P. Maragakis, H. Schroeder, and P. Lambropoulos. Generalized multiphoton-ionization cross sections of the rare gases for 500-fs, 248.6-nm pulses. *Physical Review A*, 57:392–400, 1998.

[34] Xiaoxu Guan, C. J. Noble, O. Zatsarinny, K. Bartschat, and B. I. Schneider. Time-dependent R-matrix calculations for multiphoton ionization of argon atoms in strong laser pulses. *Physical Review A*, 78:053402, 2008.

[35] Ronald Cooper, Roger J. van Sonsbeek, and R. N. Bhave. Pulse radiolysis studies of ion-electron recombination in gaseous argon. *The Journal of Chemical Physics*, 98(1):383–389, 1993.

[36] H. A. Hyman. Electron-impact ionization cross sections for excited states of the rare gases (Ne, Ar, Kr, Xe), cadmium, and mercury. *Phys. Rev. A*, 20(3):855–859, Sep 1979.

[37] H. Brunet, B. Lacour, J. Rocca Serra, M. Legentil, S. Mizzi, S. Pasquiers, and V. Puech. Theoretical and experimental studies of phototriggered discharges in argon and neon. *Journal of Applied Physics*, 68(9):4474–4480, 1990.

[38] V A Ivanov. Dissociative recombination of molecular ions in noble-gas plasmas. *Soviet Physics Uspekhi*, 35(1):17–36, 1992.

[39] E. Zamir, C. W. Werner, W. P. Lapatovich, and E. V. George. Temporal evolution of the electron density in high-pressure electron-beam-excited xenon plasmas. *Applied Physics Letters*, 27(2):56–58, 1975.

[40] Takefumi Oka, Masuhiro Kogoma, Masashi Imamura, Shigeyoshi Arai, and Tsutomu Watanabe. Energy transfer of argon excited diatomic molecules. *The Journal of Chemical Physics*, 70(7):3384–3389, 1979.

[41] J. W. Keto, R. E. Gleason, and G. K. Walters. Production mechanisms and radiative lifetimes of argon and xenon molecules emitting in the ultraviolet. *Phys. Rev. Lett.*, 33(23):1365–1368, Dec 1974.

[42] P Millet, A Birot, H Brunet, H Dijolis, J Galy, and Y Salamero. Spectroscopic and kinetic analysis of the VUV emissions of argon and argon-xenon mixtures. I. study of pure argon. *Journal of Physics B: Atomic and Molecular Physics*, 15(17):2935–2944, 1982.

[43] J.W. Keto, R.E. Gleason Jr., T.D. Bonifield, G.K. Walters, and F.K. Soley. Collisional mixing of the lowest bound molecular states in xenon and argon. *Chemical Physics Letters*, 42(1):125 – 128, 1976.

[44] C. Werner, E. George, P. Hoff, and C. Rhodes. Radiative and kinetic mechanisms in bound-free excimer lasers. *IEEE Journal of Quantum Electronics*, 13(9):769 – 783, sep. 1977.

[45] H. B. Milloy, R. W. Crompton, J. A. Rees, and A. G. Robertson. The momentum transfer cross section for electrons in argon in the energy range 0-4 eV. *Australian Journal of Physics*, 30:61–72, 1977.

[46] L. S. Frost and A. V. Phelps. Momentum-transfer cross sections for slow electrons in He, Ar, Kr, and Xe from transport coefficients. *Phys. Rev.*, 136(6A):A1538–A1545, Dec 1964.

[47] D. E. Golden. Comparison of low-energy total and momentum-transfer scattering cross sections for electrons on helium and argon. *Phys. Rev.*, 151(1):48–51, Nov 1966.

[48] D. A. McPherson, R. K. Feeney, and J. W. Hooper. Microwave transient-response measurements of elastic momentum-transfer collision frequencies in argon. *Phys. Rev. A*, 13(1):167–179, Jan 1976.

[49] S. Kirkpatrick, C. D. Gelatt, and M. P. Vecchi. Optimization by simulated annealing. *Science*, 220:671–680, 1983.

[50] Y J Shiu and M A Biondi. Dissociative recombination in argon - dependence of total rate coefficient and excited-state produciton on electron-temperature. *Physical Review A*, 17(3):868–872, 1978.

[51] Carl Kenty. The recombination of argon ions and electrons. *Phys. Rev.*, 32(4):624–635, Oct 1928.

[52] Manfred A. Biondi and Sanborn C. Brown. Measurement of electron-ion recombination. *Phys. Rev.*, 76(11):1697–1700, Dec 1949.

[53] Manfred A. Biondi. Concerning the mechanism of electron-ion recombination. II. *Phys. Rev.*, 83(5):1078–1080, Sep 1951.

[54] A. Redfield and R. B. Holt. Electron removal in argon afterglows. *Phys. Rev.*, 82(6):874–876, Jun 1951.

[55] M. C. Sexton and J. D. Craggs. Recombination in the afterglows of argon and helium using microwave techniques. *International Journal of Electronics*, 4(6):493–502, 1958.

[56] M. C. Sexton, M. J. Mulcahy, and J. J. Lennon. Electron removal processes in the afterglows of microwave discharges in argon and oxygen. In *Fourth International Conference on Ionization Phenomena in Gases*, 1960.

[57] Manfred A. Biondi. Studies of the mechanism of electron-ion recombination. *Physical Review*, 129(3):1181–1188, 1963.

[58] H. J. Oskam and V. R. Mittelstadt. Recombination coefficient of molecular rare-gas ions. *Phys. Rev.*, 132(4):1445–1454, Nov 1963.

[59] J. N. Fox and R. M. Hobson. Temperature dependence of dissociative recombination coefficients in argon. *Phys. Rev. Lett.*, 17(4):161–163, Jul 1966.

[60] F. J. Mehr and Manfred A. Biondi. Electron-temperature dependence of electron-ion recombination in argon. *Phys. Rev.*, 176(1):322–326, Dec 1968.

[61] Che Jen Chen. Temperature dependence of dissociative recombination and molecular-ion formation in He, Ne, and Ar plasmas. *Phys. Rev.*, 177(1):245–254, Jan 1969.

[62] Chien-Yu Kuo and J. W. Keto. Dissociative recombination in electron-beam excited argon at high pressures. *Journal of Chemical Physics*, 78(4):1851–1860, 1983.

[63] T. Okada and M. Sugawara. Microwave determination of the coefficient of dissociative recombination of Ar_2^+ in Ar afterglow. *Journal of Physics D-Applied Physics*, 26(10):1680–1686, 1993.

[64] J. Royal and A. E. Orel. Dissociative recombination of Ar_2^+. *Phys. Rev. A*, 73(4):042706, Apr 2006.

[65] H. S. W. Massey and H. S. Bishop. *Electronic and Ion Impact Phenomena*. Oxford University Press, 1952.

[66] G. Mainfray and C. Manus. Multiphoton ionization of atoms. *Rep. Prog. Phys.*, 54:1333–1372, 1991.

[67] S. Szatmari and F.P. Schaefer. Simplified laser system for the generation of 60 fs pulses at 248 nm. *Optics Communications*, 68(3):196 – 202, 1988.

[68] R. R. Freeman, T. J. McIlrath, P. H. Bucksbaum, and M. Bashkansky. Pondermotive effects on angular distributions of photoelectrons. *Phys. Rev. Lett.*, 57(25):3156–3159, Dec 1986.

[69] R. R. Freeman and P. H. Bucksbaum. Investigations of above-threshold ionization using subpicosecond laser pulses. *Journal of Physics B: Atomic, Molecular and Optical Physics*, 24(2):325–347, 1991.

[70] H. W. van der Hart. Ionization rates for He, Ne, and Ar subjected to laser light with wavelengths between 248.6 and 390 nm. *Physical Review A*, 73(2):23417, FEB 2006.

[71] N. Popov. Associative ionization reactions involving excited atoms in nitrogen plasma. *Plasma Physics Reports*, 35:436–449, 2009.

[72] H. Brunet and J. Rocca-Serra. Model for a glow discharge in flowing nitrogen. *Journal of Applied Physics*, 57(5):1574–1581, 1985.

[73] W. H. Kasner and Manfred A. Biondi. Electron-ion recombination in nitrogen. *Phys. Rev.*, 137(2A):A317–A329, Jan 1965.

[74] Jr. Myran C. Sauer and William A. Mulac. Studies of light emission in the pulse radiolysis of gases: Electron-ion recombination in nitrogen. *The Journal of Chemical Physics*, 56(10):4995–5004, 1972.

[75] Marlin Whitaker, Manfred A. Biondi, and Rainer Johnsen. Electron-temperature dependence of dissociative recombination of electrons with $N_2^+ \cdot N_2$ dimer ions. *Phys. Rev. A*, 24(2):743–745, Aug 1981.

[76] Y. S. Cao and R. Johnsen. Recombination of N_4^+ ions with electrons. *The Journal of Chemical Physics*, 95(10):7356–7359, 1991.

[77] Yasumasa Ikezoe, Shingo Matsuoka, and Hironc Nakamura. Recombination of N_4^+ and N_3^+ with electrons in atmospheric pressure nitrogen. *Chemical Physics Letters*, 177:366–370, 1991.

[78] O. G. Kosareva, V. P. Kandidov, A. Brodeur, C. Y. Chien, and S. L. Chin. Conical emission from laser-plasma interactions in the filamentation of powerful ultrashort laser pulses in air. *Optics Letters*, 22(17):1332–1334, SEP 1 1997.

[79] W. Liu, F. Theberge, E. Arevalo, J. F. Gravel, A. Becker, and S. L. Chin. Experiment and simulations on the energy reservoir effect in femtosecond light filaments. *Optics Letters*, 30(19):2602–2604, OCT 1 2005.

[80] W. Liu, J. F. Gravel, F. Theberge, A. Becker, and S. L. Chin. Background reservoir: its crucial role for long-distance propagation of femtosecond laser pulses in air. *Applied Physics B-Lasers and Optics*, 80(7):857–860, JUN 2005.

[81] S. L. Chin, N. Akozbek, A. Proulx, S. Petit, and C. M. Bowden. Transverse ring formation of a focused femtosecond laser pulse propagating in air. *Optics Communications*, 188(1-4):181–186, FEB 1 2001.